Final Report

Nuclear Energy Research Initiative
Project Number: 99-0228

Novel investigation of iron cross sections via spherical shell transmission measurements and particle transport calculations for material embrittlement studies

Prepared for the U.S. Department of Energy

by:

National Institute of Standards and Technology
University of Florida
Ohio University

Table of Contents

Table of Contents ii

List of Figures iv

List of Tables ix

I. Introduction 1

I.1 Background information 1

I.2 Project Overview 2

II. Description of the Experiment and Experimental Facility 3

II.1 Iron Spheres 4

II.2 Neutron Source and Source Reactions 12

II.3 Standard Source Spectra 14

II.4 Neutron Detectors and Detector Calibration 14

II.5 Experimental Measurements 15

III. Computational approach and results 34

III.1 Introduction 34

III.2 Particle transport Methodologies 34

III.2.1 Monte Carlo Method 34

III.2.1.1 New Tallying Option for the Monte Carlo MCNP Code 34

III.2.1.2 Monte Carlo Models for Simulation of ToF Experiments 35

III.2.2 Deterministic Sn Method 46

III.3 Optimization of the Experimental Setup 47

III. 4 ToF Simulation 48

III.4.1 Comparison of the ^{15}N(p,n) calculations and Experiments. 48

III.4.1.1 Without Sphere 48

III.4.1.2. Small Sphere 53

III.4.1.3. Large Sphere 56

Section III.4.2 Comparison of the D(d,n) Calculations and Experiments. 58

Section III.4.2.1 Without Sphere 58

Section III.4.2.2 With Sphere 63

III.4.3 Cross Section Evaluation and Adjustment Methodology 66

III.4.4 Generation of the Adjusted Cross Sections 67

III.4.5 The Effect of Modified Cross Sections 68

III.4.5.1 Continuous energy Monte Carlo Simulation 68

III.4.5.2 Multigroup Sn Deterministic Calculation for a PV Problem 70

IV. Summary, Conclusions, and Future Work 72

List of Figures

Figure II.1 The experimental facilities at the Ohio University Accelerator Laboratory. The shielding between the ToF tunnel and the beam swinger facility and the shielding door are indicated in the central portion of the figure with arrows. 4

Figure II.2 Schematic diagram of the 3-cm-thick iron sphere. 5

Figure II.3 Lower hemisphere of the 3-cm -thick iron shell with a gas cell in place. The picture was taken during the April 2001 experiment sequence. Water- and air-cooling is accomplished with three hypodermic tubes. A capillary tube is used to fill the gas cell and monitor its pressure. The rod and ball bearings of the support stand are visible to the left of the lower hemisphere. This view is looking downward on the lower hemisphere with the swinger in the position of 180 degrees. 6

Figure II.4 Setup for the small sphere in the February 2002 experiment. The new style gas cell is shown with attachment to the beam line at the right. The water cooling coil for the cell is shown outside of the cell to the right of the sphere in this picture, near the edge of the yellow label. 7

Figure II.5 Experimental setup for the April 2001 experiment. The low mass stand is directly below the iron sphere. This picture was taken in the direction perpendicular to the ToF tunnel. Also shown is the swinger in the background. To the left in the foreground is the arm that held the monitor detector for this experiment. 8

Figure II.6 Schematic diagram of the larger iron sphere used in these experiments. 9

Figure II.7 The setup for the large sphere. The low mass stand is shown below the iron sphere. This picture was taken in the direction of the ToF tunnel. 10

Figure II.8 Schematic drawing of the new gas cell: the foil holder, charge suppression and collimation are shown. 13

Figure II.9 Neutron detector efficiency determination for the experimental work. 15

Figure II.10 Source data for the D(d,n) reaction with 3.0 MeV deuterons incident on the gas. 18

Figure II.11 The "sphere-on" spectra obtained with the small (3-cm-thick) sphere and the D(d,n) source reaction with 3.0 MeV deuterons incident on the gas. 19

Figure II.12 Source data for the D(d,n) reaction with 5.0 MeV deuterons incident on the gas. 20

Figure II.13 The "sphere-on" spectra obtained with the small (3-cm-thick) sphere and the D(d,n) source reaction with 5.0 MeV deuterons incident on the gas. 21

Figure II.14 Shown is the source spectrum for the 15N(p,n) reaction with 5.1 MeV protons incident on the gas. 23

Figure II.15 The "sphere-on" spectra obtained with the small (3-cm-thick) sphere and for the 15N(p,n) reaction with 5.1 MeV protons incident on the gas. All of the measured angles are shown. 24

Figure II.16The "sphere-on" spectra obtained with the large (8-cm-thick) sphere and for the 15N(p,n) reaction with 5.1 MeV protons incident on the gas. All of the measured angles are shown 25

Figure II.17 Shown is the source spectrum for the D(d,n) reaction with 3.0 MeV deuterons incident on the gas. All of the measured angles are shown. 26

Figure II.18 The "sphere-on" spectra obtained with the large (8-cm-thick) sphere and for the D(d,n) reaction with 3 MeV deuterons incident on the gas. 27

Figure II.19 Source shown is the source spectrum for the D(d,n) reaction with 5.0 MeV deuterons incident on the gas. All of the measured angles are shown. 28

Figure II.20 The "sphere-on" spectra obtained with the large (8-cm-thick) sphere and the for the D(d,n) reaction with 5 MeV deuterons incident on the gas. All of the measured angles are shown 29

Figure II.21 Shown is the source spectrum for the D(d,n) reaction with 7.0 MeV deuterons incident on the gas. All of the measured angles are shown. 30

Figure II.22 The "sphere-on" spectra obtained with the large (8-cm-thick) sphere and for the D(d,n) reaction with 7 MeV deuterons incident on the gas. All of the measured angles are shown 31

Figure II.23 Comparison of the gamma peak region with all of the gamma rays allowed, and with only the most energetic gamma rays allowed. The spectra have been renormalized to allow the differences in position to be shown. The time calibration is ~0.6 ns/channel. 33

Figure III.1 The 5 MeV D(d,n) DROSG versus experimental source angular distribution comparison . 36

Figure III.2 Comparison of the ^{15}N(p,n) DROSG prediction to the experiment source angular dependence. 36

Figure III.3 Distribution of the number of resolution intervals per experimental bin size. 37

Figure III.4 The comparison of the 3 MeV D(d,n) source spectra before and after redistribution comparison. 38

Figure III.5 Source Generation Interpolation Schematic. 39

Figure III.6 The 3 MeV D(d,n) interpolated spectrum. 40

Figure III.7 Experimental source distribution for the 5 MeV D(d,n) reaction. 41

Figure III.8 Complete corrected 5 MeV D(d,n) source distribution. 42

Figure III.9 Schematic of the large model. A cutaway view of the iron sphere center to the time of flight tunnel region is shown above. Cross sections through the iron sphere, the collimator and the time of flight tunnel are shown from right to left below. 43

Figure III.10 Schematic of the cut down simplified model (The top diagram shows the iron sphere to the time of flight tunnel, and the bottom diagrams show x-y projections of the iron sphere, the collimator and an ideal detector, from right to left.) 44

Figure III.11 Schematic of MCNP Model Utilized 44

Figure III.12 Comparison of the neutron flux distributions obtained using different quadrature sets compared to a reference Monte Carlo solution (shown in dark blue). 46

Figure III.13 Estimation of the number of inelastically scattered neutrons which are detected at the detector for different source energies and sphere thicknesses. 47

Figure III.14 Comparison of ^{15}N(p,n) Monte Carlo calculations and experimental data for the 0 degree angle. 49

Figure III.15 Comparison of ^{15}N(p,n) Monte Carlo calculations and experimental data for the 15 degree angle. 49

Figure III.16 Comparison of ^{15}N(p,n) Monte Carlo calculations and experimental data for the 45 degree angle. 50

Figure III.17 Comparison of ^{15}N(p,n) Monte Carlo calculations and experimental data for the 60 degree angle. 50

Figure III.18 Comparison of ^{15}N(p,n) Monte Carlo calculations and experimental data for the 90 angle. 51

Figure III.19 Comparison of ^{15}N(p,n) Monte Carlo calculations and experimental data for the 100 degree angle. 51

Figure III.20 Comparison of ^{15}N(p,n) Monte Carlo calculations and experimental data for the 120 degree angle. 52

Figure III.21 Comparison of ^{15}N(p,n) Monte Carlo calculations and experimental data for the 135 degree angle. 52

Figure III.22 Comparison of ^{15}N(p,n) Monte Carlo calculations and experimental data for the 0 degree angle. (Small Sphere On) 54

Figure III.23 Comparison of ^{15}N(p,n) Monte Carlo calculations and experimental data for the 45 degree angle. (Small Sphere On) 54

Figure III.24 Comparison of ^{15}N(p,n) Monte Carlo calculations and experimental data for the 90 degree angle. (Small Sphere On) 55

Figure III.25 Comparison of ^{15}N(p,n) Monte Carlo calculations and experimental data for the 0 degree angle. (Large Sphere On) 56

Figure III.26 Comparison of ^{15}N(p,n) Monte Carlo calculations and experimental data for the 45 degree angle. (Large Sphere On) 57

Figure III.27 Comparison of ^{15}N(p,n) Monte Carlo calculations and experimental data for the 90 degree angle. (Large Sphere On) 57

Figure III.28 Comparison of 3 MeV D(d,n) Monte Carlo calculations and experimental data for the 0 degree angle. 59

Figure III.29 Comparison of 3 MeV D(d,n) Monte Carlo calculations and experimental data for the 45 degree angle. 59

Figure III.30 Comparison of 3 MeV Monte Carlo calculations and experimental data for 90 degree angle. 60

Figure III.31 Comparison of 5 MeV D(d,n) Monte Carlo calculations and experimental data for the 0 degree angle. 60

Figure III.32 Comparison of 7 MeV D(d,n) Monte Carlo calculations and experimental data for the 0 degree angle. 61

Figure III.33 Comparison of 7 MeV D(d,n) Monte Carlo calculations and experimental data for the 45 degree angle. 61

Figure III.34 Comparison of 7 MeV D(d,n) Monte Carlo calculations and experimental data for the 90 degree angle. 62

Figure III.35 Comparison of 3MeV D(d,n) Monte Carlo calculations and experimental data for the 0 degree angle. (Large Sphere On) 64

Figure III.36 Comparison of 5MeV D(d,n) Monte Carlo calculations and experimental data for the 0 degree angle. (Large Sphere On) 64

Figure III.37 Comparison of the 7MeV D(d,n) Monte Carlo calculations and experimental data for the 0 degree angle. (Large Sphere On) 65

Figure III.38 Fe-56 ENDF/B-VI and adjusted nonelastic, inelastic, elastic, and total cross section. 68

Figure III.39 Comparison of modified 3 MeV D(d,n) Monte Carlo calculations and experimental data for 0 degree angle. (Peak Region) 69

Figure III.40 Comparison of modified 5 MeV D(d,n) Monte Carlo calculations and experimental data for the 0 Degree angle. (Peak Region) 69

Figure III.41 Comparison of Modified 7 MeV D(d,n) Monte Carlo calculations and experimental data for the 0 degree angle. (Peak Region) 70

Figure III.42 Reactor pressure vessel model 70

List of Tables

Table II.1The chemical impurities determined for the iron used for fabricating the iron spheres. These values represent our current knowledge on these sphere's composition; representative samples are available to be analyzed if it is later determined that more accurate results are needed. A dash is shown when no amount of a particular impurity constituent had been detected. 11

Table II.2 Summary of the first experiment in April 2001. 17

Table II.3 Summary of the second experiment in February 2002. 22

Table III.1One sigma Statistical Error for $^{15}N(p,n)$ Sphere Off Monte Carlo Simulation 53

Table III.2 One sigma statistical error for $^{15}N(p,n)$ small sphere on Monte Carlo simulation 55

Table III.3 One Sigma Statistical Error for $^{15}N(p,n)$ Small Sphere On Monte Carlo Simulation 58

Table III.4 One sigma Statistical Error for D(d,n) Sphere Off Monte Carlo Simulations 62

Table III.5 Experiment and Calculation differences for D(d,n) Sphere Off Simulations 63

Table III.6 One Sigma Statistical Error for zero-degree D(d,n) Large Sphere On Monte Carlo Simulation 65

Table III.7Comparison of estimated and ENDF/B-VI total cross sections using the D(d,n) experiments 66

Table III.8 Cross Section adjustments and their associated energy bin 67

Table III.9 Reaction Rate Ratios (ENDF/B-VI/adjusted cross-section) at the Cavity Dosimeter 71

I. Introduction

We have been pursuing a multi-year project, funded by the U.S. Department of Energy, to study neutron scattering interactions in iron. The principal objective of this work is to investigate the well-known deficiency that exists for reactor pressure vessel neutron fluence determinations. Specifically, we are using the spherical-shell transmission method, employing iron shells with different thicknesses, and neutron time-of-flight (ToF) measurements of the scattered neutrons, in an effort to precisely determine specific energy regions over which deficiencies in the non-elastic scattering cross section for neutron scattering in iron appear to exist.

I.1 Background information

Nuclear data play a governing role in the safe design and operation of both current and future generation nuclear power plants. In particular, knowledge of iron scattering cross sections is essential due to the extensive use of iron in the construction of nuclear plant systems, including the reactor pressure vessel (RPV), and accurate knowledge of iron cross sections is needed to adequately assess plant design and operational characteristics, such as the structural integrity of the RPV. It has long been known that during the operational lifetime of a nuclear power plant, there occurs a reduction in fracture toughness of the pressure vessel brought about by fast-neutron irradiation, which degrades the vessel's ability to maintain structural integrity, which thereby necessitates the accurate determination of the vessel exposure. Specific regulatory provisions require that operators of commercial nuclear power stations accurately determine and monitor the RPV fast-neutron fluence. Calculation of the absolute neutron fluence is accomplished by considering the transport of neutrons from the reactor core out through the reactor vessel and into the vessel cavity. These calculations are exceedingly complex, and their ultimate reliability is predicated, in large part, upon the fidelity of the nuclear data employed therein. Often times the agreement between measured and calculated neutron fluences (for neutrons with energies greater than 1 MeV) may be no better than approximately 20 % for deep penetrations.[1]

Efforts to improve the agreement between measurement and calculation have resulted in re-evaluations of the iron cross sections. Overall, these changes have resulted in an increase in the calculated neutron transmission for those neutrons with energies greater than 1 MeV, mitigating somewhat the observed discrepancy between the computed and measured neutron fluence. Notwithstanding, there continue to remain apparent differences between the experimental results obtained from neutron fluence monitors placed at in-vessel and ex-vessel locations in operating nuclear reactors, and the corresponding results from neutron transport calculations for the fast-neutron fluence at those positions. The summary documentation for the ENDF/B-VI nuclear data file specifically calls out the weaknesses in the iron evaluation relative to the needs of the reactor pressure vessel dosimetry community, especially the ^{56}Fe inelastic scattering cross section.[2] The problem may be due to poor or incomplete information on the iron levels and level density contained in ENDF/B-VI.

In 1982, measurements of iron-moderated ^{252}Cf fission-neutron spectra were conducted in the Czech Republic.[3] For these experiments, differential neutron fluence spectra emitted from a californium neutron source centered within iron spheres of varying thickness were measured using proportional proton recoil counters and a stilbene scintillator. In 1993, Sajo, et al.,[4] examined whether simulations of the Czech experiments performed using the ENDF/B-VI cross section library accurately predicted the measured neutron fluence spectra, and concluded that, although the fluence spectra calculated using the ENDF/B-VI cross sections exhibit improved agreement with measurements as compared to corresponding spectra calculated using the ENDF/B-IV and ENDF/B-V cross section data sets, the fluence spectrum above 1 MeV obtained using ENDF/B-VI remains significantly lower than that observed in the measurements. More recently, a group from the National Institute of Standards and Technology (NIST) also reported the results of proton recoil measurements[5] of the iron-moderated ^{252}Cf fission-neutron leakage spectrum from a 50-cm diameter iron sphere. Generally, there is good agreement between the NIST and Czech data sets in the energy range from 0.1 MeV to 1.0 MeV. In the energy interval above 1 MeV, the Czech data indicate a neutron fluence that is, on average, approximately 16 % to 20 % greater than the NIST measurement. The NIST group also performed Monte Carlo neutron transport calculations of the iron-moderated ^{252}Cf neutron spectra generated in their experiment using ENDF/B-VI cross sections. Comparison of these calculations with the measurements revealed that, for the important energy region above 1 MeV, the calculational results continue to underpredict measurement by as much as 11 %. Such large discrepancies translate into substantially more restrictive operational limits being placed on plant operations in order to ensure the requisite level of nuclear safety.

I.2 Project Overview

As previously mentioned, we utilize the spherical-shell transmission method and neutron ToF spectroscopy of the scattered neutrons to obtain experimental information concerning the interactions of fast neutrons scattering in iron shells. This method is a variant of the classical spherical-shell transmission method, employing iron shells with different thicknesses. We perform our measurements using a combination of two accelerator-based neutron sources: ^{15}N(p,n) and D(d,n), in conjunction with two high-purity iron shells with different thicknesses covering the neutron source, and a remotely positioned neutron detector for collecting the ToF data. The iron spheres were fabricated with shell thicknesses of approximately 3 cm and 8 cm. These selections were chosen in order to enhance the experimental sensitivity to the iron cross section, and were made based on Monte Carlo simulations of the experiment that indicate that a range of shell thicknesses ranging from 4 cm to 8 cm should be optimal.

The spherical shell transmission method for neutrons is especially well suited to measurements of the non-elastic cross section in iron, which, for the energies of interest, is dominated by inelastic scattering. The measurements are analogous to normal neutron transmission measurements that yield the neutron total cross section, and can be done simply and with very high accuracy, since they are not limited by measurements of the absolute neutron flux. For cross section evaluations, such as the Evaluated Nuclear Data

Files (ENDF), measurements such as those that we are performing are especially important because of the small uncertainties that can be obtained. These measurements reveal information on the total non-elastic cross section, various components of the non-elastic cross section for which there are neutrons in the exit channel, and also provide a way of determining the quality of evaluated microscopic cross section data by an application to a macroscopic system through which neutron transport can be determined. Moreover, such measurements are used to establish normalizations for some partial cross section measurements and for determining cross section components that are difficult to measure directly.

During the course of this project, two experimental runs were made, in April of 2001 and February of 2002. The experimental measurements are complemented by detailed particle transport calculations as a means of both optimizing the experimental setup and evaluating how well the prevailing interaction cross sections predict neutron transport through thick-sections of steel. Analysis of the experimental data involves correlating the data with theoretical calculations of neutron transport through the iron spheres in order to evaluate the degree to which the calculated neutron spectra predict the measured spectra relative to different types of particle interactions. In doing so, we have developed new methodologies for performing neutron transport calculations that will be useful to a range of transport problems.

II. Description of the Experiment and Experimental Facility

We performed our experimental measurements at the Ohio University Accelerator Laboratory (OUAL), using neutron ToF spectroscopy techniques. This facility consists of a tandem Van de Graaff accelerator with several available flight paths, and there are a number of different charged particle beams that can be produced for use in this project, the most common ones being protons and deuterons. At this facility, specific scattering geometries may be investigated by utilizing the accelerator's "beam swinger,"[6] a feature that permits experimental measurements to be made at various angles along a single well-defined flight path without the need to move the neutron detector, thereby not disturbing the precision alignment of the neutron beamline. Further, the beam swinger allows measurements to be made with a single neutron detector that has a well-characterized efficiency. The Ohio University accelerator facility is unique among accelerator facilities to possess this capability. An Illustration of the OUAL facility is presented in Figure II.1.

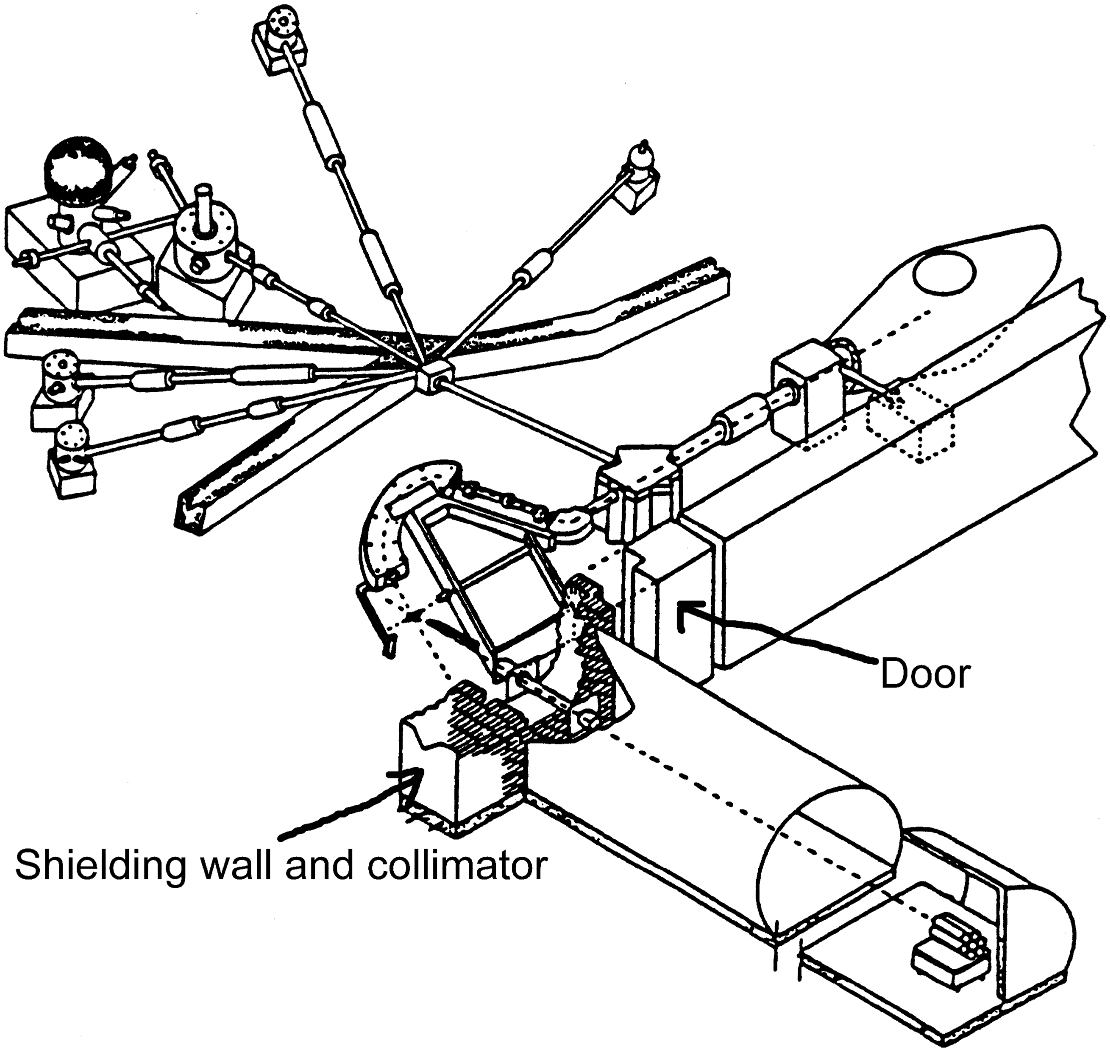

Figure II.1 The experimental facilities at the Ohio University Accelerator Laboratory. The shielding between the ToF tunnel and the beam swinger facility and the shielding door are indicated in the central portion of the figure with arrows.

The physical setup for the experiment consisted of iron spheres, a support stand for the spheres, gas cells placed inside the spheres that serve as the source of neutrons, beam collimators, and a neutron detector and associated electronics. The iron spheres, beam collimator and neutron detector were all aligned along the neutron beam line. The collimator in the shielding wall at the tunnel entrance was 30 cm in diameter. These components will be discussed below followed by a summary of the results.

II.1 Iron Spheres

A small iron sphere with a 3-cm-thick shell was used in both sets of experiments. This spherical iron shell was fabricated at NIST, and is composed of two hemispherical sections possessing an inner radius of 4.50 cm and an outer radius of 7.5 cm. One of the hemispherical sections has a 1.27-cm hole drilled at 45 degrees to the plane between the hemispheres to permit insertion of the neutron source gas cell**.** During fabrication, threaded bolt holes were drilled into the hemispherical sections to allow the machining of the outside spherical surface. These holes were subsequently plugged with cap head bolts for the experiments performed in April 2001. A diagram of this sphere is shown in Figure II.2. A neutron radiograph taken of this sphere using 10 MeV neutrons showed that small voids were present at the bottom of the cap head bolts. Consequently, for the second set of experiments performed in February of 2002, replacement bolts were designed and fabricated so as to reduce the void volume in the material down to a minimum.

A picture of one hemisphere of this sphere with the gas cell in place is shown in Figure II.3. Note that in the initial set of experiments a stainless steel tube was used to extend the OUAL standard gas cell while in the second set of experiments the triple concentric design was used, which is described below and shown in Figure II.4. An overview of the entire setup is shown in Figure II.5.

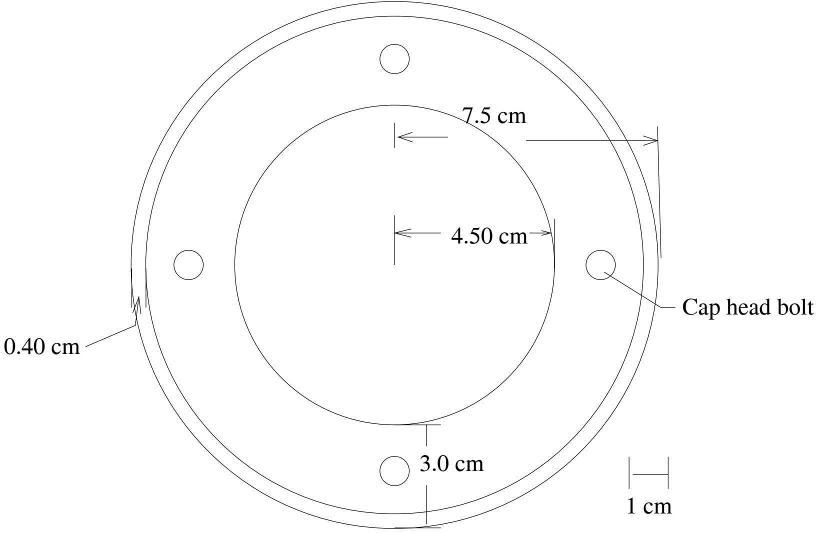

Figure II.2 Schematic diagram of the 3-cm-thick iron sphere.

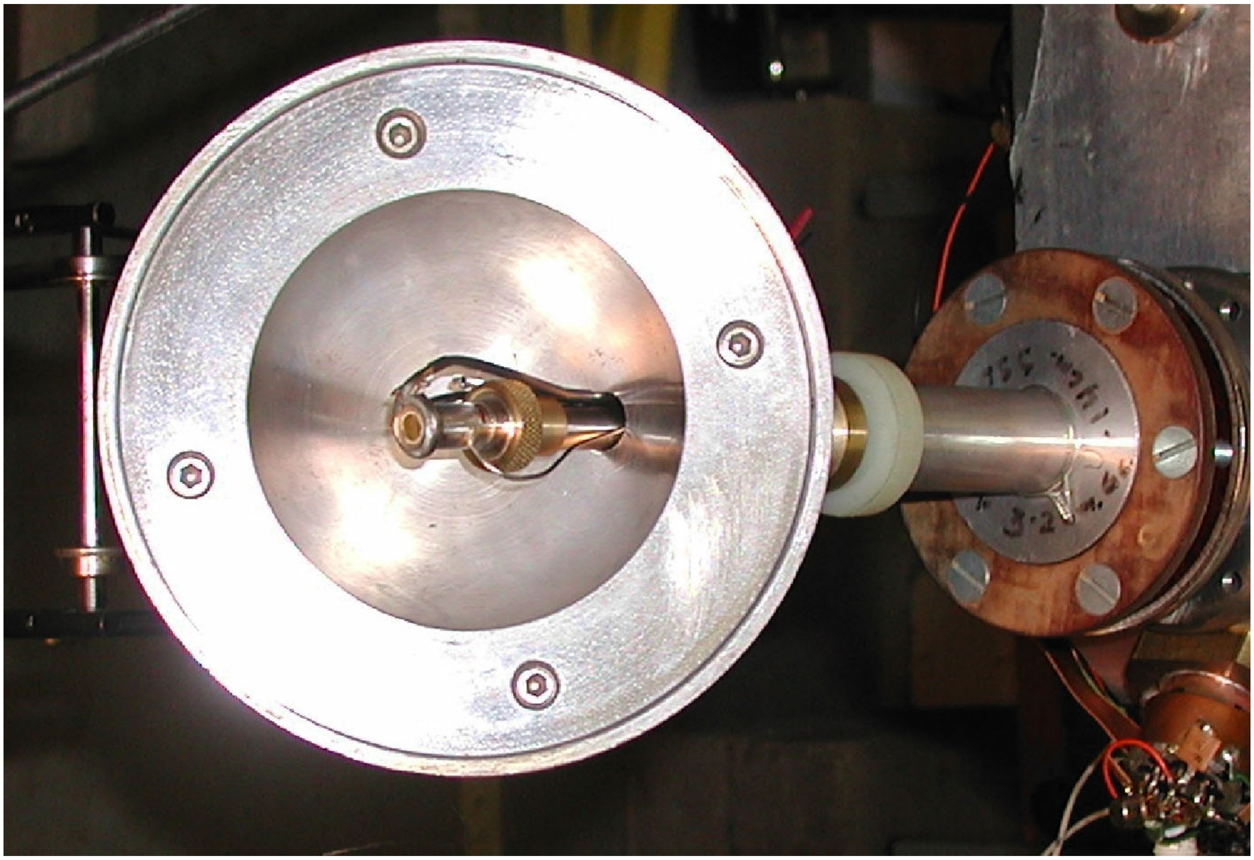

Figure II.3 Lower hemisphere of the 3-cm -thick iron shell with a gas cell in place. The picture was taken during the April 2001 experiment sequence. Water- and air-cooling is accomplished with three hypodermic tubes. A capillary tube is used to fill the gas cell and monitor its pressure. The rod and ball bearings of the support stand are visible to the left of the lower hemisphere. This view is looking downward on the lower hemisphere with the swinger in the position of 180 degrees.

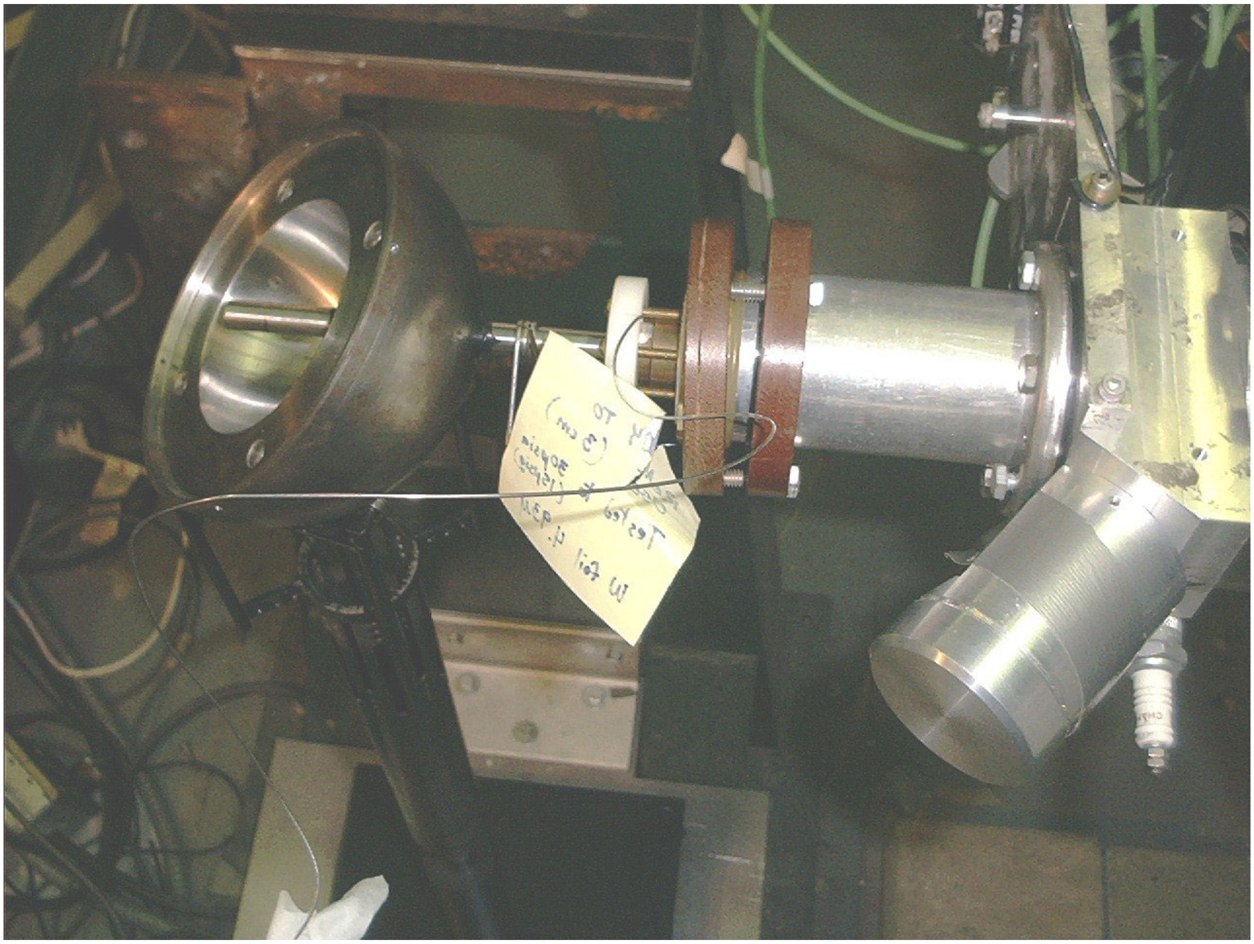

Figure II.4 Setup for the small sphere in the February 2002 experiment. The new style gas cell is shown with attachment to the beam line at the right. The water cooling coil for the cell is shown outside of the cell to the right of the sphere in this picture, near the edge of the yellow label.

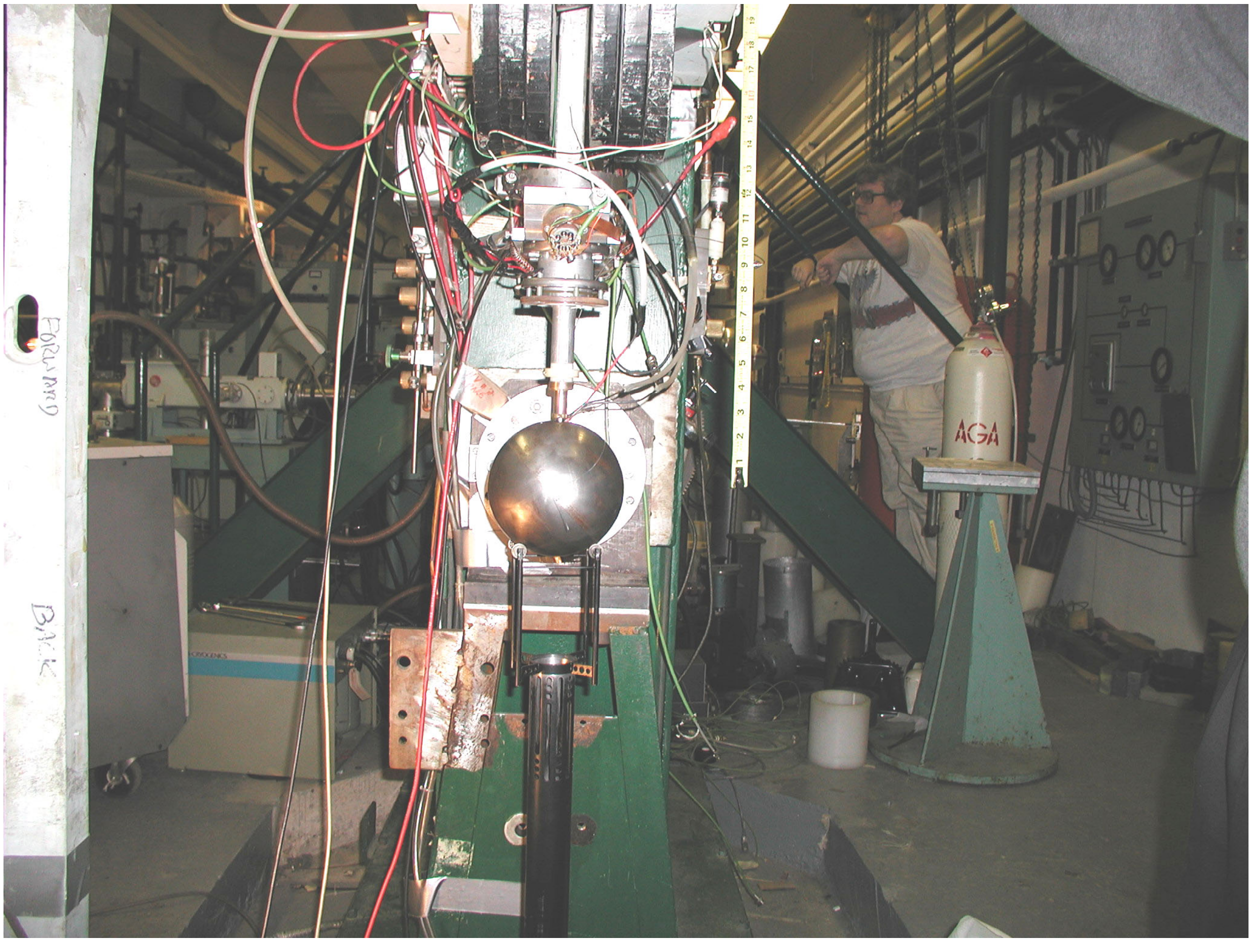

Figure II.5 Experimental setup for the April 2001 experiment. The low mass stand is directly below the iron sphere. This picture was taken in the direction perpendicular to the ToF tunnel. Also shown is the swinger in the background. To the left in the foreground is the arm that held the monitor detector for this experiment.

The more recently fabricated (large) iron sphere (with ~8 cm wall thickness) was fabricated from high-purity 99.47% magnet iron with a low carbon content that was hot forged and annealed. The iron sphere was fabricated in the form of two hemispherical sections that were cut from cylindrical billets. This sphere had an inner radius of 2.47 cm and an outer radius of 10.47 cm with an entrance hole for the gas cell of 1.27 cm diameter positioned at the plane between the two hemispheres (equator). The fabrication work was performed using a numerical controlled lathe at Ohio University. The new sphere has some major advantages over the first sphere that we used. The new sphere was fabricated so that there was less interior void space, which allowed the sphere to have a greater annular thickness without incurring a large increase in its outer diameter. This aspect has important implications regarding proper alignment of the beamline components and the selection of appropriate neutron beam collimation. A diagram of this sphere is shown in Figure II.6. The two hemispheres were made by machining jaws to fit the partially completed sphere in order to hold it without the use of any additional fixtures, which would have required drilling and tapping of holes to allow the machining of the round outer surface of the hemisphere (as had been done for the smaller sphere). Consequently, the new sphere has no voids, which simplifies the modeling. The purity of the iron is also higher thereby allowing for more accurate modeling of the experimental results. The setup for this large sphere is shown in Figure II.7.

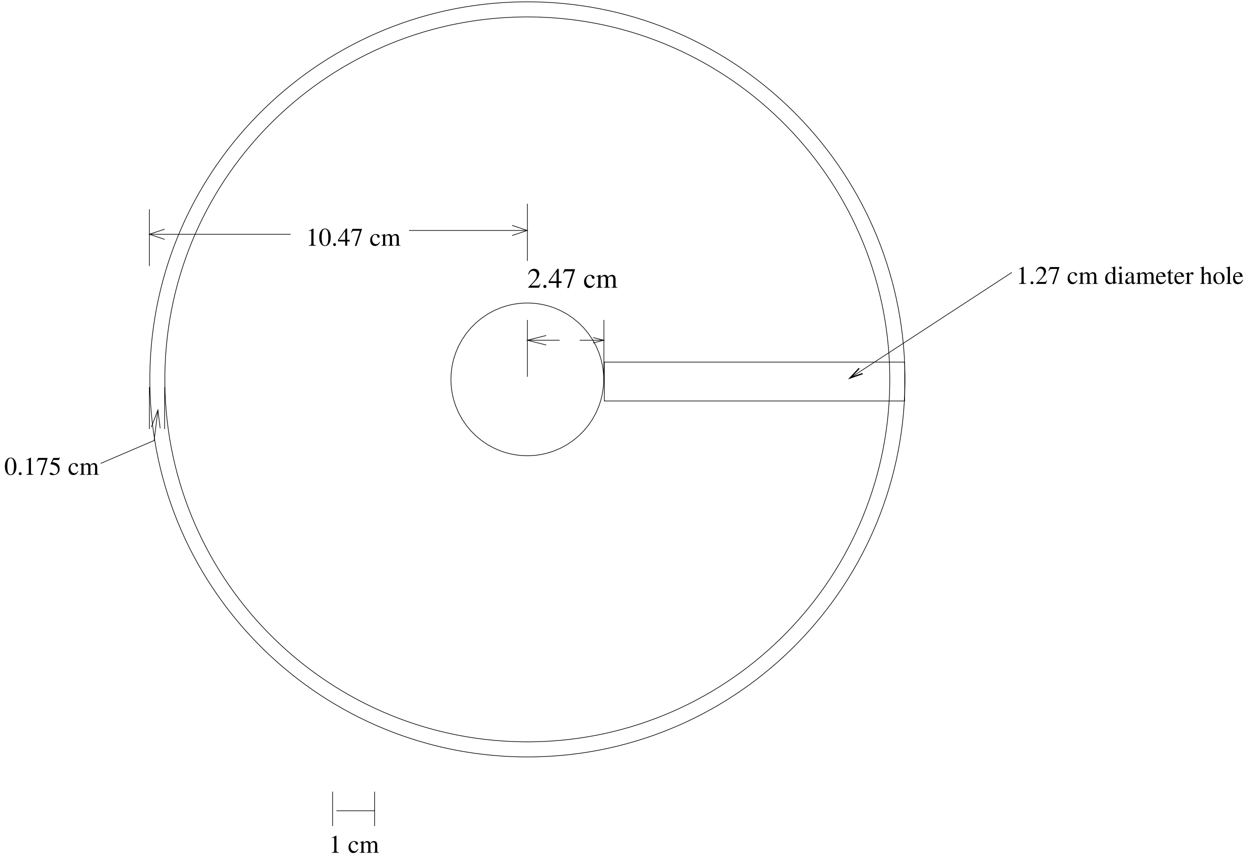

Figure II.6 Schematic diagram of the larger iron sphere used in these experiments.

Figure II.7 The setup for the large sphere. The low mass stand is shown below the iron sphere. This picture was taken in the direction of the ToF tunnel.

A support stand was needed to permit proper positioning of the spheres on the beamline. The spheres were supported using a low-mass, external structure that permitted free rotation of the sphere/target-cell assembly as the accelerator beam swinger was positioned to various angles. Some of its special design features include arms to support the sphere during rotation and roller bearings to insure that sphere material (iron) is not scraped from the sphere when rotations are made. Two upper sections of the support stand were made for accommodating both the larger and smaller spheres. The greater mass of the new sphere required that a lifter be used to allow careful placement of the sphere on the stand. The lifter consisted of a simple vacuum chamber fitted with an o-ring. When vacuum was applied to the chamber while the o-ring was in contact with the sphere, atmospheric pressure would hold the sphere in place. The lifter was fitted with a hook so that the sphere (or half of the sphere) could be moved with an overhead manual crane.

Chemical analyses of the iron used to fabricate each sphere were performed in order to determine their respective impurity content; the results of these analyses are presented in Table II.1**.** The small sphere sample was analyzed by X-ray fluorescence (XRF) at NIST. The melt for the large sphere was performed commercially with measurements of the carbon by a carbonometer and XRF for the remainder of the elements. A large sample of the metal shavings from the machining of the large sphere has been reserved for future analysis as needed.

Table II.1The chemical impurities determined for the iron used for fabricating the iron spheres. These values represent our current knowledge on these sphere's composition; representative samples are available to be analyzed if it is later determined that more accurate results are needed. A dash is shown when no amount of a particular impurity constituent had been detected.

	Small Sphere Impurities	**Large Sphere Impurities**
Element	**Percentage by Mass**	**Percentage by Mass**
C	0.3-1.0	0.020
P	0.040	0.015
S	-	0.013
Si	0.480	0.010
Mn	0.840	0.250
Ni	0.050	0.090
Cr	0.270	0.070
Al	0.240	-
Cu	0.330	-
As	0.040	-
Mo	0.050	-
Ca	~0.02	-
Cl	~0.06	-

II.2 Neutron Source and Source Reactions

We studied various neutron-producing nuclear reactions to determine which neutron source targets would be the most appropriate for our measurements. The ideal case is where the source produces neutrons that have the same energy at all angles, and where the intensity of neutron emission is isotropic. Then measurements of the sphere's transmission yield the non-elastic cross section. Unfortunately, a source reaction with these properties does not exist. The objective then was to obtain a source that has properties that are close to the ideal case, with the deviation from isotropy and the kinematic energy spread of the neutrons emitted into the angular interval from 0° to 180, both being minimized. Studies were done for the following source reactions: $D(d,n)^3He$, $T(p,n)^3He$, $T(d,n)^4He$, $^7Li(p,n)^7Be$, $^9Be(p,n)^9B$, $^9Be(\alpha,n)^{12}C$, $^{10}Be(\alpha,n)^{13}C$, $^{11}B(p,n)^{11}C$, $^{12}C(p,n)^{12}N$, $^{12}C(d,n)^{13}N$, $^{13}C(p,n)^{13}N$, $^{13}C(\alpha,n)^{16}O$, $^{15}N(^3He,n)^{17}F$, $^{19}F(p,n)^{19}Ne$, $^{19}F(d,n)^{20}Ne$, $^{19}F(\alpha,n)^{22}Na$, $^{16}O(d,n)^{17}F$, $^{15}N(p,n)^{15}O$ and $^{51}V(p,n)^{51}Cr$. This work involved investigating the neutron energy as a function of laboratory angle, and the angular distribution , in the laboratory system, of the neutrons, produced by these charged-particle reactions. We performed kinematic calculations of the neutron energies from these reactions, and found that more the massive targets yielded an overall smaller range in energy of the emitted neutrons throughout the full angular interval from 0° to 180°. For the same reason we determined that is is also preferential to use the lighter particle as the projectile. For very massive targets, however, the first excited state of the residual nucleus (and possibly higher excited states, too) tends to be at a low energy. This limits the neutron energy that can be used since more than one energy group of neutrons will be produced otherwise. Angular distribution data for the neutron source reactions listed above generally need improvement. Our study led us to conclude that the best reactions for the present experiment were the $^{15}N(p,n)^{15}O$ reaction at the lower neutron energies and the $D(d,n)^3He$ reaction at the higher energies.

The neutrons needed for these pulsed sphere experiments are generated in gas cell targets. During the first experiment series, the D(d,n) source reaction was used. The beam target was a small gas-filled cell measuring 3 cm long and filled with deuterium gas to a pressure of 207 kPa (2 atmospheres). For this series of experiments, the gas was contained in the cell by a thin 4.9-micron tungsten entrance window. The cell is made of stainless steel tubing for the body, and has a 1 mm thick gold foil beam stop. (Studies previously completed indicate that use of a gold foil reduces the production of background neutrons from the beam stop.) This gas cell is connected to the beam line by a small vacuum tube, which connects the charge suppression and beam collimation fixtures to the gas cell, and is positioned at the center of the sphere.

For the second series of experiments, both the D(d,n) reaction (using a gas pressure of 2 atmospheres) and the $^{15}N(p,n)$ reaction (using a gas pressure of 1.5 atmospheres) were used. For this series of experiments, a new gas cell was constructed to provide better charged-particle beam collimation and current integration capacity. For this cell, three concentric tubes of stainless steel constitute the major pieces. The outer tube contains a 1-mm thick gold beam stop at its end with water cooling applied by a coil of hypodermic tubing at the base of the tube (outside the iron sphere diameter). The middle tube holds a ~5 micrometer -thick tungsten foil entrance window at its end. The inner tube holds the final beam collimator and charge suppression. Each tube is soft soldered to a brass cylinder that has o-ring seals. Between the inner tube's brass cylinder and the outer and middle tubes, Teflon was used to insulate the outer two tubes for charge collection. A schematic diagram of the newly designed gas cell is shown in Figure. II.8.

The neutron fluence from the charged-particle source reactions was monitored by integrating the charge accumulated when the charged-particle beam was stopped in the beam stop. Charge collection was accomplished by electrically isolating the target gas cell using an electrical isolation flange on the beam line. Since the gas cell was in contact with the iron sphere, the stand was placed on a sheet of epoxy fiberglass circuit board material to obtain sufficient isolation from ground.

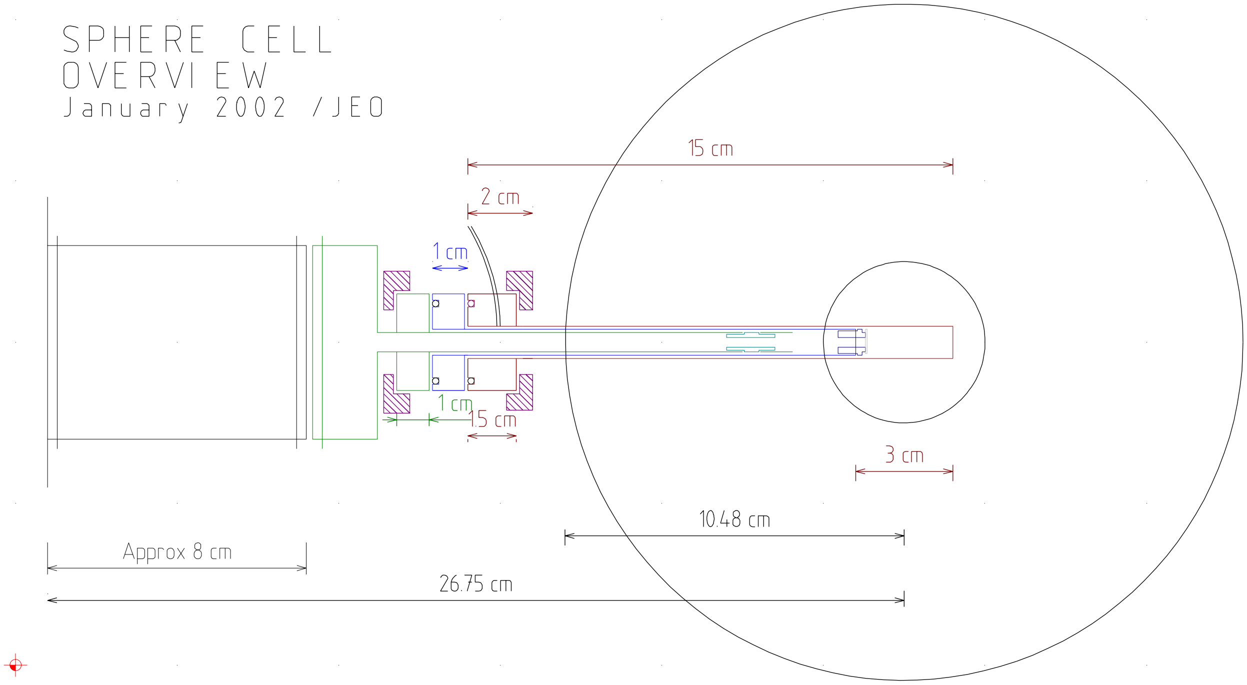

.

Figure II.8 Schematic drawing of the new gas cell: the foil holder, charge suppression and collimation are shown.

II.3 Standard Source Spectra

Measurements were made of the source spectra for several reactions that may be used as spectra standards for this work. The most useful are the Be(d,n), B(d,n) and Al(d,n) reactions. Though the intensities are somewhat more favorable for the Be(d,n) and B(d,n) reactions, the Al(d,n) reaction may be preferred in the energy region above 250 keV, since there is less energy-dependent structure contained in its spectrum. The detector efficiencies have been determined well at energies above about 250 keV. The Al(d,n) spectra measurements were made relative to the ^{235}U(n,f) neutron cross section standard. We also performed measurements of the B(d,n) spectra relative to the Al(d,n) results. Making efficiency measurements with white spectrum source reactions such as these removes one of the limitations on previous work, such as the LLNL experiment where the efficiency was determined at a limited number of isolated points with subsequent interpolation between those points. The efficiencies of the lithium glass and NE-213 detectors were determined at the time of the experiments by using suitable white spectrum source reactions. Another major advantage of using reactions such as B(d,n) and Al(d,n) to calibrate the detectors is that that the accuracy of the spherical shell results can be improved without repeating the experiment since measurements to improve the accuracy of the B(d,n) and Al(d,n) white source reactions at a later time will then lead to refinements in the spherical shell results. The group at OUAL already plans improvements for these secondary neutron standards.

II.4 Neutron Detectors and Detector Calibration

For the first experiment, we employed a Li-glass neutron detector for data collection. The detector utilizes the ^{6}Li(n,t) reaction, which has high efficiency for the very low-energy, inelastically scattered neutrons that are present in the experiment. After mounting the 12.7-cm-diameter by 1.27-cm-thick detector on an appropriate photomultiplier tube, we positioned the detector on the beamline and performed an optical alignment of the beamline components. We placed the detector inside of a lead shielding enclosure in order to reduce the largely gamma-ray background arising from the radiative capture of scattered neutrons and from natural radiation sources contained in the ToF tunnel's structural material. The dimensions of the lead shield, relative to those of the ToF tunnel collimator, dictated that the neutron flight path be approximately 5 m long from the source to the detector. We arranged the experiment by considering the flight path, collimation, shielding, and the size of the iron sphere, so that the neutron detector would maintain a "full view" of the iron sphere through the collimator sections, yet no direct neutrons emerging from the sphere would strike the lead shielding.

For the first experiment, we were limited to a maximum energy of 6 MeV deuterons due to accelerator performance, which required us to make use of the B(d,n) reaction as a neutron standard for detector calibration. The B(d,n) thick target reaction with 5.0 MeV incident deuteron energy was used since this corresponds to the calibration energy.

For the second experiment, a lead shielding enclosure similar to that used in the first experiment was used. An NE-213 detector having a thickness of 5.08 cm and a diameter of 12.7 cm was used. We began experimental runs by collecting necessary calibration spectra to determine the efficiency of the NE-213 neutron detector. For this task we used the Al(d,n) reaction[7], which we determined is known slightly better than the B(d,n) reaction. A stopping aluminum target was used along with a deuteron energy of 7.44 MeV at an angle of 120 degrees for these calibrations. This energy and angle were those used for the source spectrum determination that had been done previously relative to the ^{235}U(n,f) standard neutron cross section. The detector efficiencies, including losses due to air absorption or scattering, are given in Figure II.9.

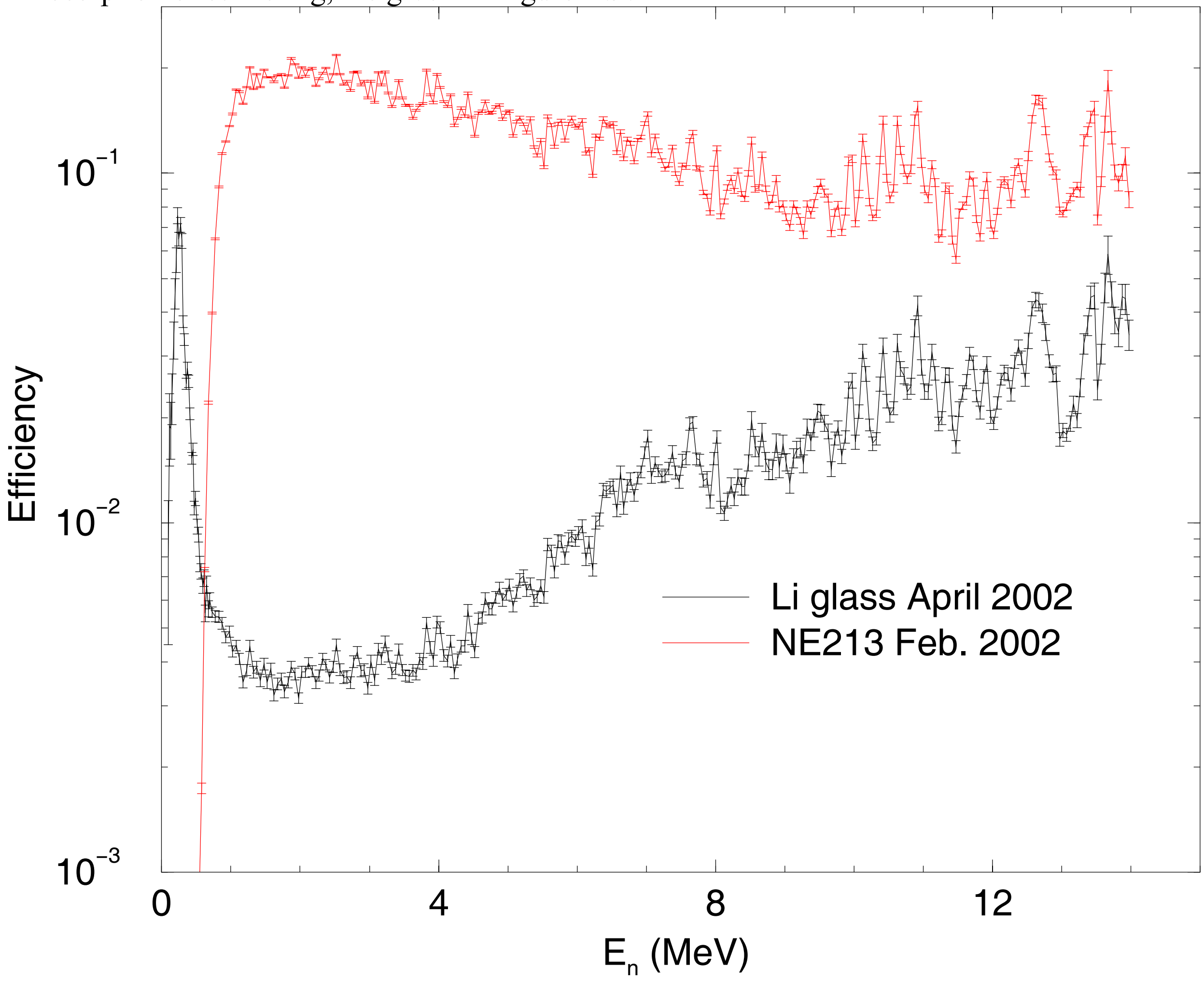

Figure II.9 Neutron detector efficiency determination for the experimental work.

II.5 Experimental Measurements

Analysis of the data proceeded in a manner very similar to that of other recent experiments.[8] The time calibration of the data acquisition system's time-to amplitude converter for all spectra was accomplished by use of both an external time standard and a "random run" for differential non-linearity. The data were analyzed by standard ToF analysis codes. The data channels were converted to ToF in two steps. First, the channels were converted to time using the differential and integral linearity measurements. The differential linearity was determined by measuring the random spectra with starts and stops that are uncorrelated. The counts in each channel then gave a measure of the time width of each channel. The integral linearity was determined by using the precision oscillator of the accelerator and a count down circuit to obtain time marks that were precisely 200 nanoseconds apart (the oscillator time period). This determined the time scale of the spectra with good accuracy. The gamma flash peak was used to determine the absolute scale for the ToF spectra. The experimental data were obtained with the charged-particle beam pulsed at a spacing of 1.6 microseconds; additional data were obtained with a pulsed-beam spacing of 3.2 microseconds to allow us to examine the effect of overlap neutrons (those present from previous beam bursts).

Measurements of the bare neutron source (without the sphere in place) are very important for the success of this study. These measurements are needed to allow correct modeling of the source reaction in the transport codes, the main goals of which are obtaining ToF (energy) and angular distribution measurements for the main neutron peak, neutrons from quantifying contaminants in the gas cell (used for aligning the spectra), and deuteron break-up reactions.

For the first experiment, the measurements were made with a lithium glass detector using the D(d,n) source reaction with deuteron energies of 3.0 and 5.0 MeV emerging from the tungsten foil into the deuterium gas. For both of these energies, bare source data were obtained at angles of 0, 45, 90, 120 and 135 degrees. Also at those energies, thin (small) sphere measurements were made at 0, 90, and 135 degrees.

For the second experiment, measurements of the bare source were made for the ^{15}N(p,n) reaction at angles of 0, 15, 45, 60, 90, 100, 120 and 135 degrees using the NE-213 detector. These measurements were made using 5.1 MeV protons emerging from the tungsten foil into the 3-cm gas cell. Measurements were also made with both the small sphere and the large sphere for this source at angles of 0, 45, 90, 120 and 135 degrees using the NE-213 detector. We also made an additional series of source measurements for the D(d,n) reaction with the bare source and using the NE-213 detector. These measurements were made at angles of 0, 15, 45, 60, 90, 100, 120 and 135 degrees for 3.0 MeV, 5.0 MeV and 7.0 MeV deuterons emerging from the tungsten foil into the gas cell. (Corresponding runs were also made at zero degrees with no gas in the cell to permit an assessment of background effects.) Runs were then made at these three deuteron energies with the large (thick) sphere surrounding the source. For each deuteron energy, measurements were made at 0, 45, 90, 120 and 135 degrees. A large number of angles were used for both the ^{15}N(p,n) and the D(d,n) source reaction work in order to provide detailed source information for the corresponding computer simulations. One conclusion from our work was that taking 12 or more angles would be preferred in future experiments due to the complexity of the D(d,n) spectra. Increasing the energy resolution of the experiments to the point where the energy width of the primary neutron source was limited only by its intrinsic energy width rather than the detector energy resolution may also prove helpful in modeling the source reaction.

The results from our experiments are given below. A summary of the first and the second experiment series is given in Table II.2 and Table II.3 below. Plots of the results from the first experiment are given in Figures. II.10-13. The results from the second experiment are shown in Figures. II.14-22.

Table II.2 Summary of the first experiment in April 2001.

Neutron Source Reaction	***Angles(Degrees)***
D(d,n) source spectrum, E_d = 3.0 MeV	0,45, 90, 120, 135
D(d,n) source spectrum, E_d = 5.0 MeV	0,45, 90, 120, 135
D(d,n) E_d = 3.0 MeV, Thin Sphere	0, 90, 135
D(d,n) E_d = 5.0 MeV, Thin Sphere	0, 90, 135

All energies refer to energy of the beam striking the gas. All measurements were performed with a lithium glass detector with a source to detector center distance of 5.004 m.

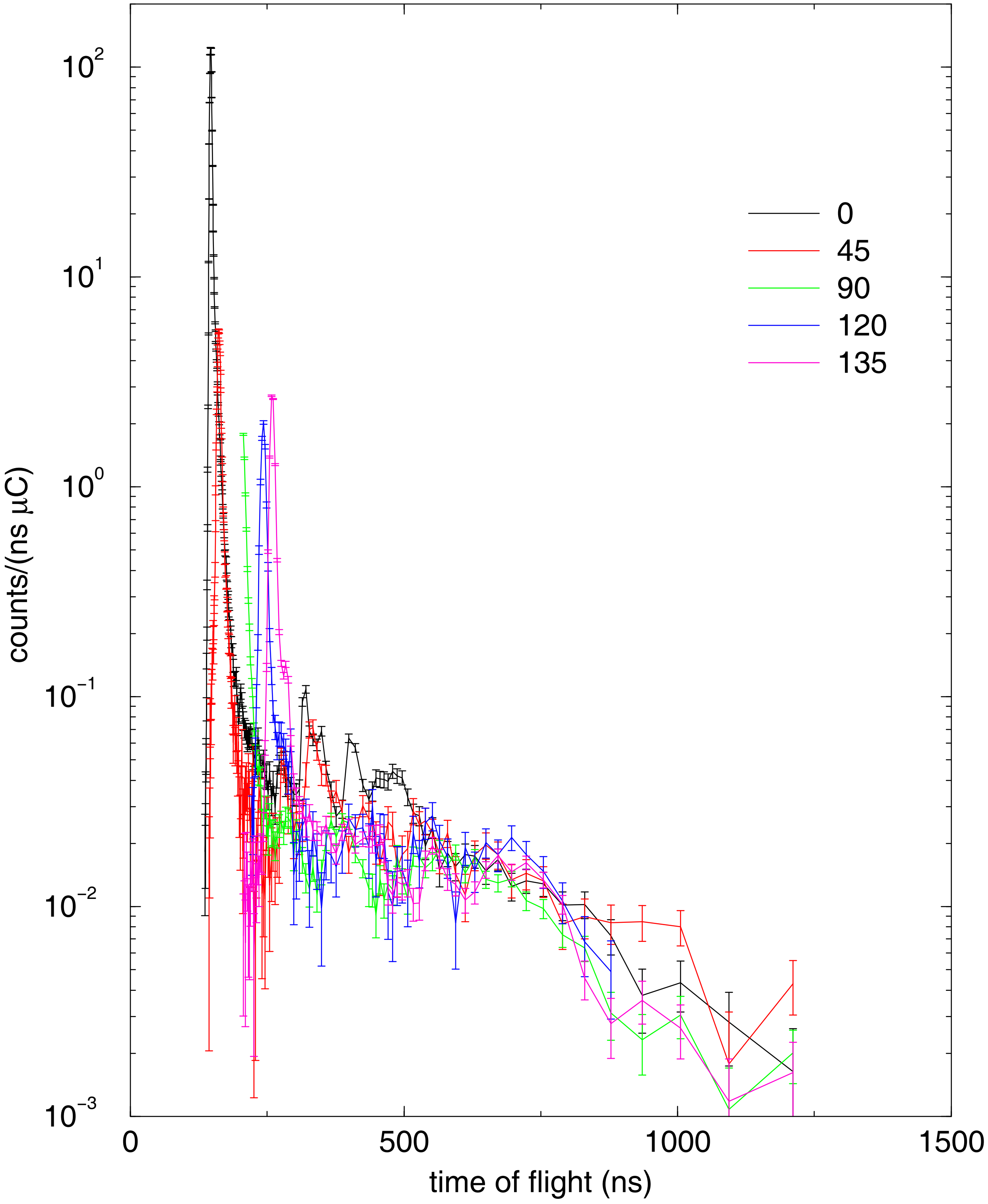

Figure II.10 Source data for the D(d,n) reaction with 3.0 MeV deuterons incident on the gas.

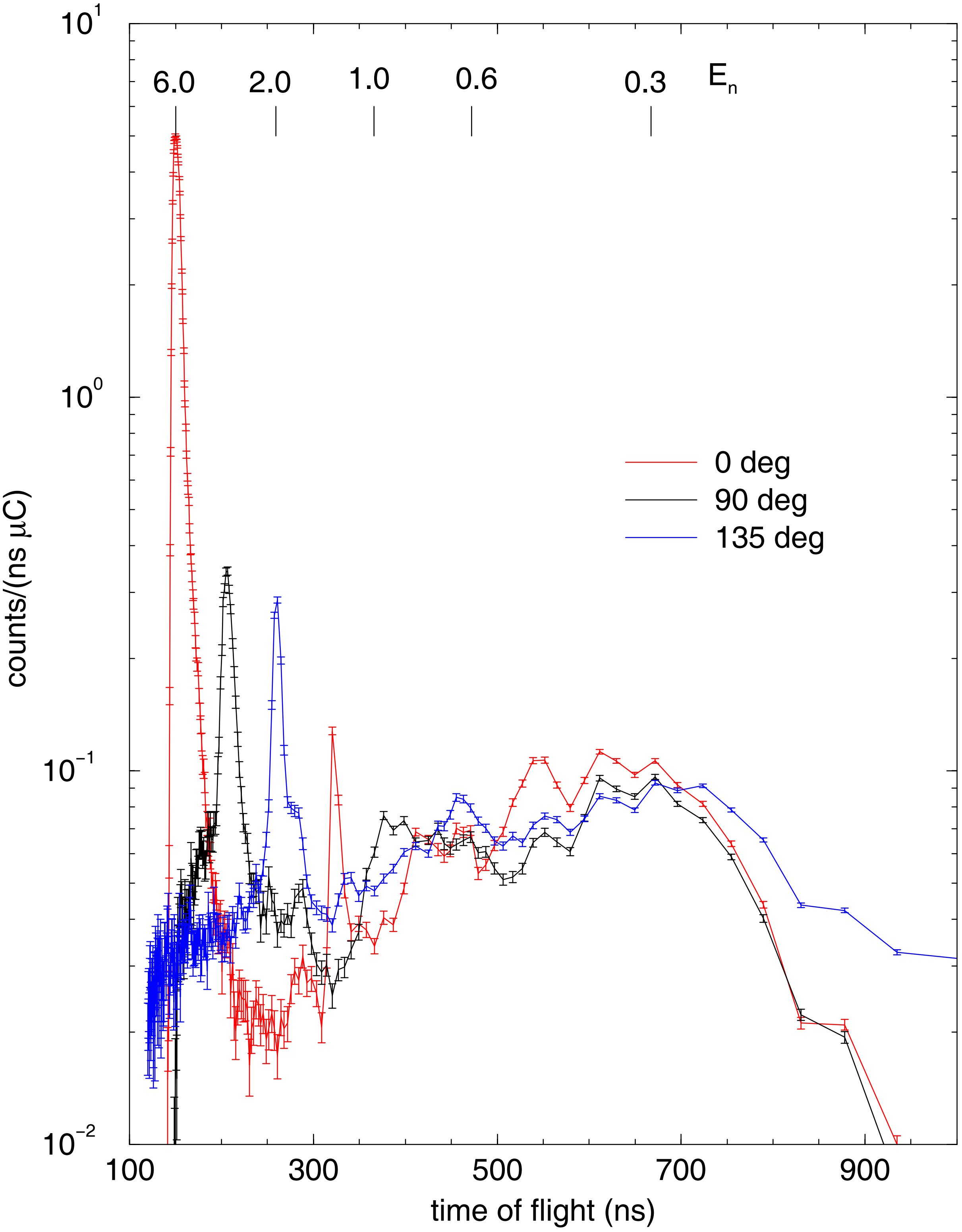

Figure II.11 The "sphere-on" spectra obtained with the small (3-cm-thick) sphere and the D(d,n) source reaction with 3.0 MeV deuterons incident on the gas.

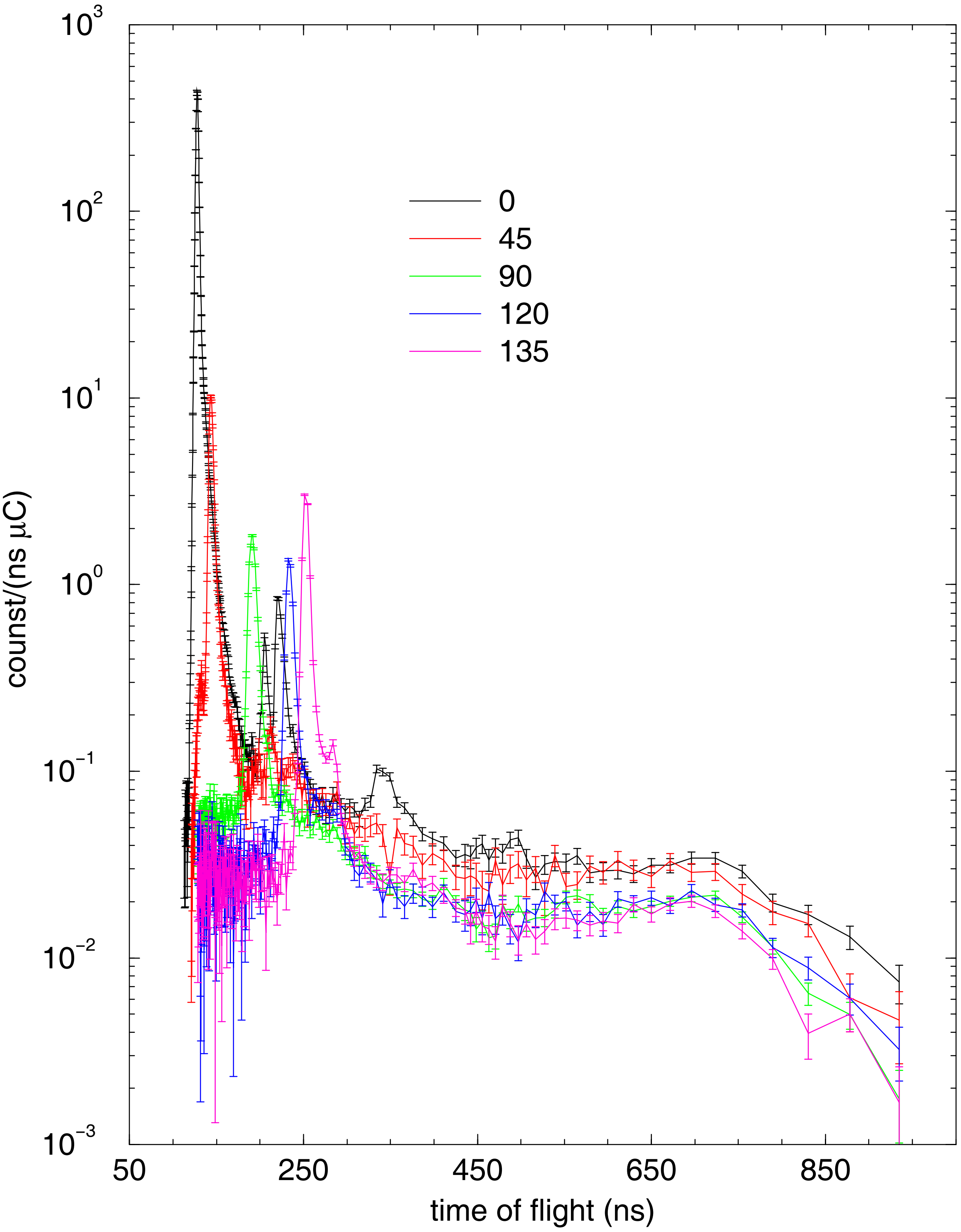

Figure II.12 Source data for the D(d,n) reaction with 5.0 MeV deuterons incident on the gas.

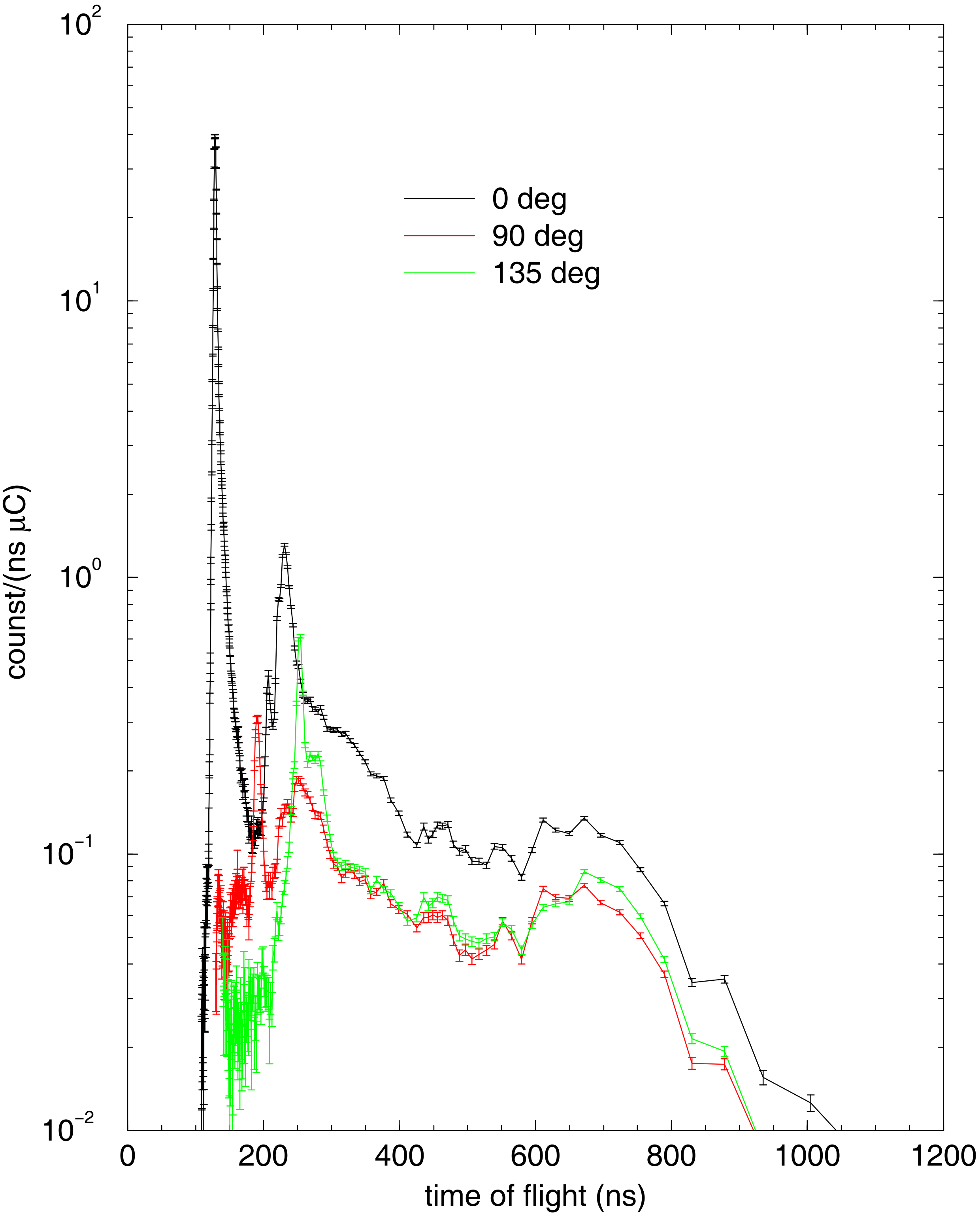

Figure II.13 The "sphere-on" spectra obtained with the small (3-cm-thick) sphere and the D(d,n) source reaction with 5.0 MeV deuterons incident on the gas.

Table II.3 Summary of the second experiment in February 2002.

Neutron Source Reaction	*Angles(degrees)*
^{15}N(p,n), source spectrum, E_p = 5.1 MeV	0,15,45,60,90,100,120,135
D(d,n), source spectrum, E_d = 3.0 MeV	0,15,45,60,90,100,120,135
D(d,n), source spectrum, E_d = 5.0 MeV	0,15,45,60,90,100,120,135
D(d,n), source spectrum, E_d = 7.0 MeV	0,15,45,60,90,100,120,135
^{15}N(p,n), Thin Sphere in, E_p = 5.1 MeV	0,45,90,120,135
^{15}N(p,n), Thick Sphere In, E_p = 5.1 MeV	0,45,90,120,135
D(d,n), Thick sphere in, E_d = 3.0 MeV	0,45,90,120,135
D(d,n), Thick sphere in, E_d = 5.0 MeV	0,45,90,120,135
D(d,n), Thick sphere in, E_d = 7.0 MeV	0,45,90,120,135
All energies refer to energy of the beam striking the gas. All measurements shown were performed with a NE213 detector, 5.08 cm deep and 12.7 cm in diameter, with a source-to-center-of-detector distance 5.055 m.	

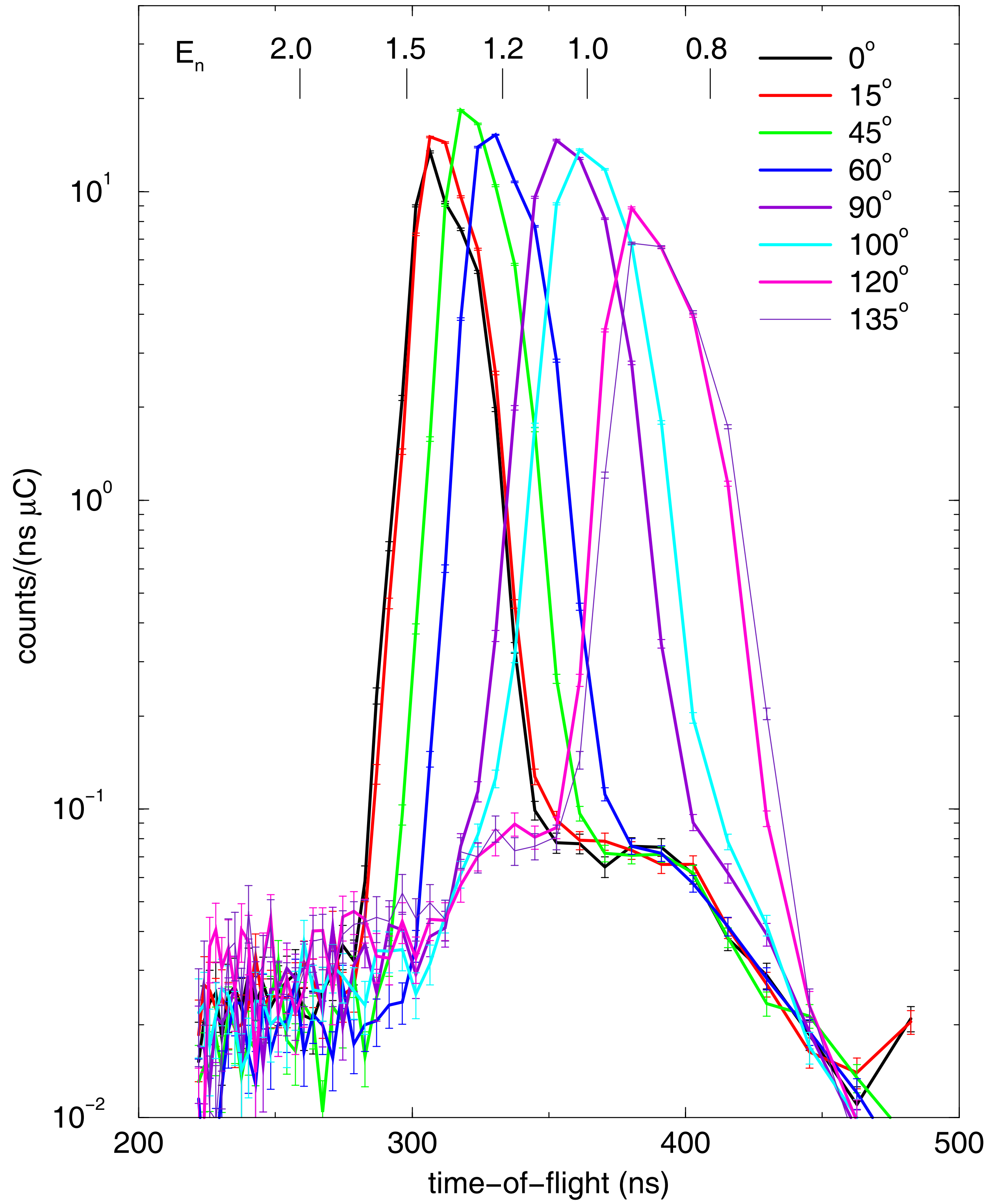

Figure II.14 Shown is the source spectrum for the 15N(p,n) reaction with 5.1 MeV protons incident on the gas.

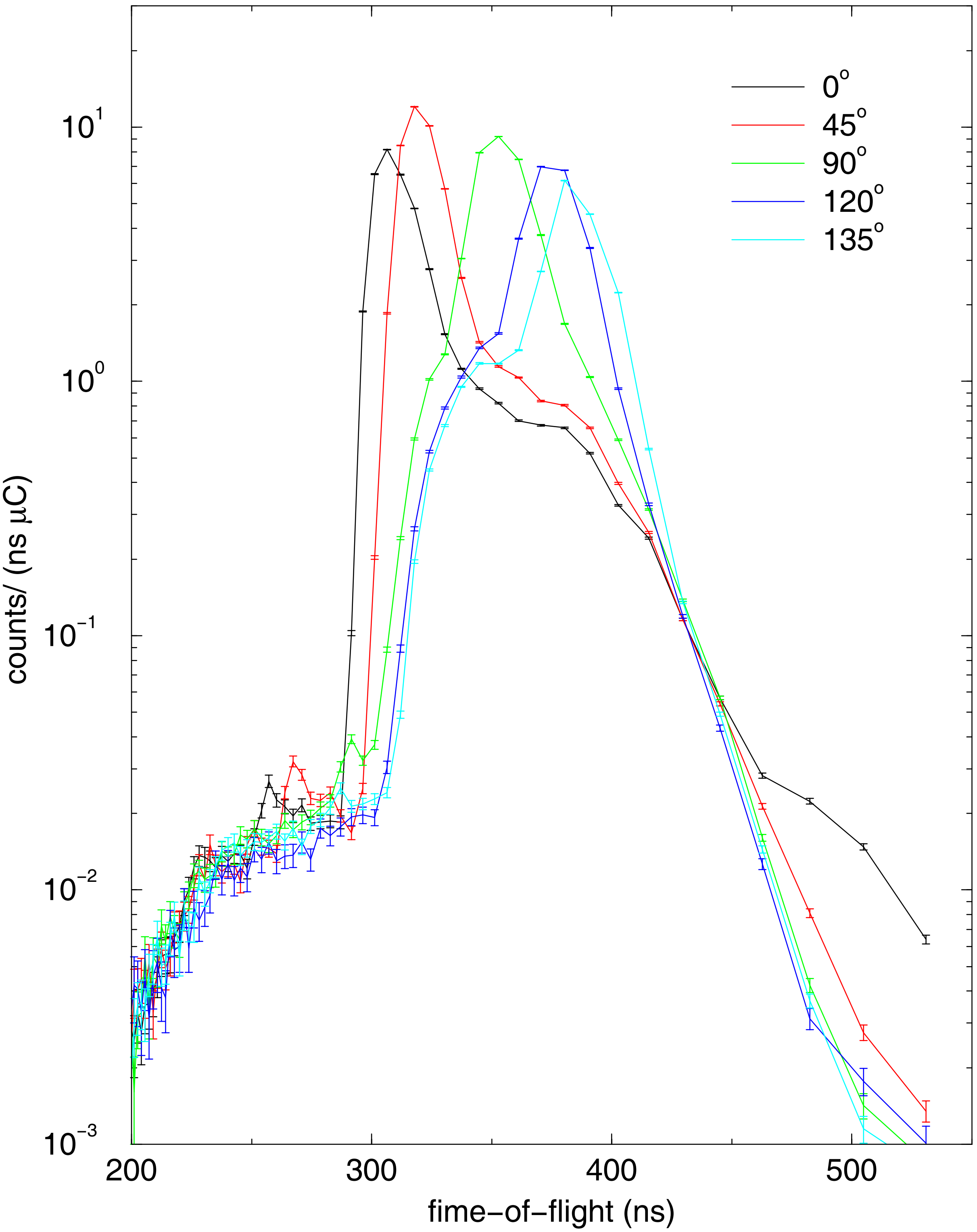

Figure II.15 The "sphere-on" spectra obtained with the small (3-cm-thick) sphere and for the 15N(p,n) reaction with 5.1 MeV protons incident on the gas. All of the measured angles are shown.

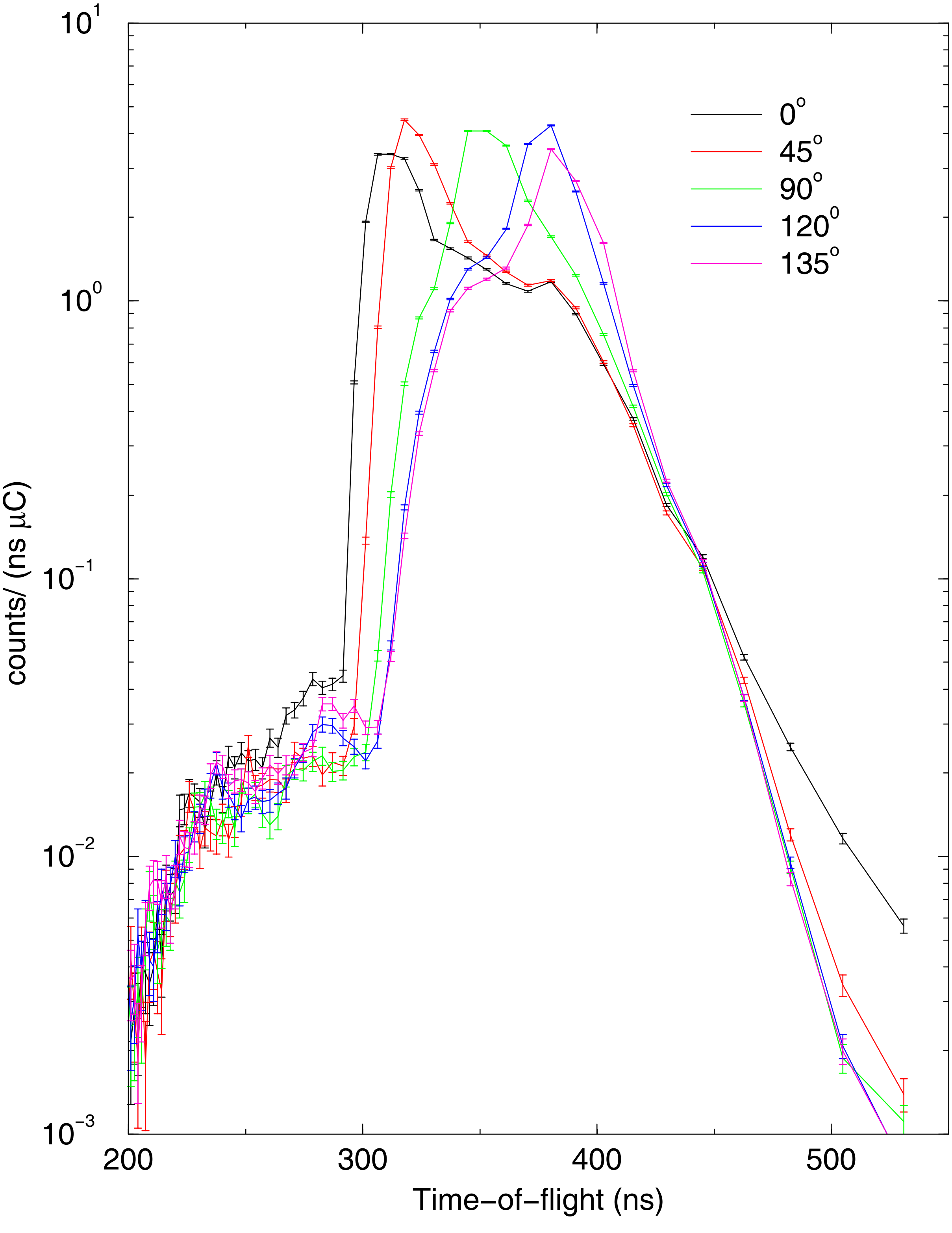

Figure II.16 The "sphere-on" spectra obtained with the large (8-cm-thick) sphere and for the 15N(p,n) reaction with 5.1 MeV protons incident on the gas. All of the measured angles are shown

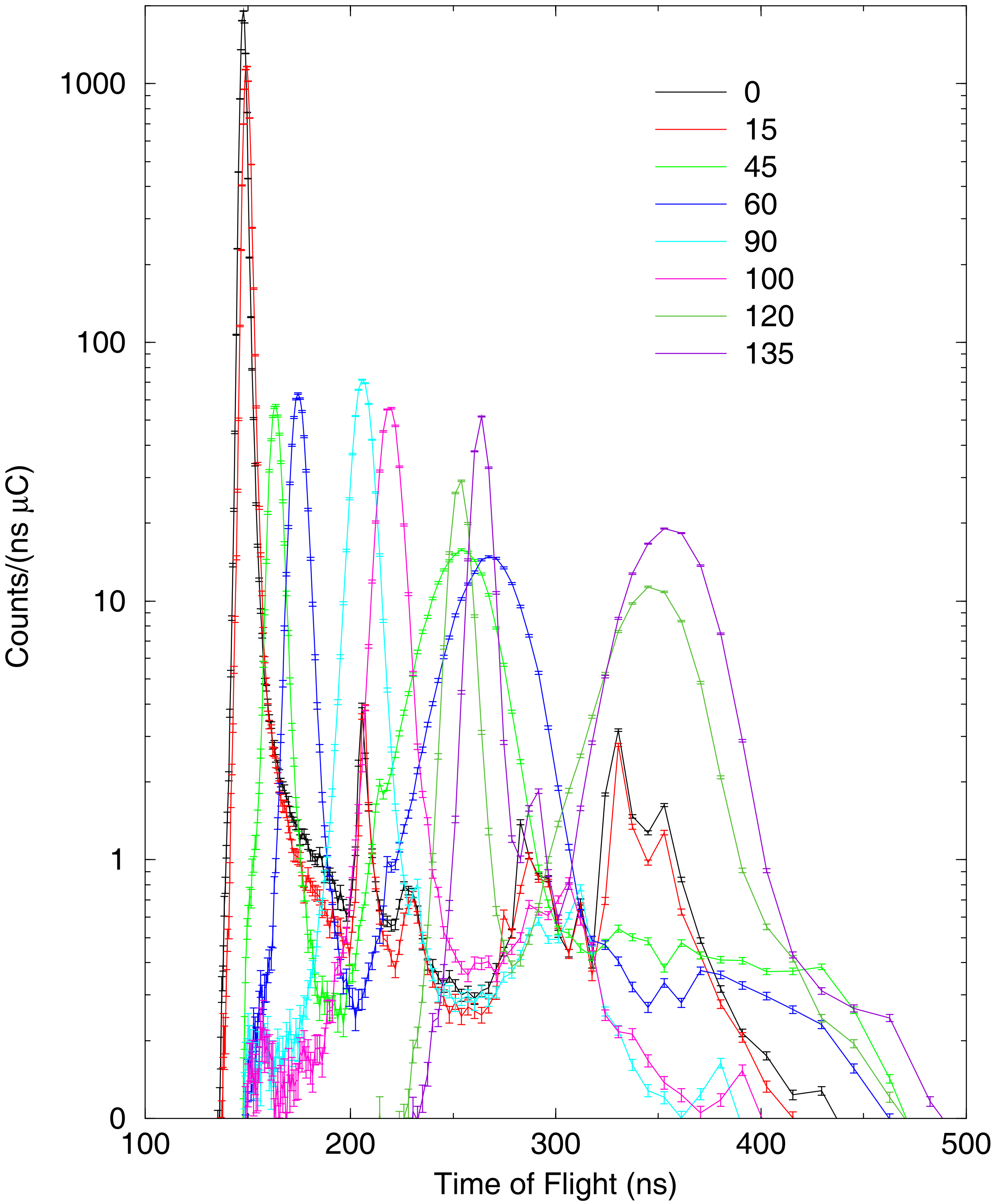

Figure II.17 Shown is the source spectrum for the D(d,n) reaction with 3.0 MeV deuterons incident on the gas. All of the measured angles are shown.

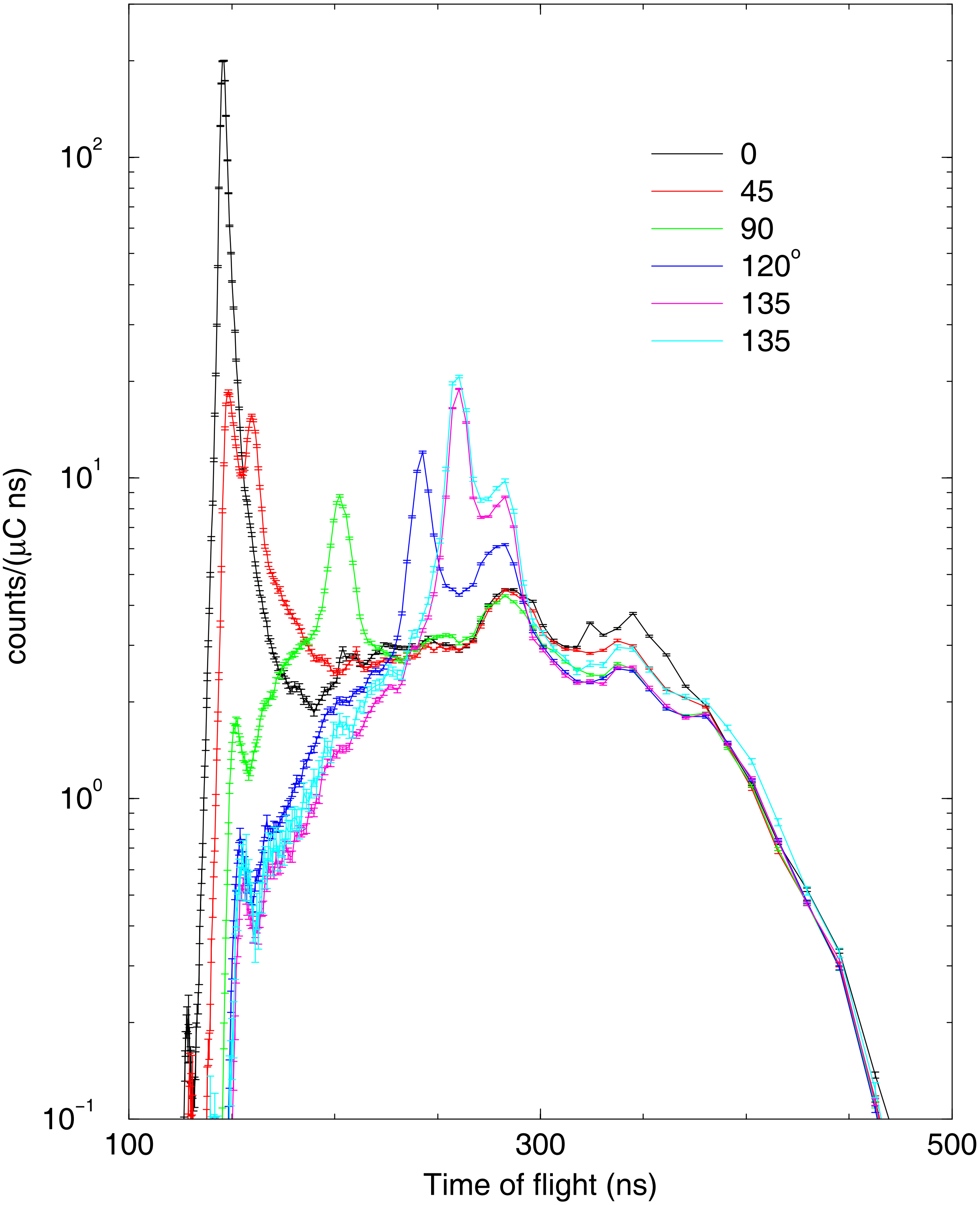

Figure II.18 The "sphere-on" spectra obtained with the large (8-cm-thick) sphere and for the D(d,n) reaction with 3 MeV deuterons incident on the gas.

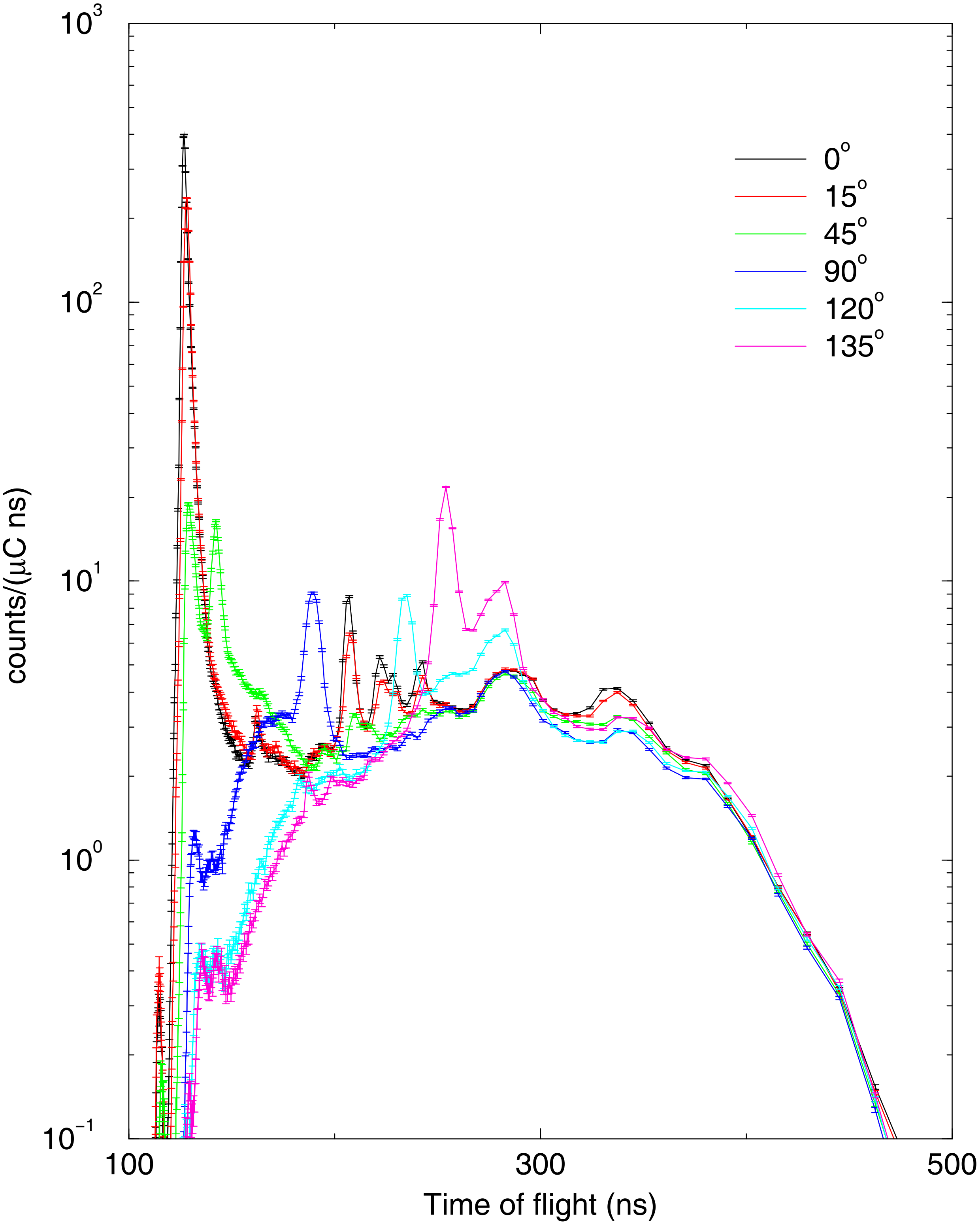

Figure II.19 Source shown is the source spectrum for the D(d,n) reaction with 5.0 MeV deuterons incident on the gas. All of the measured angles are shown.

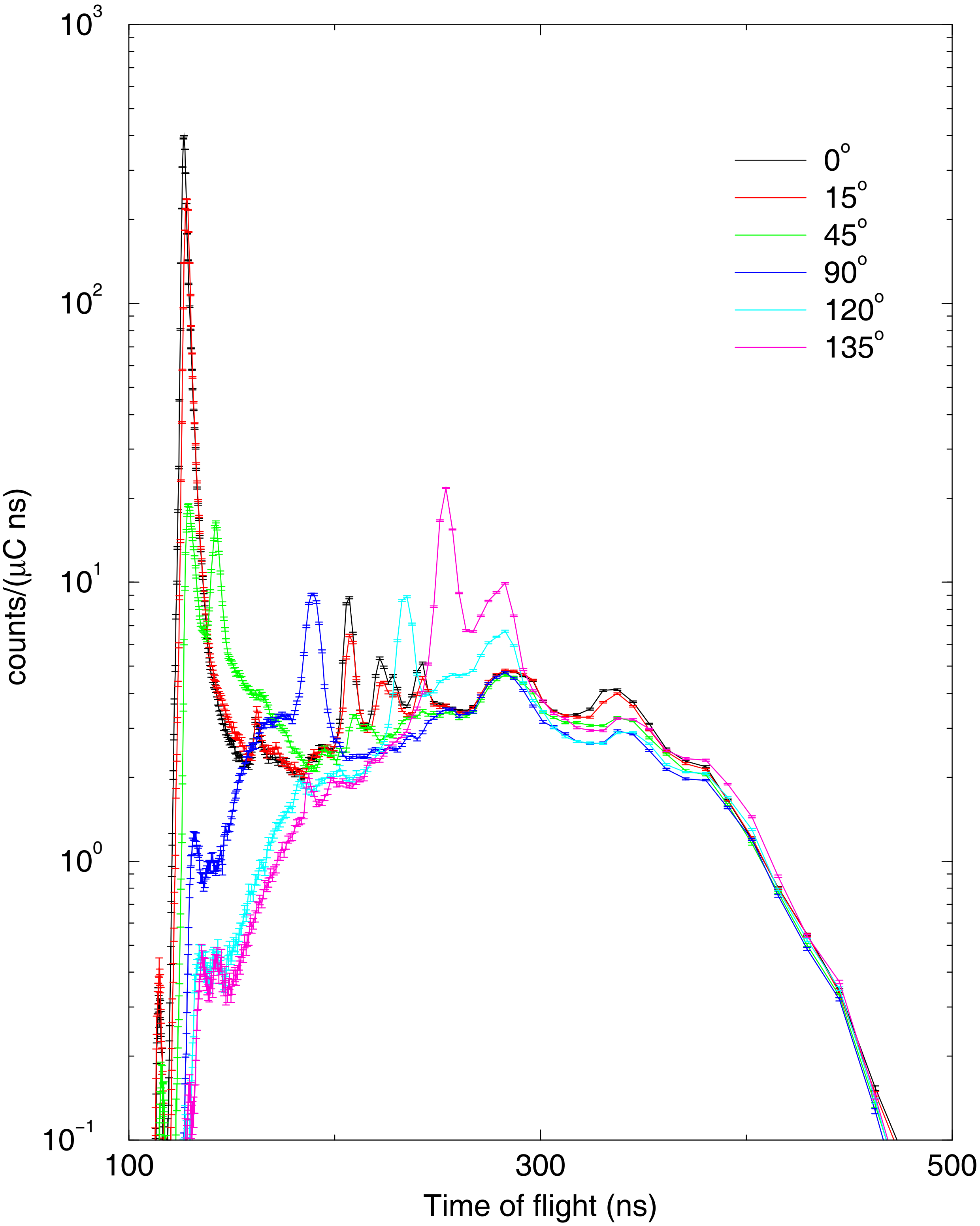

Figure II.20 The "sphere-on" spectra obtained with the large (8-cm-thick) sphere and the for the D(d,n) reaction with 5 MeV deuterons incident on the gas. All of the measured angles are shown

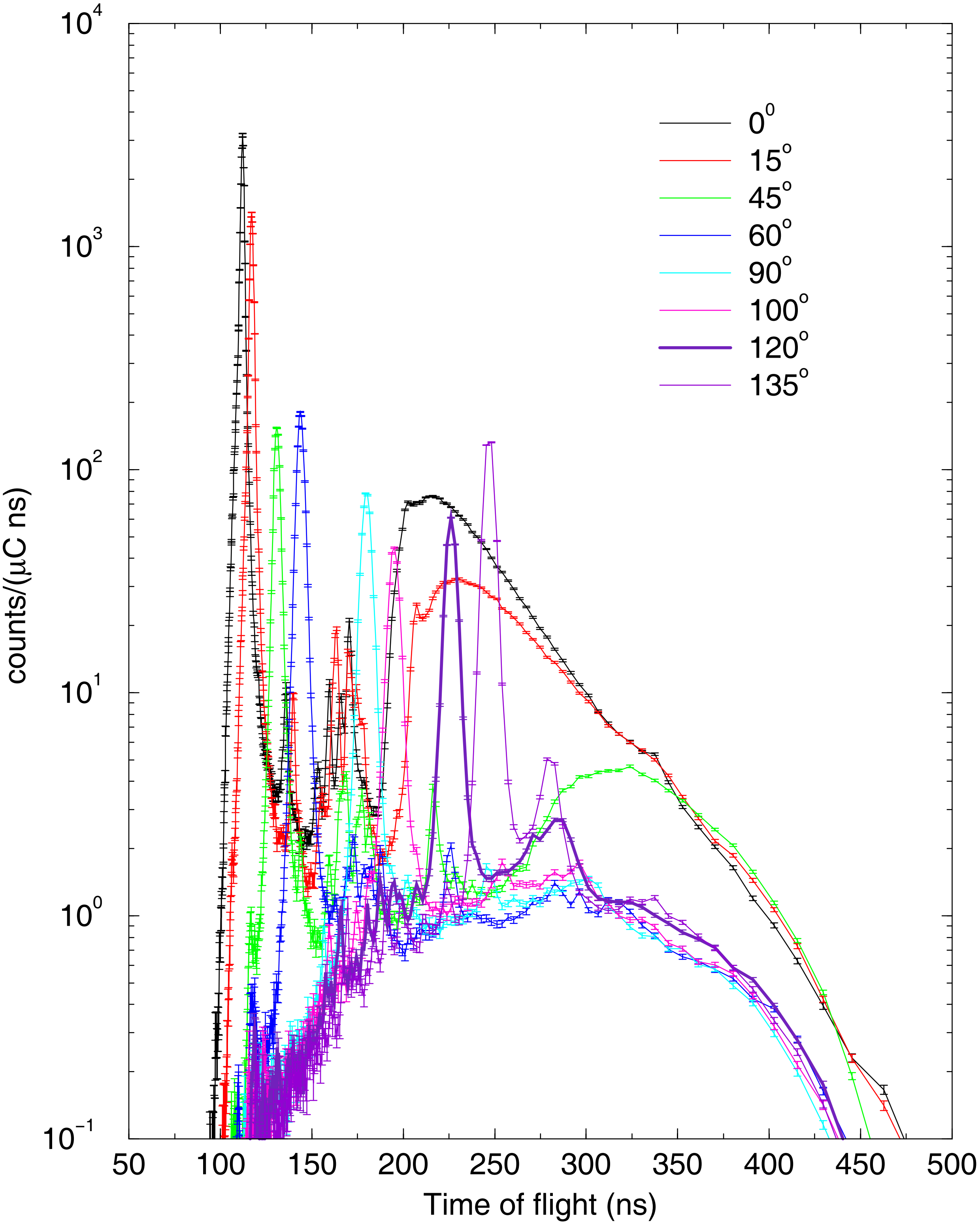

Figure II.21 Shown is the source spectrum for the D(d,n) reaction with 7.0 MeV deuterons incident on the gas. All of the measured angles are shown.

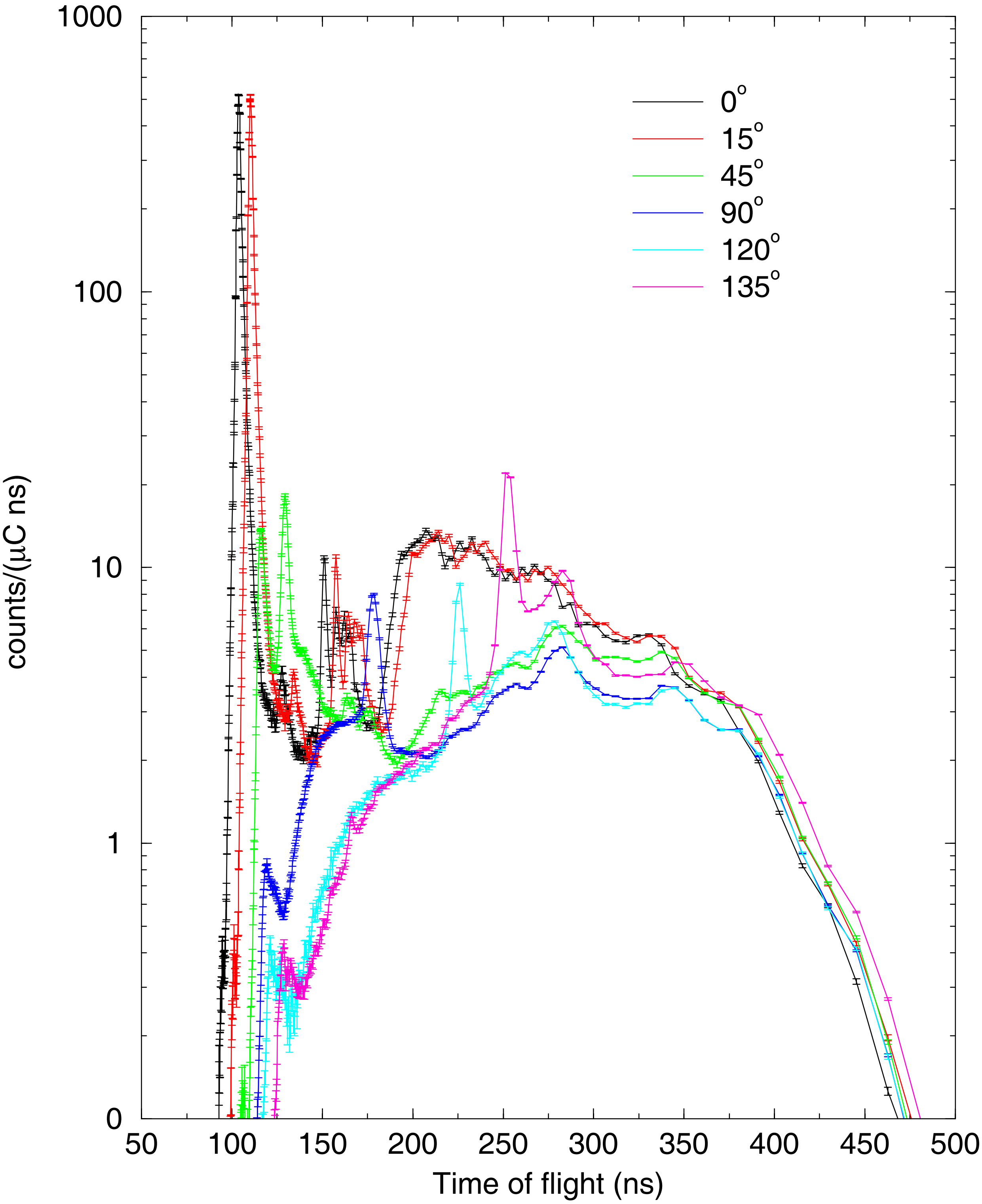

Figure II.22 The "sphere-on" spectra obtained with the large (8-cm-thick) sphere and for the D(d,n) reaction with 7 MeV deuterons incident on the gas. All of the measured angles are shown

Almost all of the data from the second experiment were taken using a single NE213 neutron detector positioned at a distance of 5.055 meters from the center of the source gas cell to the center of the detector. Some data were taken with a lithium glass detector: this data consisted of efficiency data and a measurement at 90 degrees with the thin iron sphere and the $^{15}N(p,n)$ source reaction at 5.1 MeV incident on the gas.

Some difficulties were found in the analysis of the data obtained with the iron spheres in place, the so-called "sphere-on" data. The time dependent gammas from the $(n,n'\gamma)$ reaction occurring in the spheres interfered with the determination of the precise position of the gamma flash peaks. We used three methods to overcome this problem. The first method used the gamma flash originating from a collimator upstream of the gas cell as a relative determination of the time scale. The absolute scale was then determined by comparison to the same gamma flash from the collimator obtained from a spectrum taken with the sphere off, where the gamma flash of the gas cell was easily determined. A second method was to align the narrow neutron peaks arising from impurities contained in the source cell gas for both sphere-on and sphere-off measurements by adjustment of the gamma flash position used in the analysis codes. A third method has been considered more recently and is still under investigation. This method uses the fact that the true gamma flash from the gas cell is much higher in energy than the gammas from the iron sphere. A cut was made on the pulse height to allow only the high energy gamma rays from the gas cell to be accepted. The result of this method for a single set of thick iron sphere data is shown in Figure II.23. We expect that most of the problems of determining the position of the gamma peak will be solved by this approach.

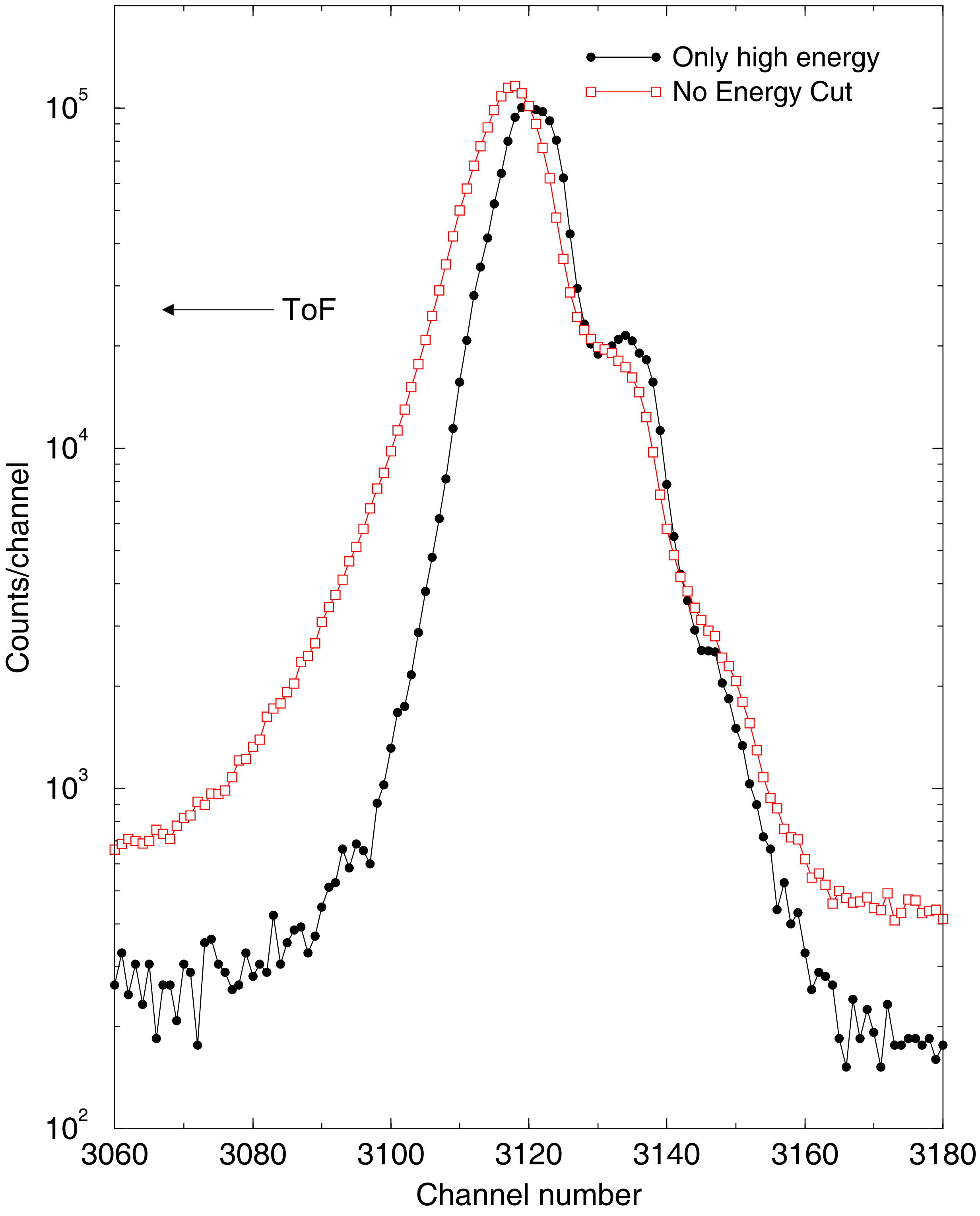

Figure II.23 Comparison of the gamma peak region with all of the gamma rays allowed, and with only the most energetic gamma rays allowed. The spectra have been renormalized to allow the differences in position to be shown. The time calibration is ~0.6 ns/channel**.**

III. Computational approach and results

III.1 Introduction

To optimize the experimental setup and evaluate how well the prevailing interaction cross sections predict neutron transport through thick-section steel, we performed a series of detailed particle transport simulations. Because of the special characteristics and objectives associated with this problem, the available particle transport theory methods and codes conventionally employed are limited and new techniques and methodologies were developed. Commonly, the iron sphere ToF experiments involve the use of monoenergetic, or well-characterized source spectra, while the current project uses different source spectra generated by charged-particle induced nuclear reactions using an accelerator. Moreover, in order to improve our confidence in the extracted experimental data, we have examined various experimental setups by changing the source reaction, charged-particle energy, and by changing the angle between the charged-particle and neutron beam line directions.

The remainder of this section is organized as follows: Section III.2 discusses the particle transport methodology developed for this project; Section III.3 discusses the use of the new tally option for optimization of the experimental setup; and Section III.4 compares and discusses the experimental and calculation results for various experimental setups.

III.2 Particle transport methodologies

To simulate a ToF experiment, commonly standard Monte Carlo software is used; however, for this project we have developed new capabilities for the Monte Carlo method, and examined the use of the deterministic methods, which can be more effective, especially when performing sensitivity studies.

III.2.1 Monte Carlo Method

The standard Monte Carlo method is generally computationally intensive, especially if detailed information is needed. We have used the method for both optimization of experimental setup and also for simulation and analysis of the ToF experiments.

III.2.1.1 New tallying option for the Monte Carlo MCNP code

In order to use the Monte Carlo method for optimization, we developed a new tallying capability[9] for the MCNP code[10]. This tallying option provides detailed information about the history of the particles detected by the detector. For the current project, we are interested in a combination of iron shell thickness and energy of source neutrons which results in the largest number of particles which have gone through inelastic scattering within the iron shell (target), and subsequently have reached the detector.

While tracking the neutrons as they travel through the model, a detailed array of information including collision type, energy, scattering angle, position and time is compiled that enables the neutrons that reach the detector to be categorized based on the type of interaction they have undergone within the iron shell. From this information, the collided and uncollided neutron flux components are calculated at the detector.

III.2.1.2 Monte Carlo Models for simulation of ToF experiments

The ToF experiment used for this project is composed of a source, a target, a collimator, a concrete wall with an opening hole, and a tunnel which houses a detector. Figure II.1 shows a schematic of the ToF experiment.

In order to simulate this experiment it is necessary to prepare a source distribution, represent the physical model as accurately as necessary, and setup a model for the detector. In this section, we will discuss in detail these items.

Preparation of source distribution

As discussed in the experimental section of this report, the neutron source is generated through proton-nitrogen $^{15}N(p,n)$ and deuteron-deuterium D(d,n) interactions.

The first attempt at providing a detailed source came from the use of the DROSG neutron source reaction code[11]. The DROSG code is capable of providing differential cross section data for the beam energies and reactions chosen resulting in a source distribution providing one neutron energy for each source angle. Figure III.1 compares angular spectra from the DROSG code with experimental data for the D(d,n) reaction. The angular distribution closely follows the DROSG behavior, however, this is not observed for the $^{15}N(p,n)$ source as is shown in Figure III.2. This difficulty along with the fact that ToF spectra for the experiments without the iron sphere clearly show neutrons from more than just the $^{15}N(p,n)$ source reaction makes the DROSG code alone ineffective for this project.

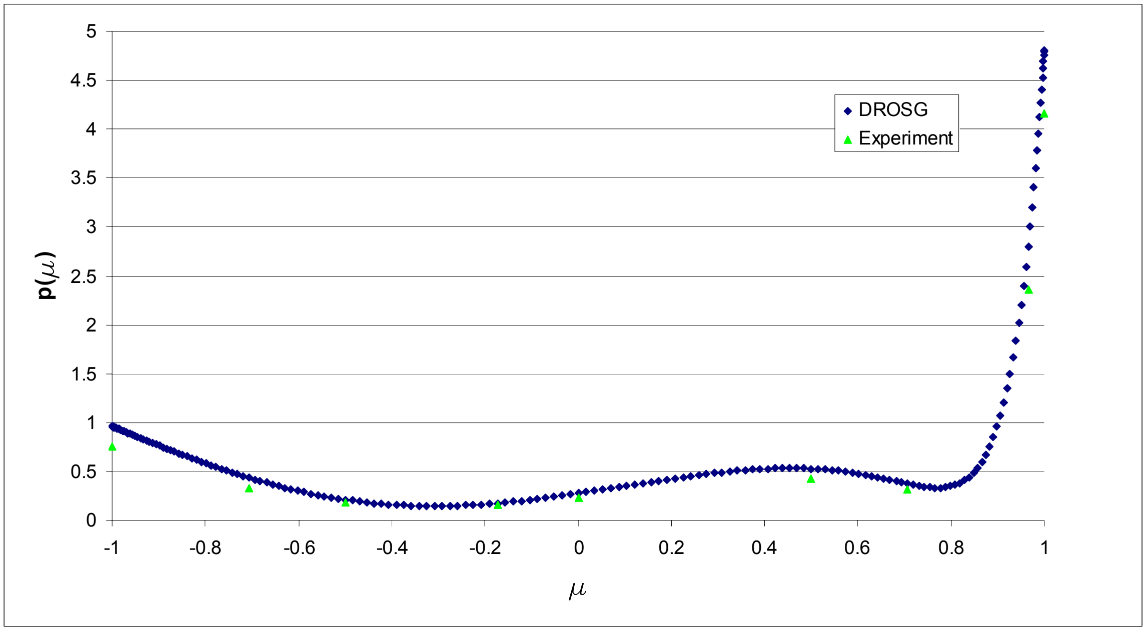

Figure III.1 The 5 MeV D(d,n) DROSG versus experimental source angular distribution comparison **.**

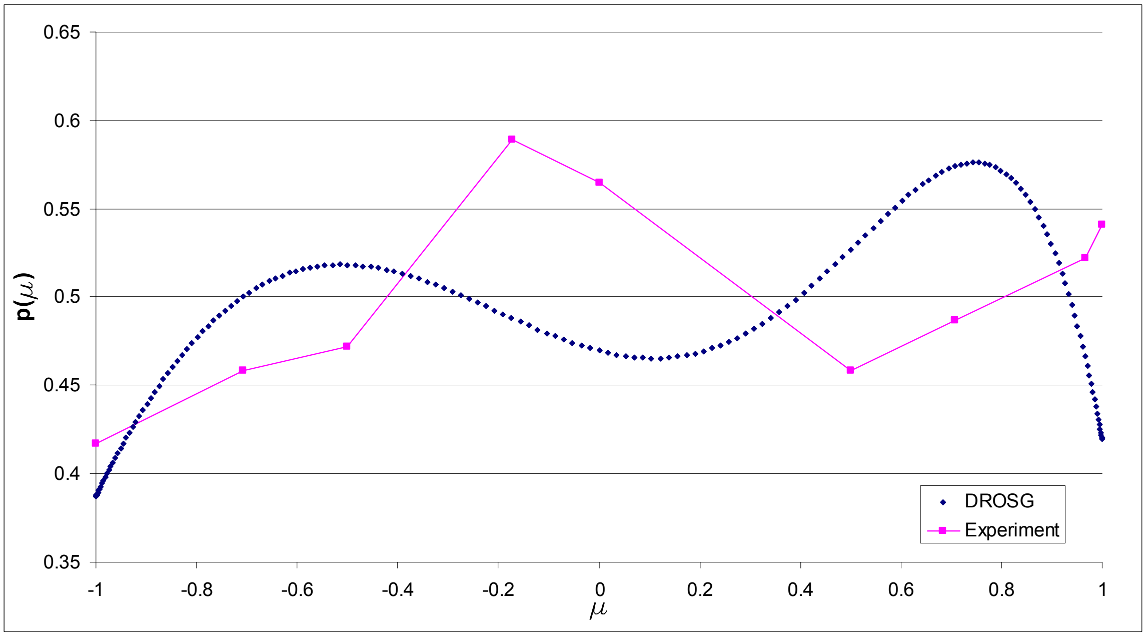

Figure III.2 Comparison of the ^{15}N(p,n) DROSG prediction to the experiment source angular dependence.

So, rather than a theoretical approach, it was decided to utilize the experimental data for generating the source distribution. It was assumed that the neutron ToF spectrum obtained from the 'sphere off' cases represent the uncollided neutrons. Considering the distance to the detector a known quantity, the ToF spectra obtained for the sphere off runs is converted directly to energy spectra using relativistic kinetic energy considerations. This procedure is repeated once for each angle, charged-particle energy and beam reaction to characterize the source.

To derive a detailed angular distribution for the source, while having limited experimental data, an interpolation/extrapolation methodology was developed as discussed below.

A computer code in FORTRAN 90 was developed for preparation of the angular and energy dependent source distribution. This code treats the experimental spectra by incorporating the effect of detector resolution. Figure III.3 shows the number of time resolution intervals per experimental bin size.

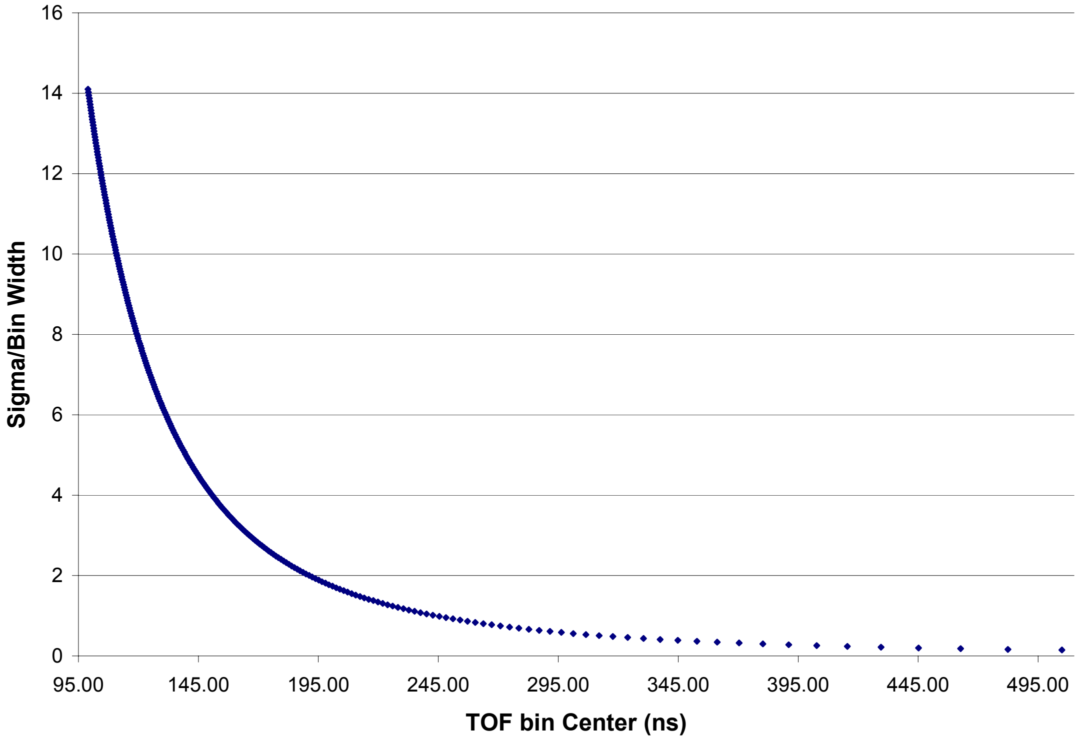

Figure III.3 Distribution of the number of resolution intervals per experimental bin size.

To incorporate the effect of resolution, we redistribute the experimental data 'normally' about the center of each time bin using the following formulation accounting for two resolution components determined from a gamma peak width estimate and physical detector size component as given by:

$$\sigma^2 = \gamma^2 + \left(\frac{\mathrm{Dt}}{2(d)} \right)^2 . \qquad \text{(III.1)}$$

Where,

γ = gamma peak width component

D = distance a particle travels through the detector

t = time of flight

d = flight path

Figure III.4 shows the 3 MeV zero-degree D(d,n) spectrum before and after redistribution.

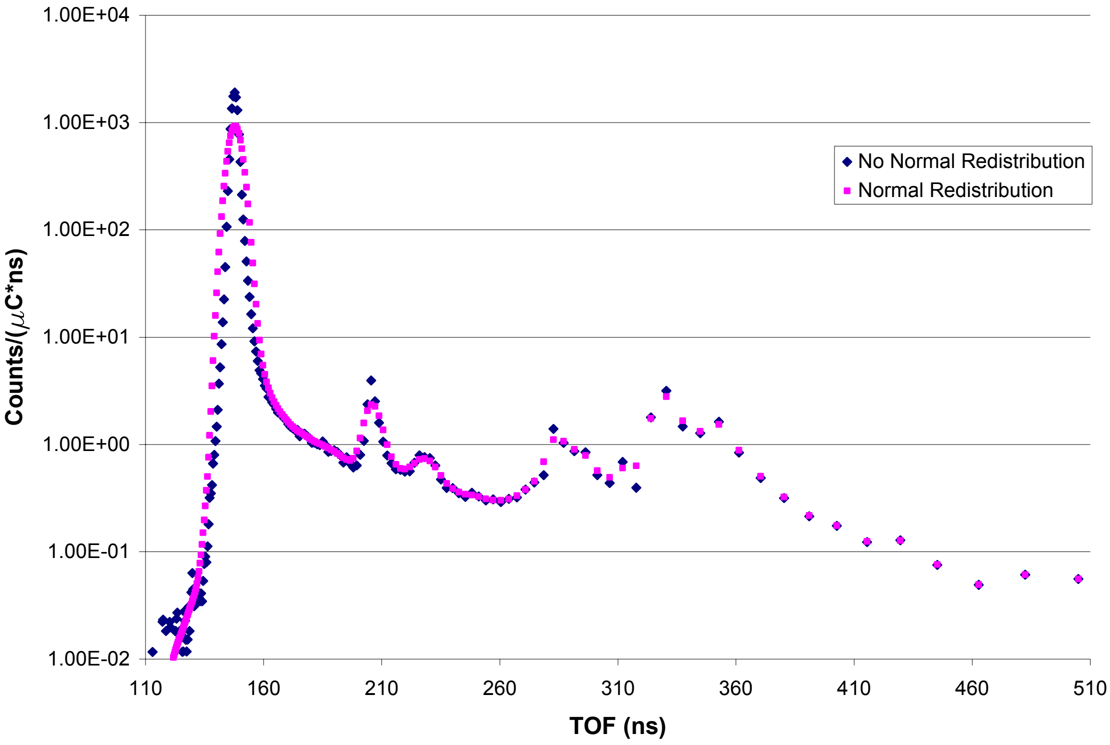

Figure III.4 The comparison of the 3 MeV D(d,n) source spectra before and after redistribution comparison.

Following accounting for the detector resolution, the data are then converted from counts/(μC ns) to neutrons/(μC ns) using the detector efficiency.

The interpolation/extrapolation procedure begins by first locating the ToF location of the maximum of each bounding spectrum (for example, the 0 and 15 degree spectra for any angle between 0 and 15 degrees). Then, a linear fit in angle is used to generate a peak (maximum) value for each spectrum desired between the bounding spectra. Note that the peak is always set in the center of the time bin. Figure III.5 shows an example for determination of the interpolated peak referred to as M-int.

Since eight experimental spectra are available, seven interpolation regions are created. ToF spectra are obtained in one degree increments. For the interpolation region one (0 to 15 degrees), there are 14 newly created time of flight spectra.

To complete the interpolated spectrum, a linear combination of the bounding spectra is used. Relative percentages of the peak value for each bounding spectrum are obtained for each side of the peak value. For example, in Figure III.5 for bounding spectrum one (0 Deg.), a value of A1/M1 is obtained for the first point to the left of the peak, similarly, a value of A2/M2 is obtained for bounding spectrum two (45 Deg.).

These percentages for each bounding spectra are then weighted linearly in angle using the angular separation distance between the newly generated spectrum and the bounding spectra. The new percentage is then multiplied by the newly generated peak maximum. In Figure III.5 this value is A-int.

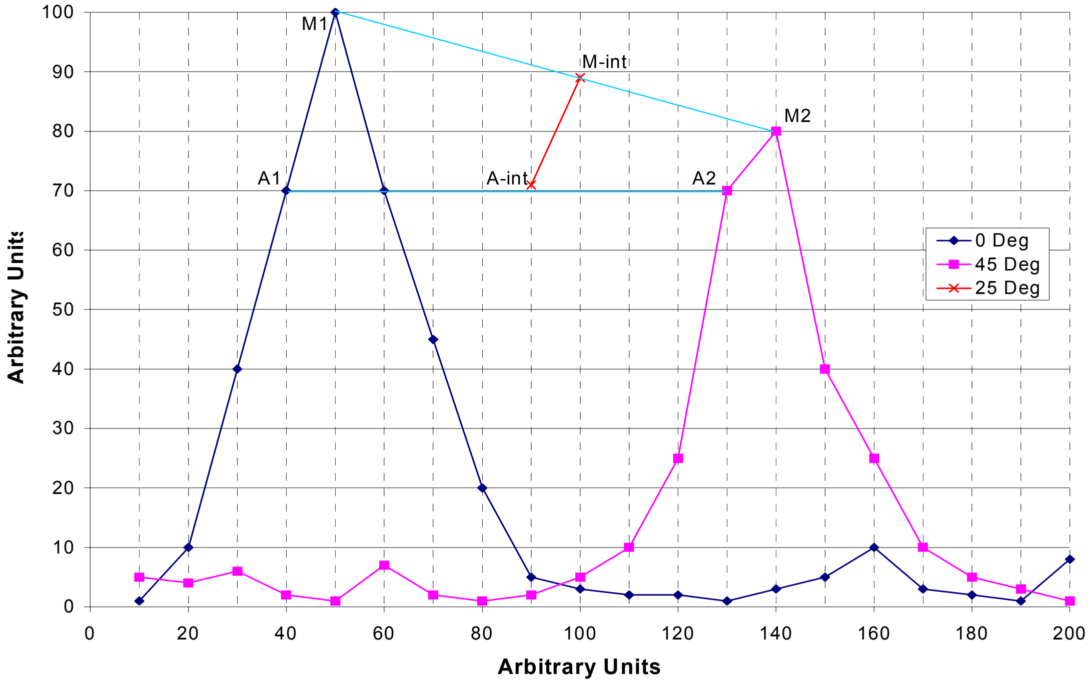

Figure III.5 Source Generation Interpolation Schematic.

This process is repeated for all spectra until a complete angular and energy dependant source distribution is obtained over the range from 0 to 135 degrees.

The resulting interpolated spectra fit well in the peak region, however, upon further inspection of the separate calculated ToF spectra, it can be seen that beyond the main peak region, secondary peaks are present which do not appear to have the same behavior as the primary peak in time (i.e a shift in time occurs as the angle is increased). Hence, a linear interpolation in terms of angle is performed considering no time-shift for the secondary peaks.

Figure III.6 shows the interpolated spectrum at a 52 degree angle for the 3 MeV D(d,n) source data using spectra at 45 and 60 degrees. Also shown is the same spectrum when linear interpolation is not used outside of the main reaction.

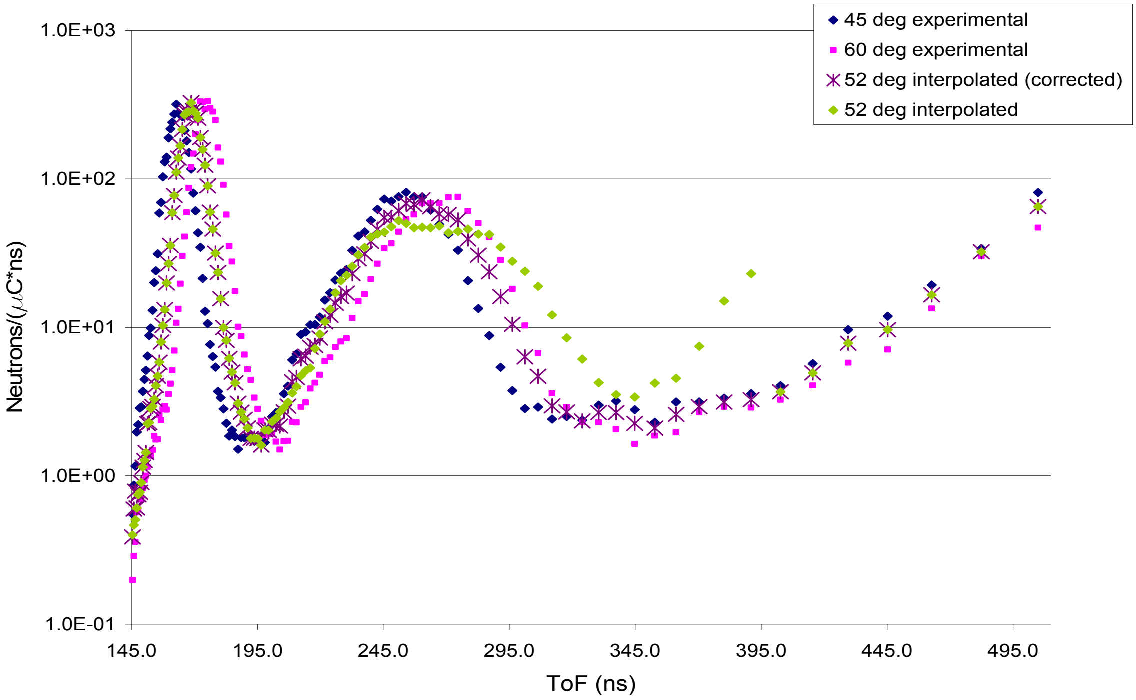

Figure III.6 The 3 MeV D(d,n) interpolated spectrum.

The corrected spectrum appears to represent the bounding spectra behavior more accurately.

To provide data beyond 135 degrees, extrapolation is employed using the same approach as was used for the interpolation. The difference in this procedure is that the newly generated spectrum is not bounded, and only the 135 degree spectrum is used to provide data on both sides of the main peak. The peak values are obtained as before except for utilizing the 120 and 135 degree spectra providing a linear fit. The interpolated spectrum is renormalized by calculating its total number of neutrons from a linear combination of the bounding spectra.

Figure III.7 shows the available data for the 5 MeV D(d,n) experiment corrected for detector resolution and efficiency.

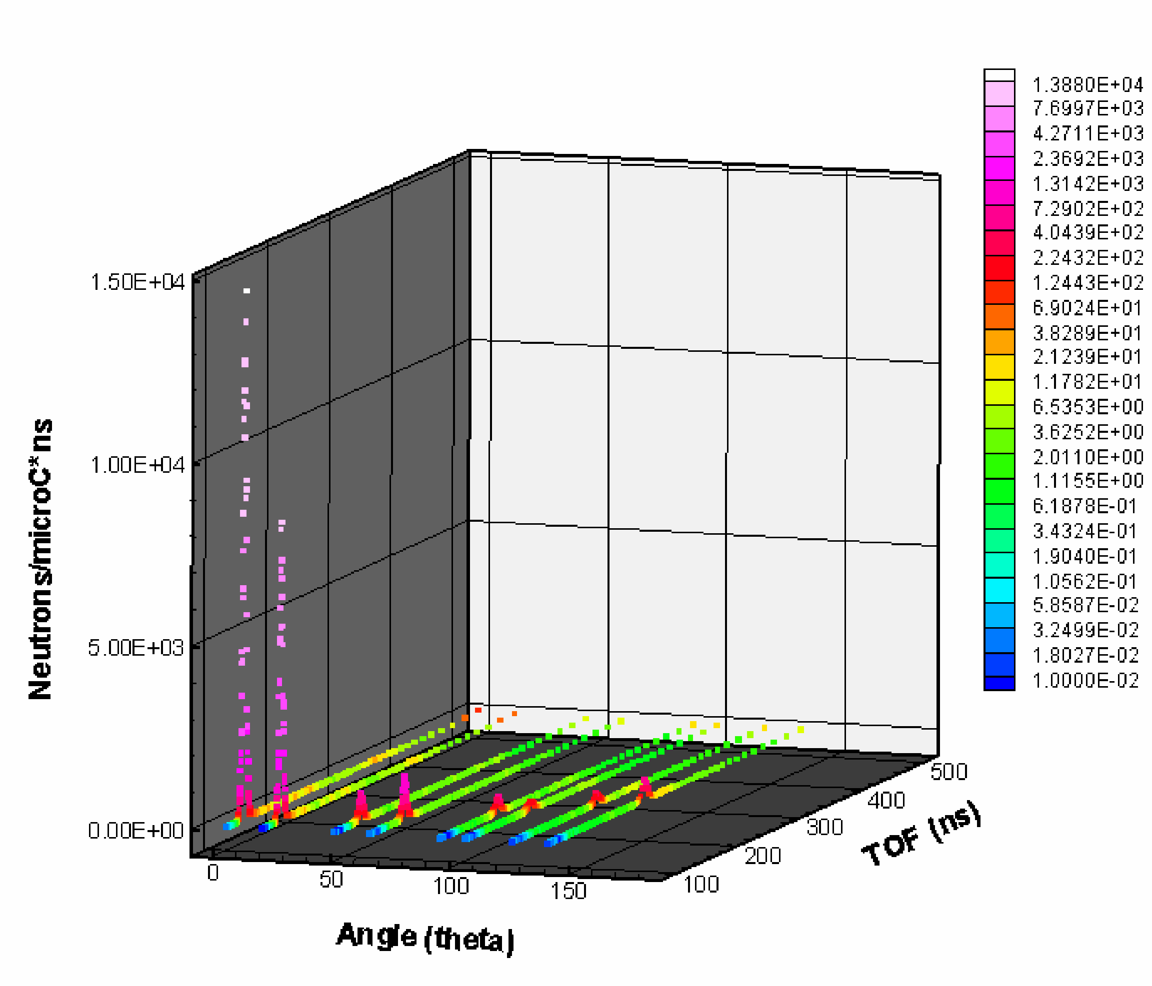

Figure III.7 Experimental source distribution for the 5 MeV D(d,n) reaction.

The complete source is shown in Figure III.8 for the case where corrections are made outside the primary peak.

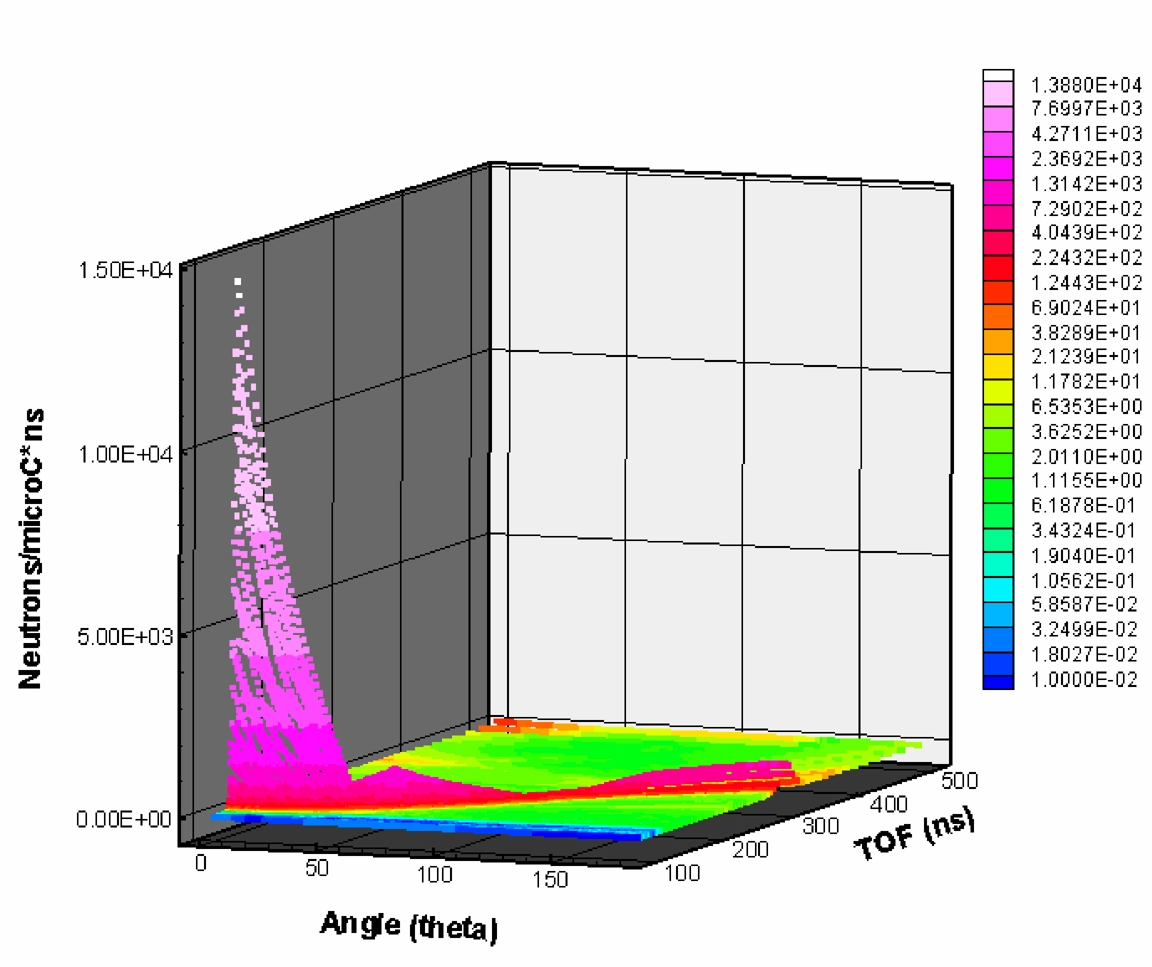

Figure III.8 Complete corrected 5 MeV D(d,n) source distribution.

It appears that the complete corrected source distribution provides the best estimate of a combination of the bounding spectra. A total of four source distributions are generated: The source distribution for the ^{15}N(p,n) reaction with a projectile energy of 5.1 MeV and the other three for the D(d,n) reaction with deuteron projectile energies of 3 MeV, 5 MeV, and 7 MeV.

Improvement in Calculation Efficiency

To improve the efficiency of the Monte Carlo simulations, we have considered two approaches: i) the use of variance reduction techniques; ii) the use of parallel processing.

Variance Reduction

We have investigated different approaches for reducing the variance or computation time of the Monte Carlo simulations. We have eliminated sections of the model after examining the impact of different regions on the measured particles of interest at the detector. Figure III.9 shows the whole model, and Figure III.10 shows the cut down model. In this model, the source region is simplified to include only the gas cell/target area, surrounded by the iron sphere, and the boundaries are moved to include only a portion of the concrete wall in the collimator region.

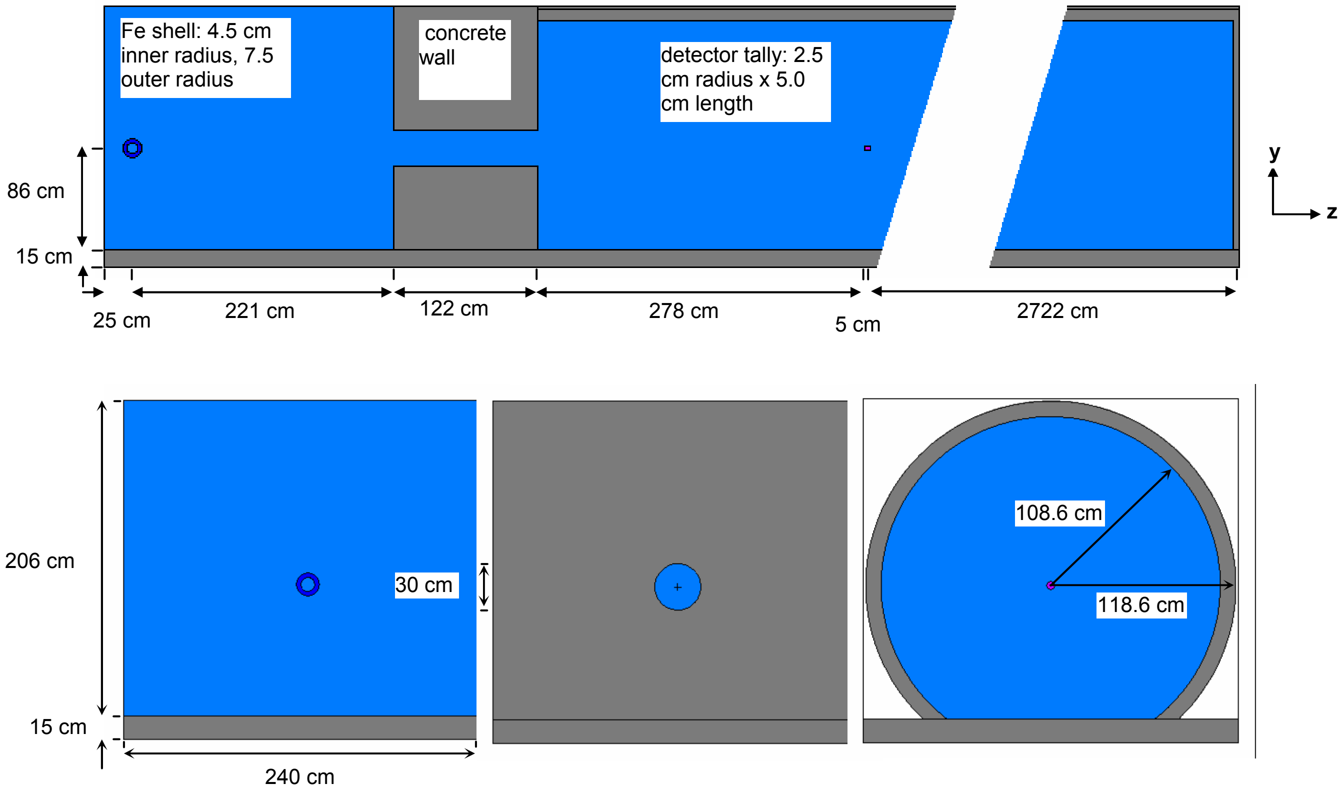

Figure III.9 Schematic of the large model. A cutaway view of the iron sphere center to the time of flight tunnel region is shown above. Cross sections through the iron sphere, the collimator and the time of flight tunnel are shown from right to left below.

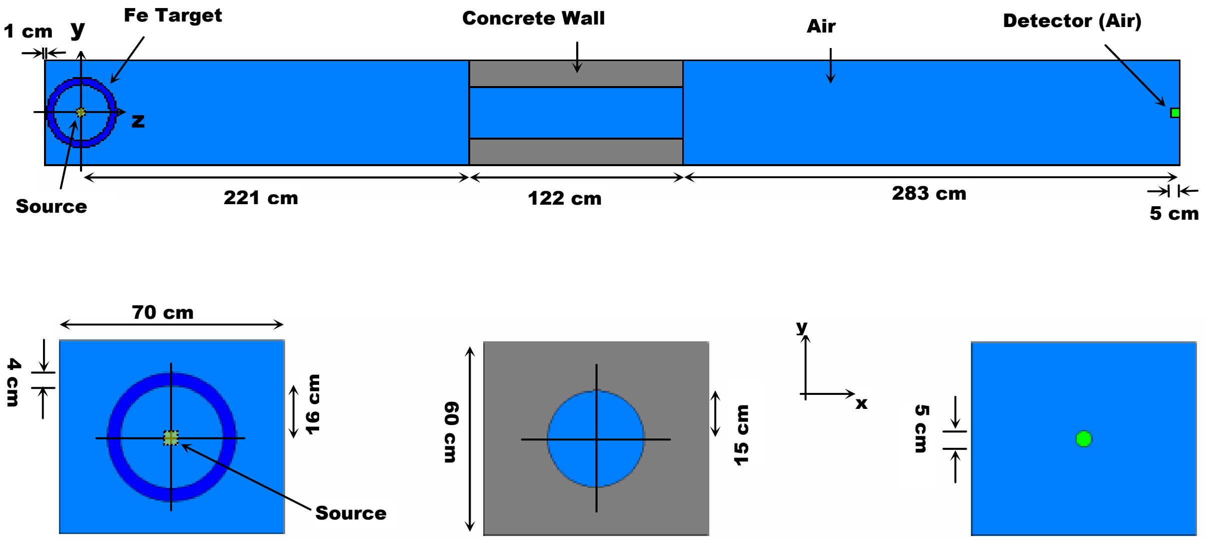

Figure III.10 Schematic of the cut down simplified model (The top diagram shows the iron sphere to the time of flight tunnel, and the bottom diagrams show x-y projections of the iron sphere, the collimator and an ideal detector, from right to left.)

In the final model setup, the detector is located at ~500 cm from the source, and a collimator is placed in the concrete wall as is shown in Figure III.11

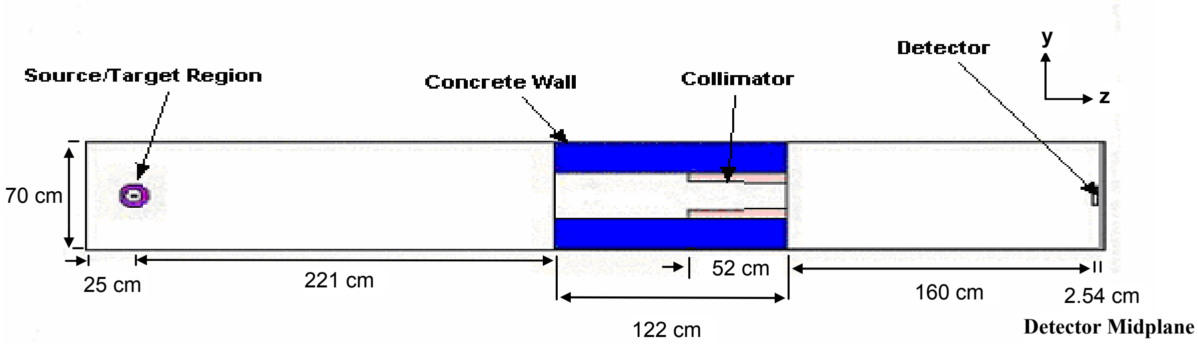

Figure III.11 Schematic of MCNP Model Utilized

Initially, the A^{3}MCNP (Automated Adjoint Accelerated MCNP) code[12] was utilized, but because of the presence of large void regions we did not observe noticeable reduction in computation time. This was caused by the significant ray-effect in the importance function calculated by the TORT code[13]. As will be discussed in Section III.2.2 on the deterministic methods, we have performed some feasibility studies using the PENTRAN code[14] with a recently developed biased quadrature set. These studies resulted in significant reduction in the ray-effects. This work, however, was not pursued because we were able to significantly reduce the computational time of the Monte Carlo simulations by using the simplified model and parallel processing.

Note that the default ‘implicit capture’ variance reduction technique in MCNP is used for all simulations performed in this study. This technique does not have significant impact on the code performance for the ToF simulations, because there is minimal absorption within the present experiment.

Parallel processing

Another approach to speed up the simulation is to process the Monte Carlo code in a parallel environment. For this, we are using the PVM (Parallel Virtual Machine) version 3.4.4[15] of MCNP4C2 on our two PC-clusters, PCPEN and PCA3MC which have 8 and 6 processors, respectively.

The use of the cut down model, variance reduction techniques, and parallel processing resulted in a significant reduction in the computational time of these simulations. For parallel computing alone, total simulation time can be reduced by at least a factor of 4.

III.2.2 Deterministic Sn method

As mentioned earlier, deterministic methods are important for performing sensitivity studies, where Monte Carlo methods become highly inefficient. One of the most widely used techniques for particle transport simulations with a fixed source (similar to the present project) is the discrete ordinates (Sn) method[16]. This method, however, suffers from ray-effects when the physical model contains large void regions.

PENTRAN, which is a 3-D parallel Sn code, has been shown to be able to diminish the ray-effects by using special numerical formulations[17]. The current problem, however, because of its large depth requires the use of special and biased quadrature sets. For this reason, we developed new methods for generation of angular quadrature sets[18]. Further, we devised new biasing approaches including ordinate splitting (OS)[19] and regional area refinement (RAR)[20]. Our studies and analyses demonstrated that the new quadrature techniques can yield flux distributions with minimal ray-effects. For example, using the model shown in Figure III.10, we have calculated the fast flux distribution due to a 14 MeV neutron source using the PENTRAN with different quadrature types and orders. Figure III.12 presents neutron flux distributions for the fastest group along the z-axis passing through the center of spherical shell up to a distance of 100 cm from the source. Besides the flux distributions obtained using different quadrature sets, Figure III.12 shows a reference solution obtained using the Monte Carlo method. These results demonstrate that an accurate solution is achieved using a Pn-Tn S30 with a 9x9 ordinate splitting refinement. Further, this angular refinement has resulted in a 3-D distribution, which is does not yield any ray-effect at the back of hole which penetrates through the wall which separates the source from the detector (see Figure III.10)

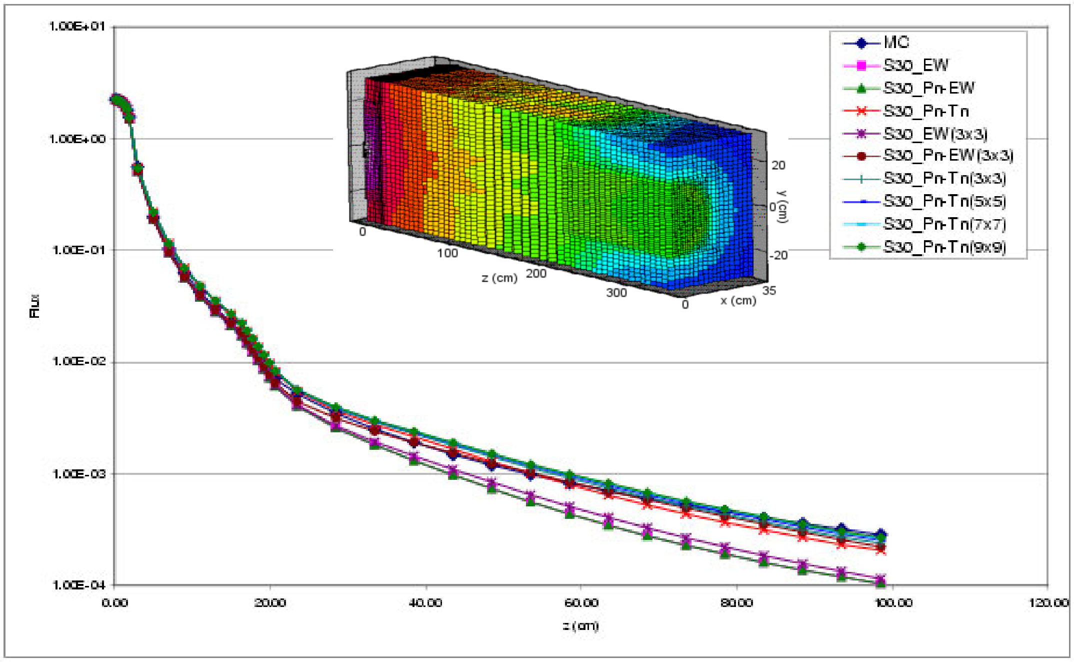

Figure III.12 Comparison of the neutron flux distributions obtained using different quadrature sets compared to a reference Monte Carlo solution (shown in dark blue).

Our studies demonstrate the possibility of using the Sn method which can be instrumental if one is interested in performing detailed simulations such as estimating the background radiation or performing detailed sensitivity analyses for examining cross sections.

III.3 Optimization of the experimental setup

To determine the "optimum" neutron source energy versus sphere thickness, a simplified MCNP model of the experimental setup was utilized as is shown in Figure III.11. Using the simplified model and the new tallying option, a study of several neutron source energies in the range from 2.5 MeV to 8.0 MeV, and several iron-shell thicknesses from 1.0 cm to 20.0 cm was performed. The fraction of neutrons that undergo at least one inelastic scattering event within the shell then subsequently traverse the detector region for the different combinations of neutron source energy and sphere thickness was analyzed. Figure III.13 shows that for essentially all of the source energies tested, there is a range of sphere thickness, from ~4 cm to ~9 cm, where the fraction of inelastically scattered neutrons is maximal.

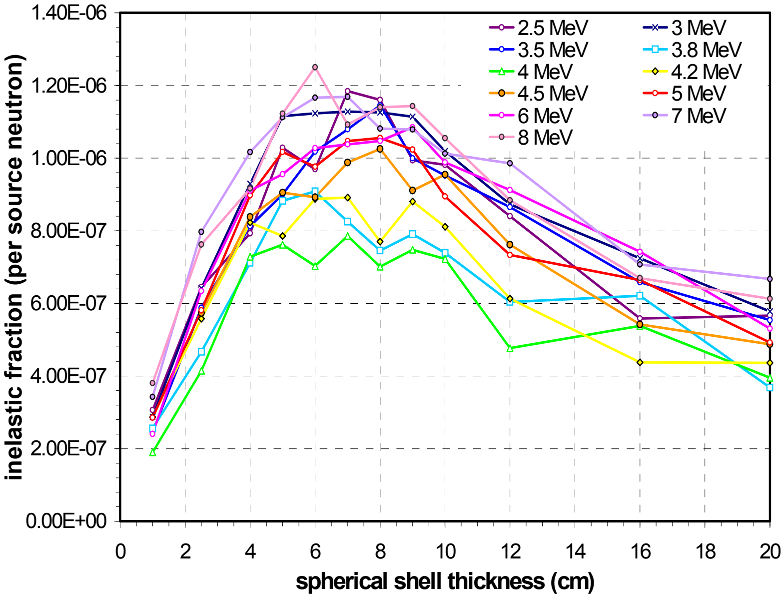

Figure III.13 Estimation of the number of inelastically scattered neutrons which are detected at the detector for different source energies and sphere thicknesses.

The results also indicate that for source energies below approximately 4 MeV there is a significant decrease in this fraction, a feature that can be attributed to the lower inelastic scattering cross section and the fact that below ~4 MeV there is a significant decrease in the forward and backward scattering, relative to scattering about 90 degrees. The backward scattering results in higher neutron leakage from the target, thereby decreasing the number of inelastic neutrons that propagate to the detector.

III. 4 ToF Simulation

In this section, we present the results of the Monte Carlo simulations for the ToF experiments. Comparisons of experimental data and calculation predictions have demonstrated some differences, which can be attributed to errors in the cross sections. We have devised a methodology to adjust the cross sections, and examine the effect of the adjusted cross sections in continuous energy and multigroup forms. For the multigroup form, we have examined the results using a pressure vessel cavity dosimeter problem. The ENDF/B-VI cross sections for impurities and isotopic contributions, where available were used in the analyses.

Section III.4.1 discusses the results of the $^{15}N(p,n)$ simulations and experiments with and without the iron sphere. Section III.4.2 discusses the results of the D(d,n) simulations and experiments for deuteron energies of 3 MeV, 5 MeV, and 7 MeV, with and without the iron sphere. Section III.4.3 presents a methodology for adjusting cross sections. Section III.4.4 examines the effect of the adjusted cross sections in continuous energy and multigroup forms.

III.4.1 Comparison of the $^{15}N(p,n)$ calculations and experiments.

III.4.1.1 Without Sphere

Figs. III.14-III.21 compare the $^{15}N(p,n)$ normalized Monte Carlo predictions to the experimental data for beam angles at 0, 15, 45, 60, 90, 100, 120, and 135 degrees without the spherical shell.

We have normalized the Monte Carlo simulation results by the total experimental counts within the range of data shown in the figures. It is important to note that the one sigma statistical relative error associated with the Monte Carlo simulations is below 10% for all the points shown in the figures.

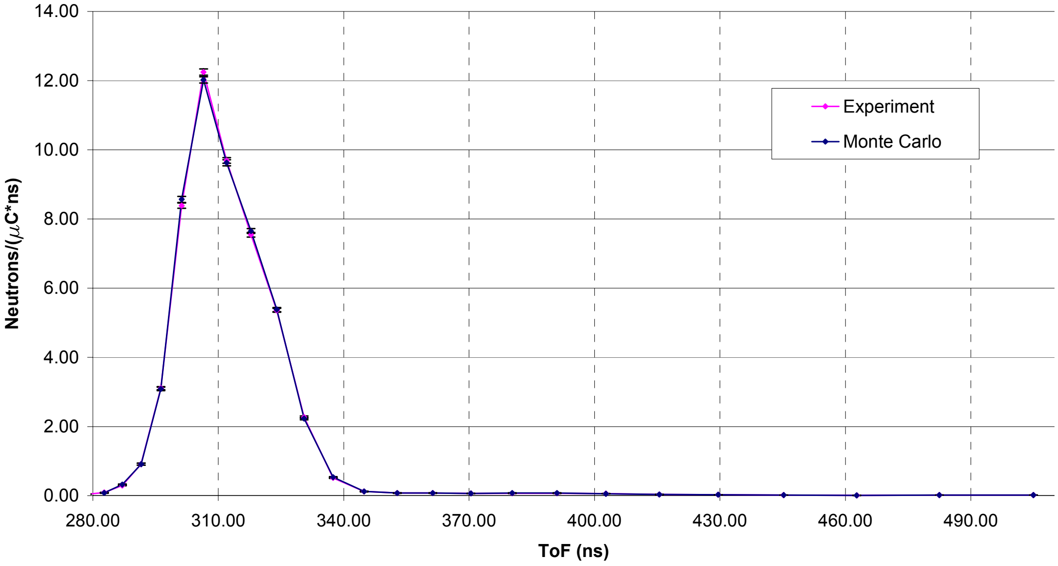

Figure III.14 Comparison of ^{15}N(p,n) Monte Carlo calculations and experimental data for the 0 degree angle.

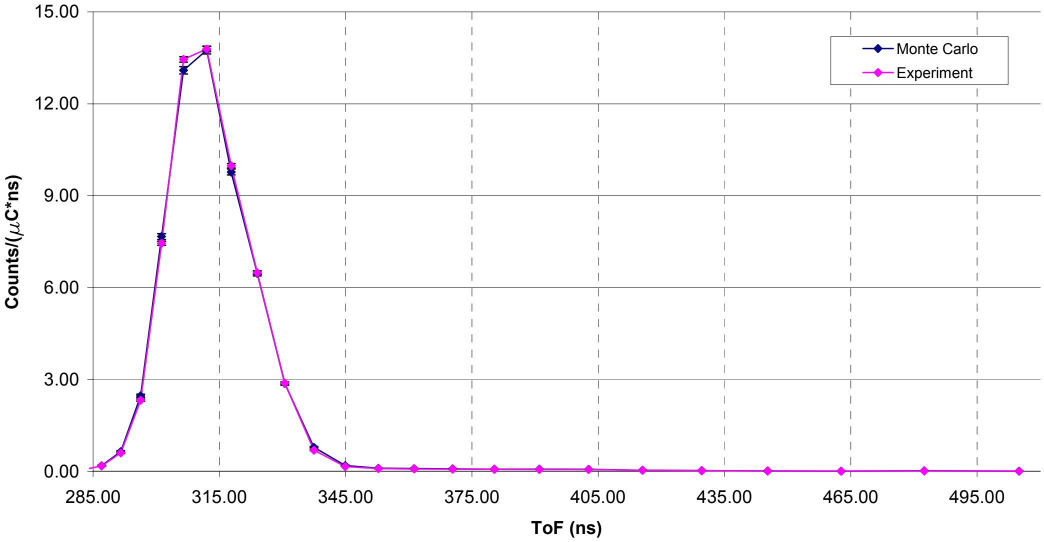

Figure III.15 Comparison of ^{15}N(p,n) Monte Carlo calculations and experimental data for the 15 degree angle.

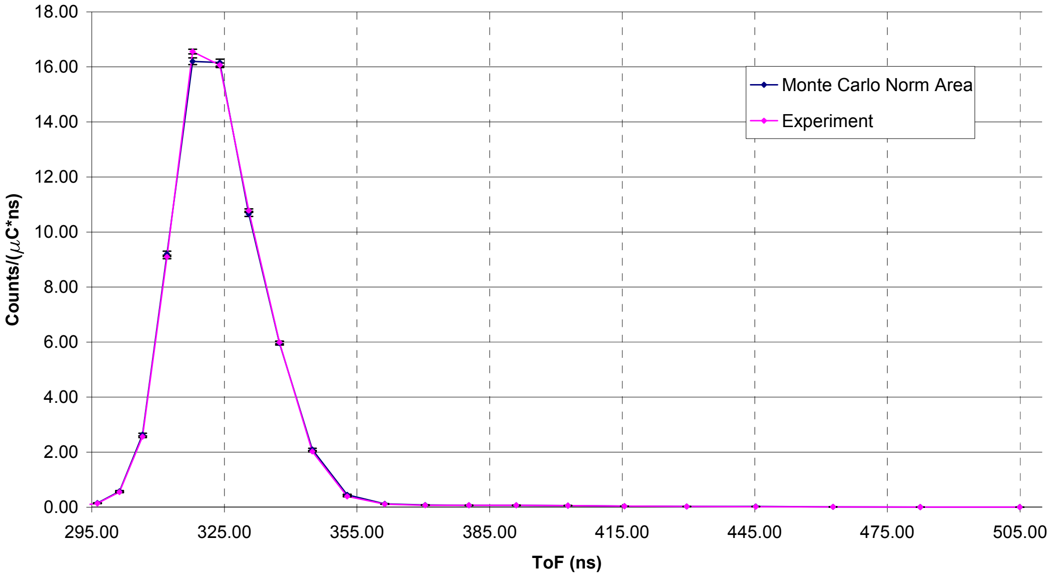

Figure III.16 Comparison of ^{15}N(p,n) Monte Carlo calculations and experimental data for the 45 degree angle.

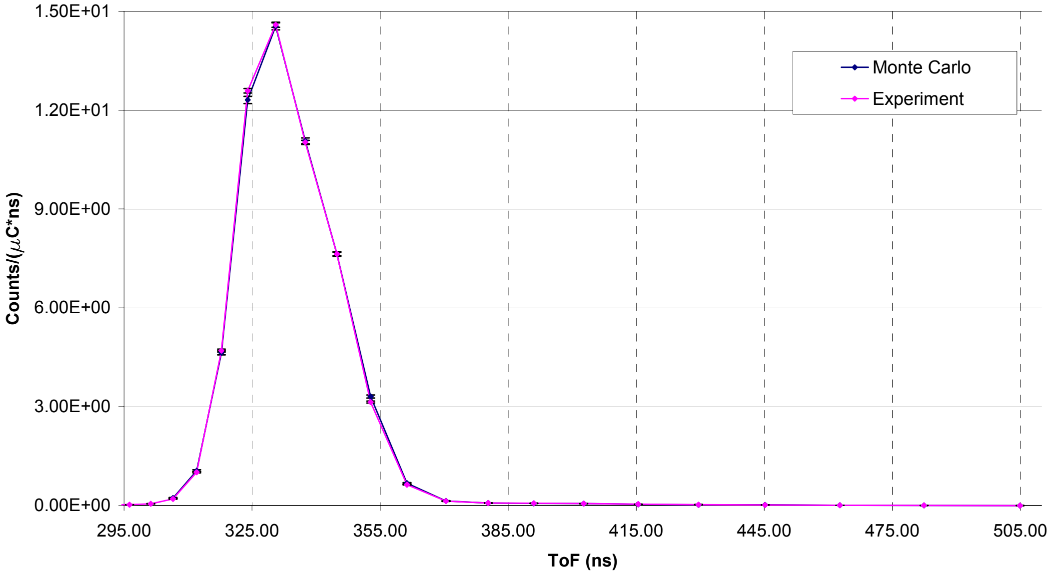

Figure III.17 Comparison of ^{15}N(p,n) Monte Carlo calculations and experimental data for the 60 degree angle.

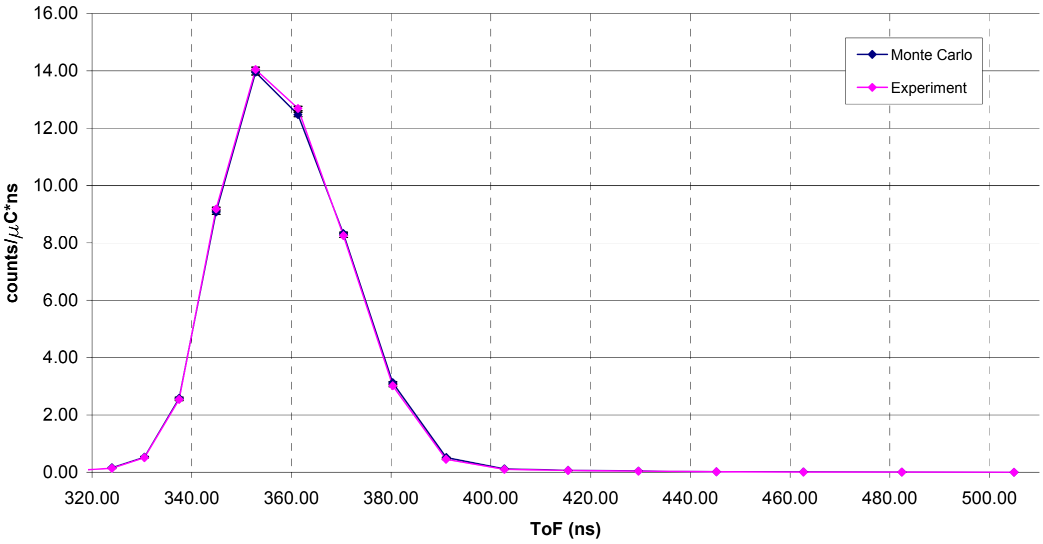

Figure III.18 Comparison of ^{15}N(p,n) Monte Carlo calculations and experimental data for the 90 angle.

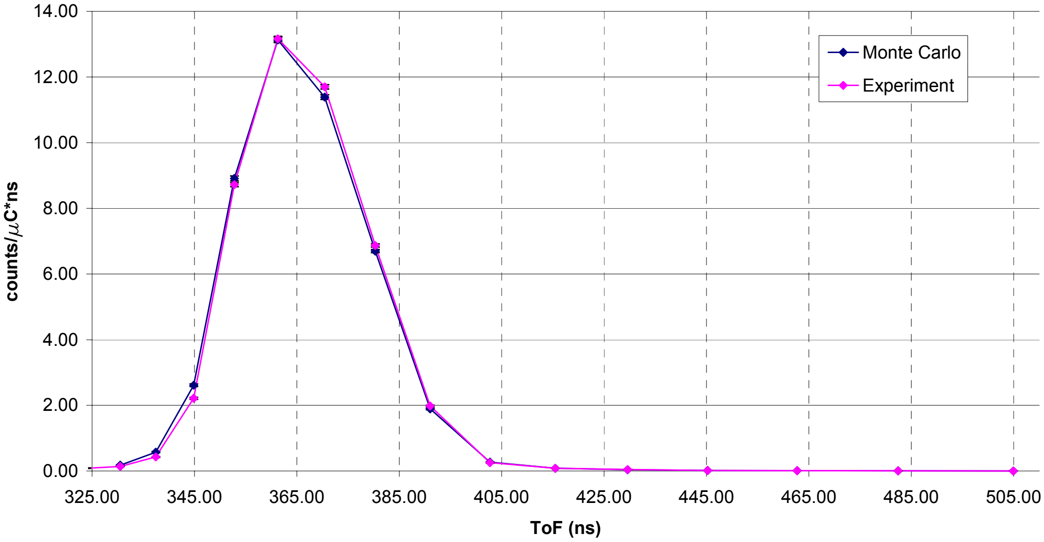

Figure III.19 Comparison of ^{15}N(p,n) Monte Carlo calculations and experimental data for the 100 degree angle.

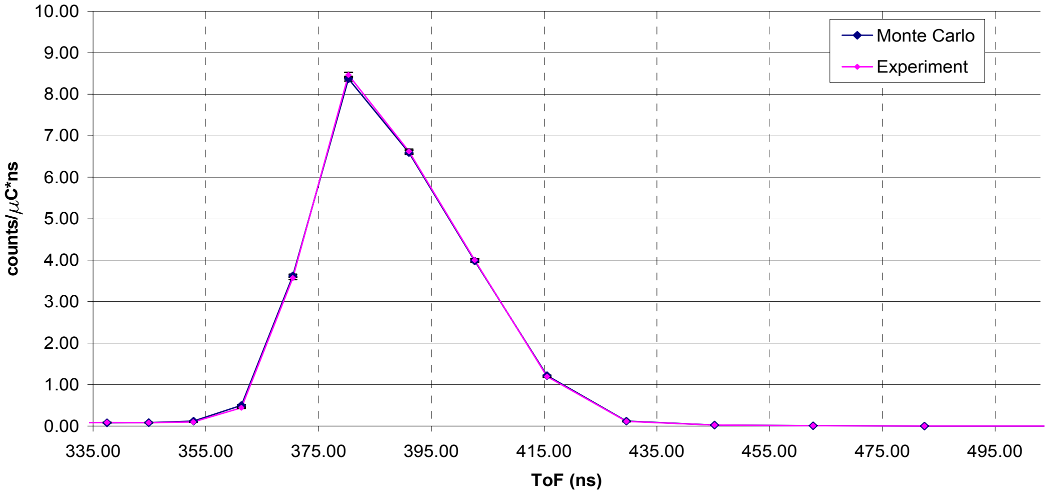

Figure III.20 Comparison of ^{15}N(p,n) Monte Carlo calculations and experimental data for the 120 degree angle.

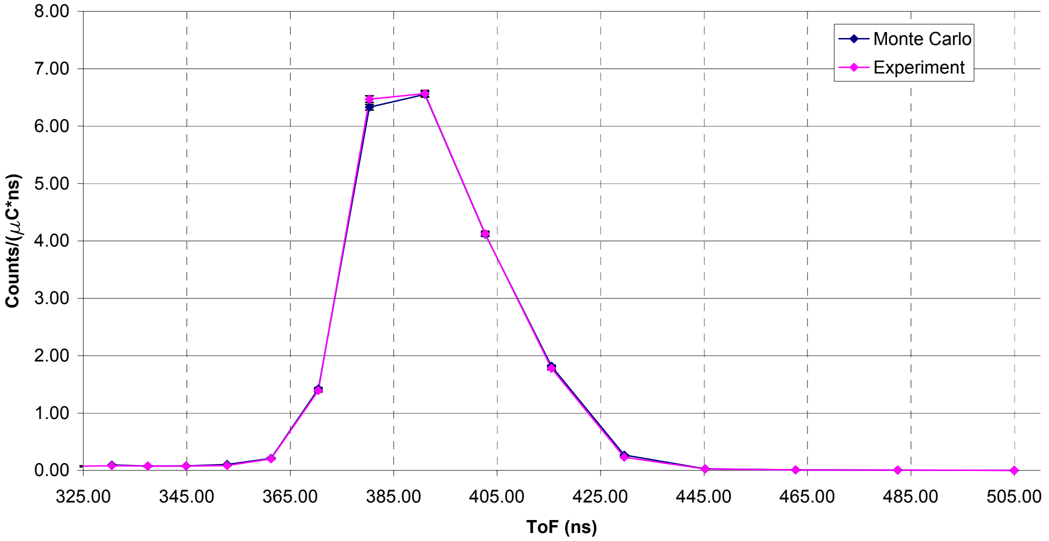

Figure III.21 Comparison of ^{15}N(p,n) Monte Carlo calculations and experimental data for the 135 degree angle.

The observed maximum differences between the calculation and experimental data for 0, 15, 45, 60, 90, 100, 120, and 135 angle cases are ~2%, 6%, 3%, 5%, 3.4%, 18%, 1.6%, and 2.1%, respectively. The statistical errors associated with different source angles are presented in Table III.1.

Table III.1One sigma Statistical Error for ^{15}N(p,n) Sphere Off Monte Carlo Simulation

Angle (Degrees)	Max Stat. Error (%)	Min Stat Error (%)	Peak Stat Error (%)
0	9.2	0.47	0.78
15	8.6	0.76	0.92
45	8.9	0.74	0.74
60	6.8	0.74	0.88
90	7.9	0.65	0.69
100	6.7	0.62	0.62
120	9.3	0.67	0.67
135	9.6	0.70	0.77

We observe that the statistical error at the peak region is less that 1% for all cases. Hence, the remaining difference can be attributed to the error in source modeling. For example, for the zero-degree case, the remaining difference of ~1.4% can be attributed to the error in the source used for Monte Carlo simulation. Hence, when comparing the Monte Carlo and experimental predictions, we should account for this error, i.e., subtract the error from the observed difference.

III.4.1.2. Small Sphere

Figs. III.22-III.24 compare the ^{15}N(p,n) normalized Monte Carlo predictions to the experimental data for different beam angles at 0, 45, and 90 degree angles for the small sphere case.

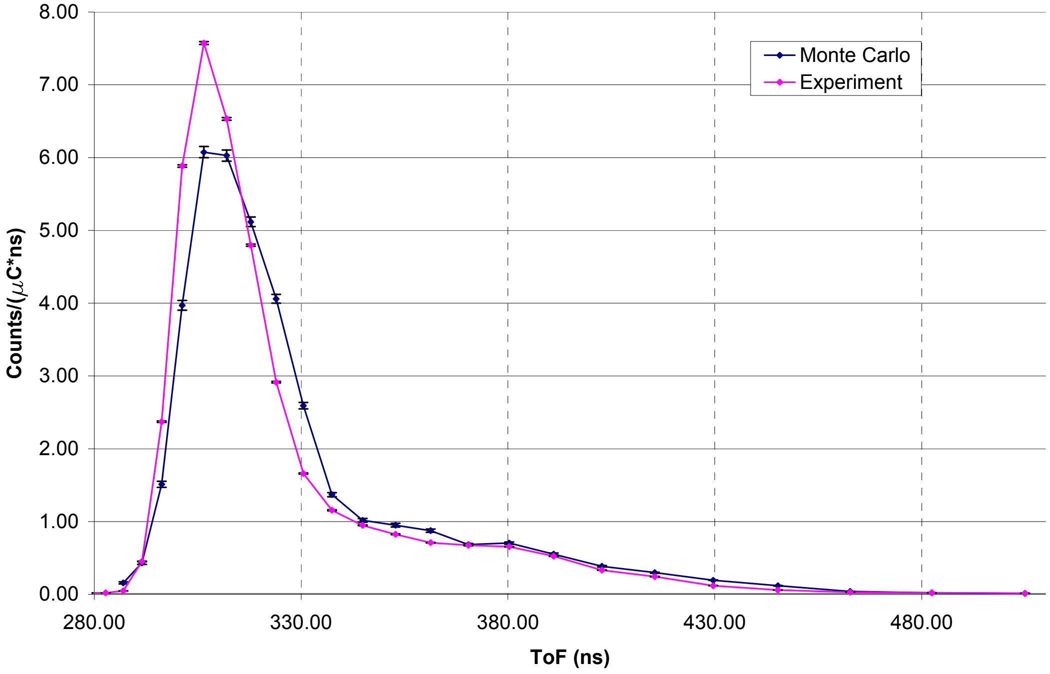

Figure III.22 Comparison of ^{15}N(p,n) Monte Carlo calculations and experimental data for the 0 degree angle. (Small Sphere On)

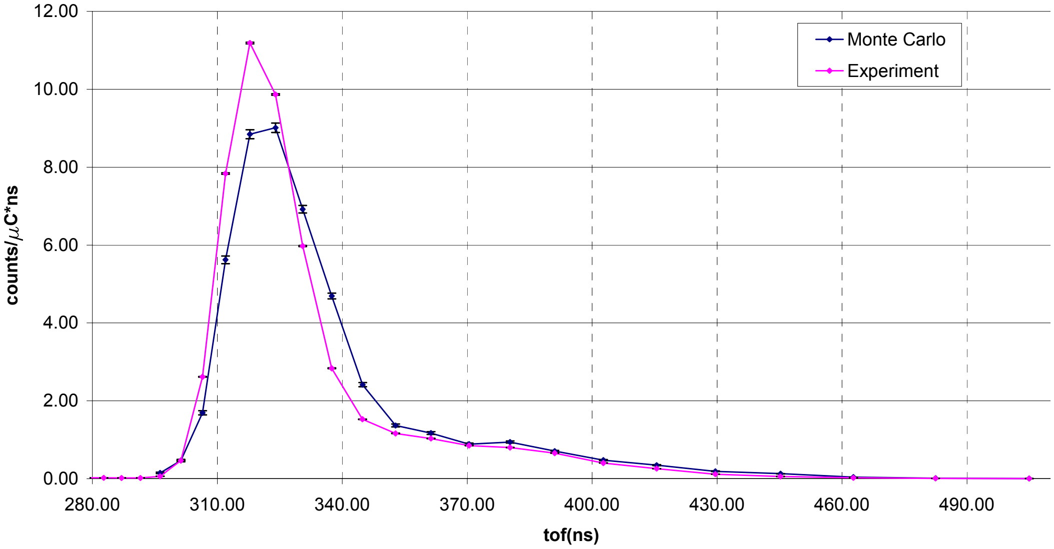

Figure III.23 Comparison of ^{15}N(p,n) Monte Carlo calculations and experimental data for the 45 degree angle. (Small Sphere On)

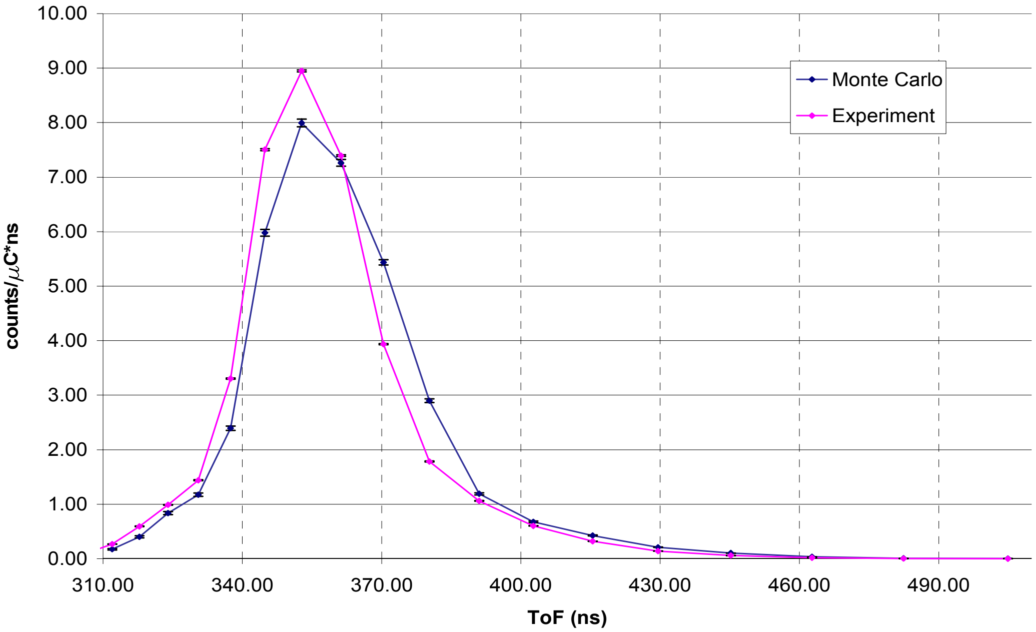

Figure III.24 Comparison of ^{15}N(p,n) Monte Carlo calculations and experimental data for the 90 degree angle. (Small Sphere On)

The maximum differences between the calculation and experimental data at the peak are ~20%, 21%, and 11% for 0, 45, 90 degree angles, respectively. The observed maximum differences over the whole spectrum are ~232%, ~205% and ~110% for the three angles. Table III.2 gives the statistical error associated with the different angles.

Table III.2 One sigma statistical error for ^{15}N(p,n) small sphere on Monte Carlo simulation

Angle (Degrees)	Max Stat. Error (%)	Min Stat Error (%)	Peak Stat Error (%)
0	8.8	0.86	1.3
45	9.2	1.0	1.
90	7.2	0.85	0.90%

It is apparent that observed differences in Figs. III.22 – III.24 are significantly larger than the statistical errors. Even in the peak region of the zero-degree case, after removing the ~1.5% statistical error, and 1-5% error caused by the difference in the source, we observe 13.5-17.5% difference which can be attributed to the expected error in the ENDF/B-VI cross section library..

III.4.1.3. Large Sphere

Figs. III.25-III.27 compare the $^{15}N(p,n)$ normalized calculation predictions to the experimental data for different beam angles at 0, 45, 90 degrees for the large sphere-on case.

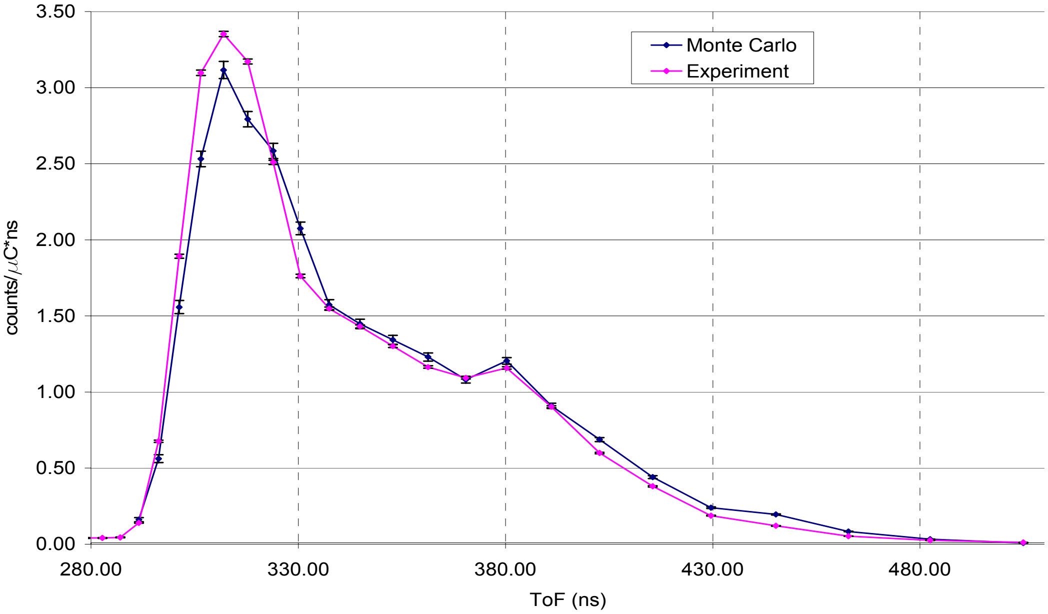

Figure III.25 Comparison of $^{15}N(p,n)$ Monte Carlo calculations and experimental data for the 0 degree angle. (Large Sphere On)

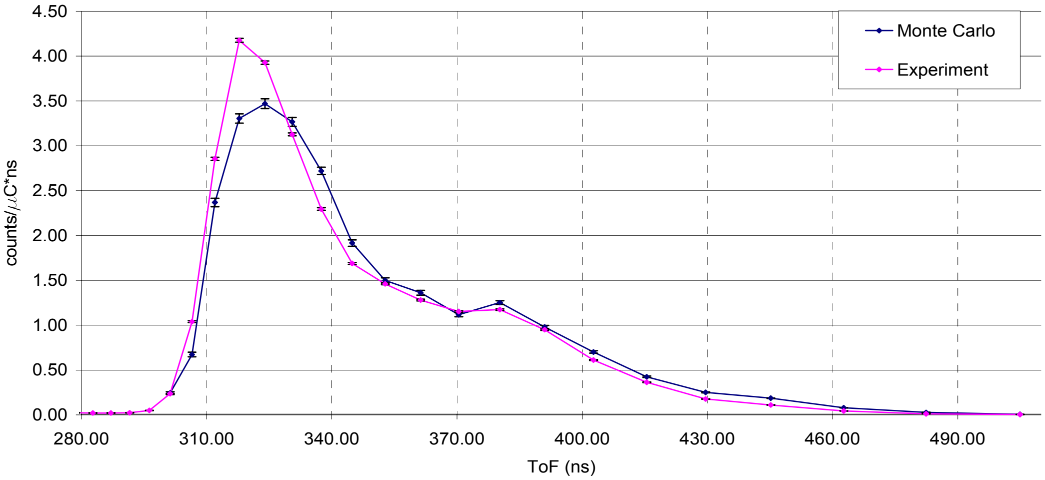

Figure III.26 Comparison of ^{15}N(p,n) Monte Carlo calculations and experimental data for the 45 degree angle. (Large Sphere On)

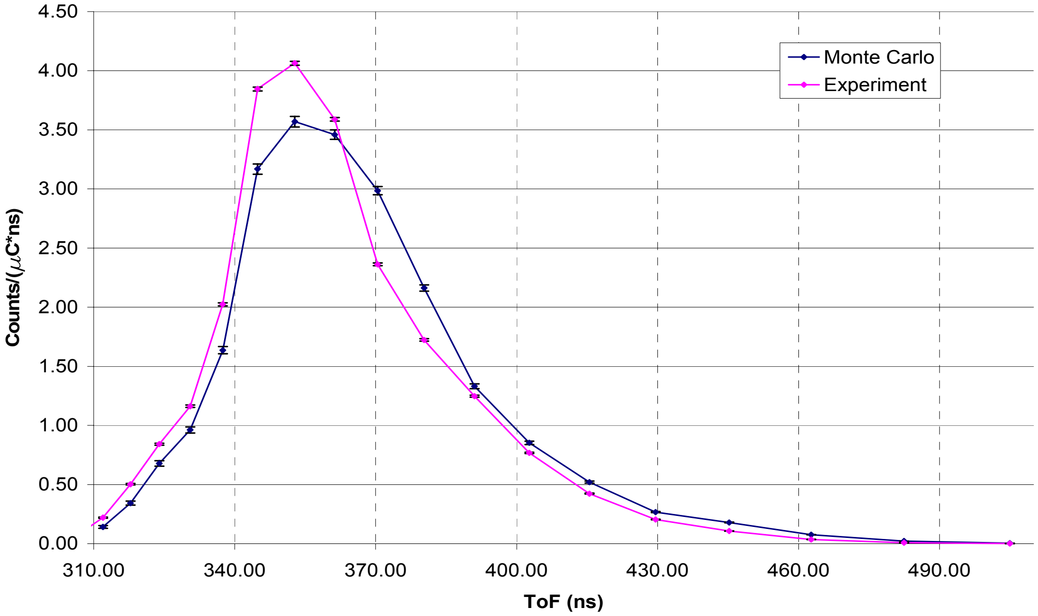

Figure III.27 Comparison of ^{15}N(p,n) Monte Carlo calculations and experimental data for the 90 degree angle. (Large Sphere On)

Table III.3 shows the statistical error associated with the 0, 45 and 90 degree Monte Carlo simulations.

Table III.3 One Sigma Statistical Error for $^{15}N(p,n)$ Small Sphere On Monte Carlo Simulation

Angle (Degrees)	Max Stat. Error (%)	Min Stat Error (%)	Peak Stat Error (%)
0	8.8	1.8	1.8
45	6.6	1.5	1.6
90	7.9	1.2	1.2

At the peak, the differences between the calculation and experimental data for 0, 45, and 90 degree angles are ~7%, 21%, and 12% respectively. The maximum differences over the whole spectrum for the three angles are 62%, 125%, and 148% respectively. Again, the observed differences are significantly larger than the sum of statistical error plus the expected error in the source modeling. Even at the peak of the zero-degree case, 3-4% of error may be attributed to the error in the iron cross sections.

Section III.4.2 Comparison of the D(d,n) calculations and experiments.

Section III.4.2.1 Without Sphere

In this section, we compare the Monte Carlo and experiment data for the D(d,n) interaction for projectile energies of 3 MeV, 5 MeV, and 7 MeV without the presence of the spherical shell.

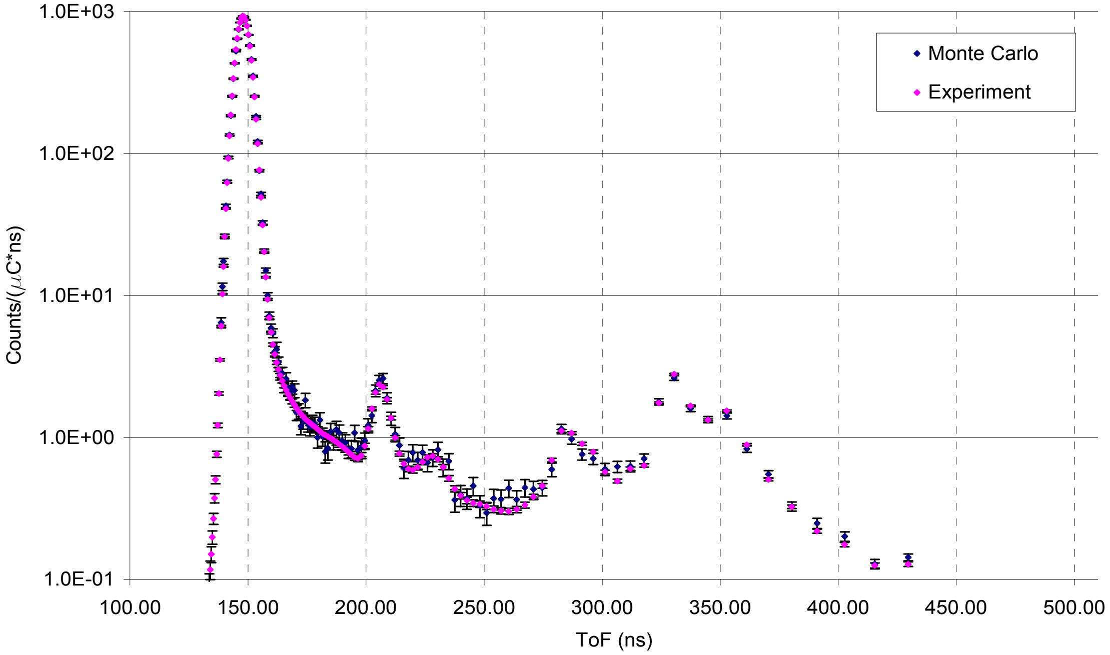

Figure III.28 Comparison of 3 MeV D(d,n) Monte Carlo calculations and experimental data for the 0 degree angle.

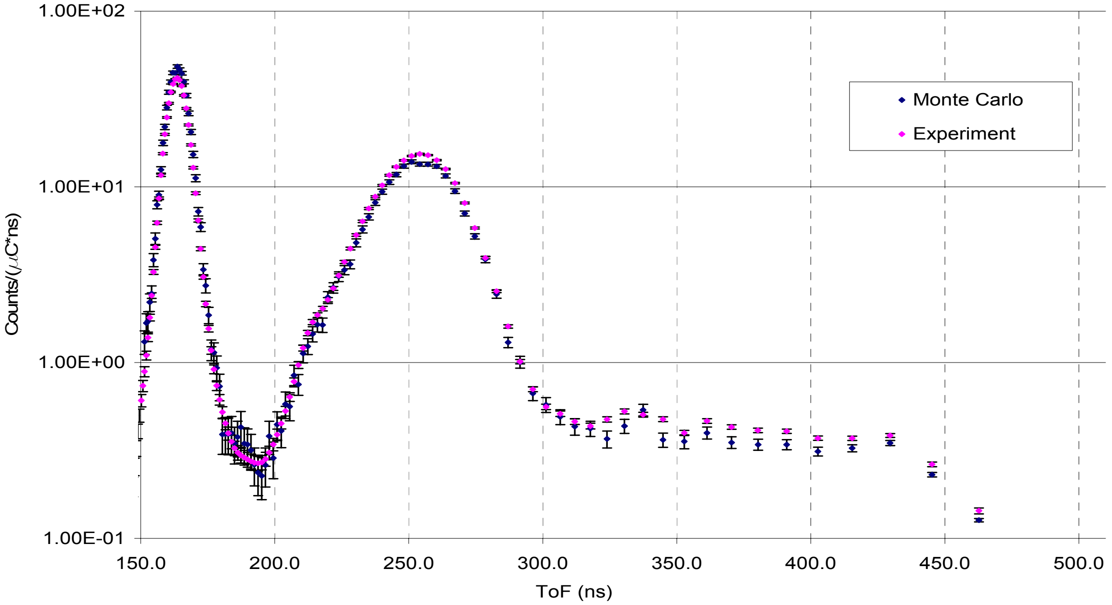

Figure III.29 Comparison of 3 MeV D(d,n) Monte Carlo calculations and experimental data for the 45 degree angle.

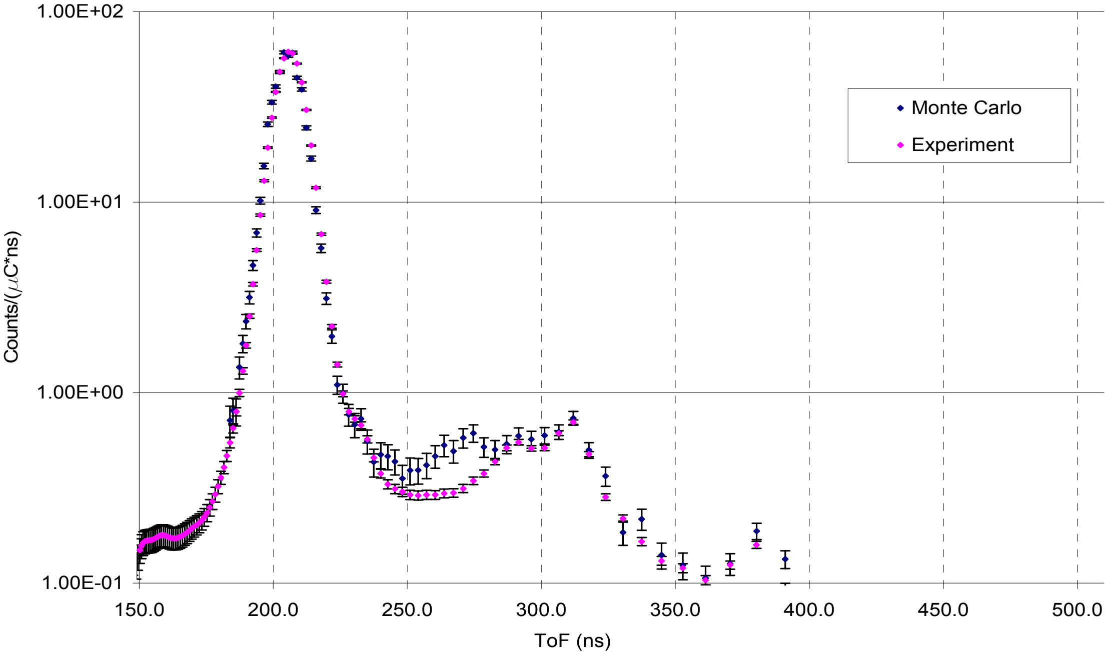

Figure III.30 Comparison of 3 MeV Monte Carlo calculations and experimental data for 90 degree angle.

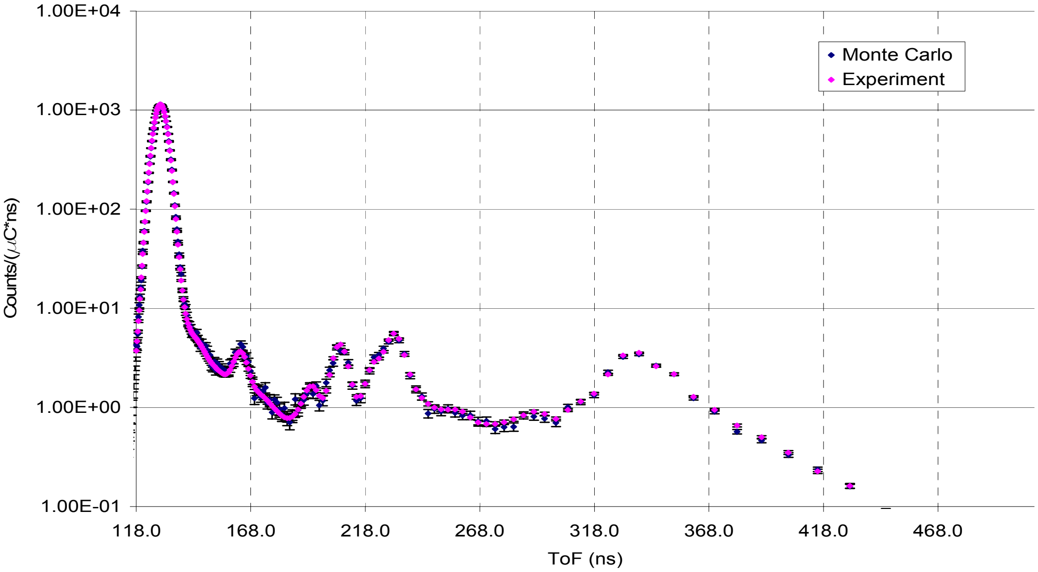

Figure III.31 Comparison of 5 MeV D(d,n) Monte Carlo calculations and experimental data for the 0 degree angle.

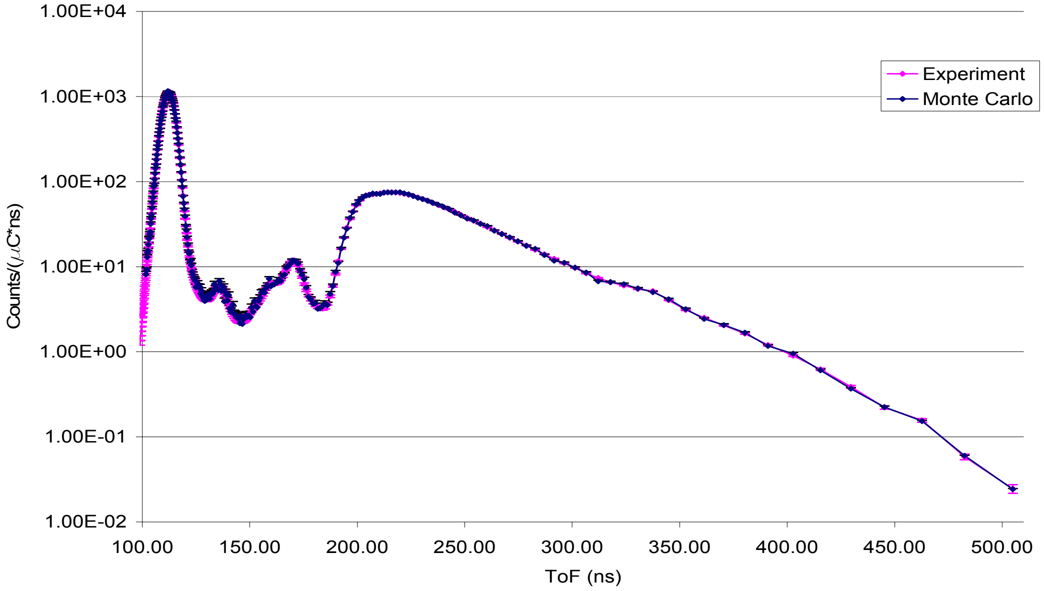

Figure III.32 Comparison of 7 MeV D(d,n) Monte Carlo calculations and experimental data for the 0 degree angle.

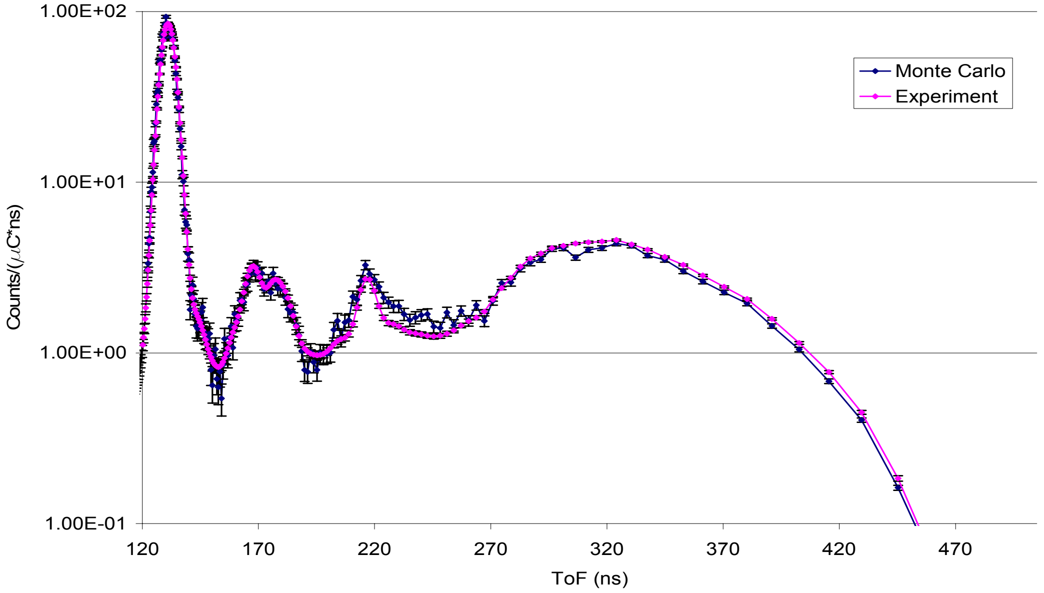

Figure III.33 Comparison of 7 MeV D(d,n) Monte Carlo calculations and experimental data for the 45 degree angle.

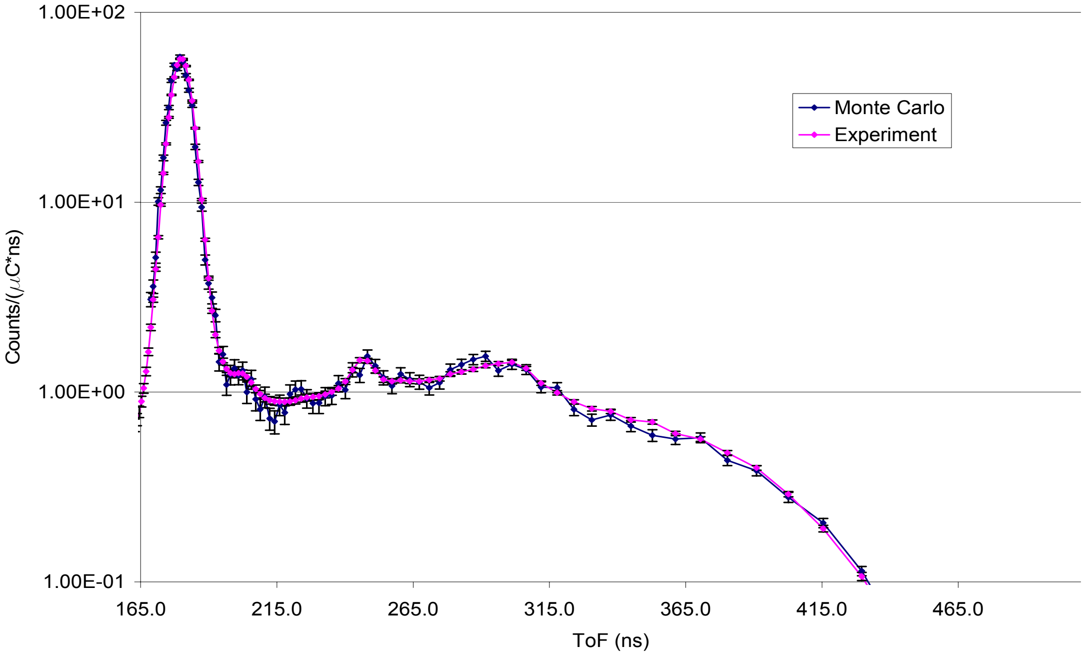

Figure III.34 Comparison of 7 MeV D(d,n) Monte Carlo calculations and experimental data for the 90 degree angle.

Table III.4 presents the statistical error associated with the Monte Carlo calculation results shown in Figs. III.29-III.34.

Table III.4 One sigma Statistical Error for D(d,n) Sphere Off Monte Carlo Simulations

Beam Energy	Angle (Degrees)	Max Stat. Error (%)	Min Stat Error (%)	Peak Stat Error (%)
3 MeV	0	18	0.55	0.56
	45	27	0.96	2.3
	90	24	1.2	2.1
5 MeV	0	16	0.50	0.52
7 MeV	0	13	0.70	0.83
	45	21	1.8	1.9
	90	14	1.7	1.9

The differences between the calculation and experimental data for different cases at the peaks and over the whole spectra are given in Table III.5

Table III.5 Experiment and Calculation differences for D(d,n) Sphere Off Simulations

Beam Energy	Angle (Degrees)	Peak (%)	Max. Relative Difference (%)
3 MeV	0	1.5	48
	45	16	52
	90	4.6	85
5 MeV	0	0.22	41
7 MeV	0	1.0	30
	45	14	45
	90	2.6	54

Compared to the ^{15}N(p,n) experiments, the differences between the calculation and experimental data are similar magnitude for the peaks, but are noticeably larger over the rest of the spectrum. The larger differences may be related to the larger inaccuracies in the source modeling and errors in processing the D(d,n) experiments.

Section III.4.2.2 With Sphere

In this section, we compare the calculation and experimental data for the zero-degree angle D(d,n) interactions with projectile energies of 3 MeV, 5 MeV, and 7 MeV. For angles greater that zero-degree, a more complex source modeling is needed, hence, the results are not reported here.

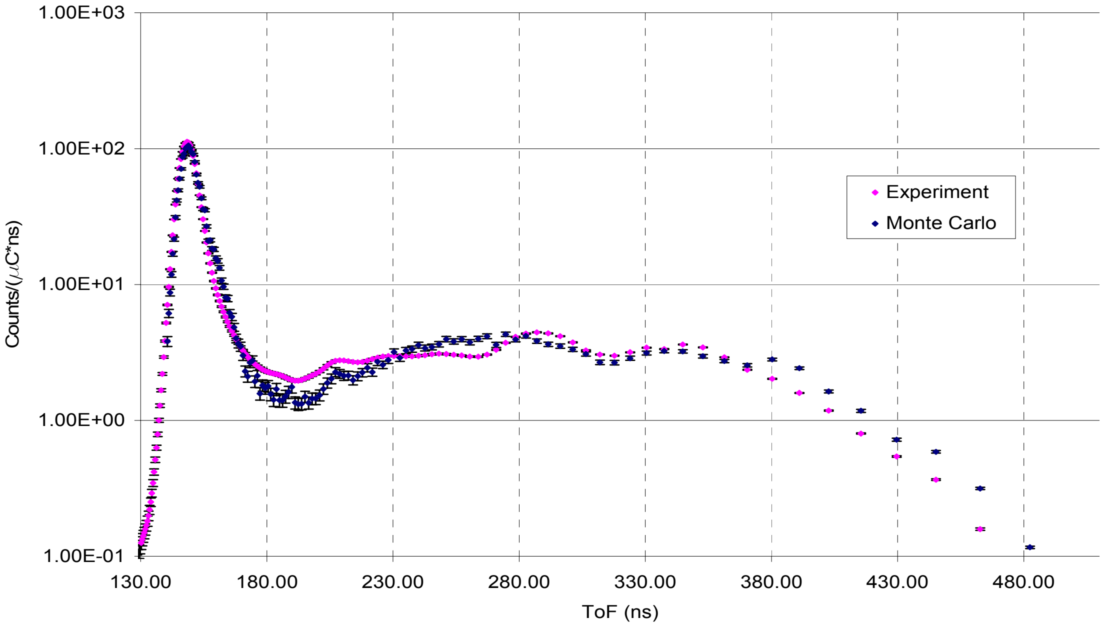

Figure III.35 Comparison of 3MeV D(d,n) Monte Carlo calculations and experimental data for the 0 degree angle. (Large Sphere On)

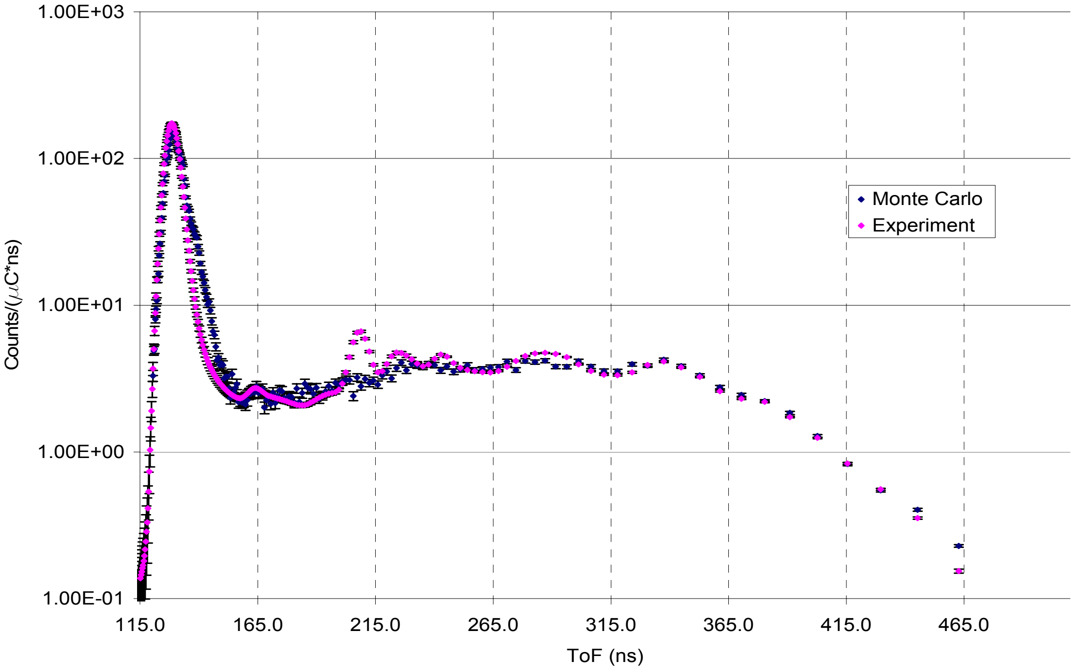

Figure III.36 Comparison of 5MeV D(d,n) Monte Carlo calculations and experimental data for the 0 degree angle. (Large Sphere On)

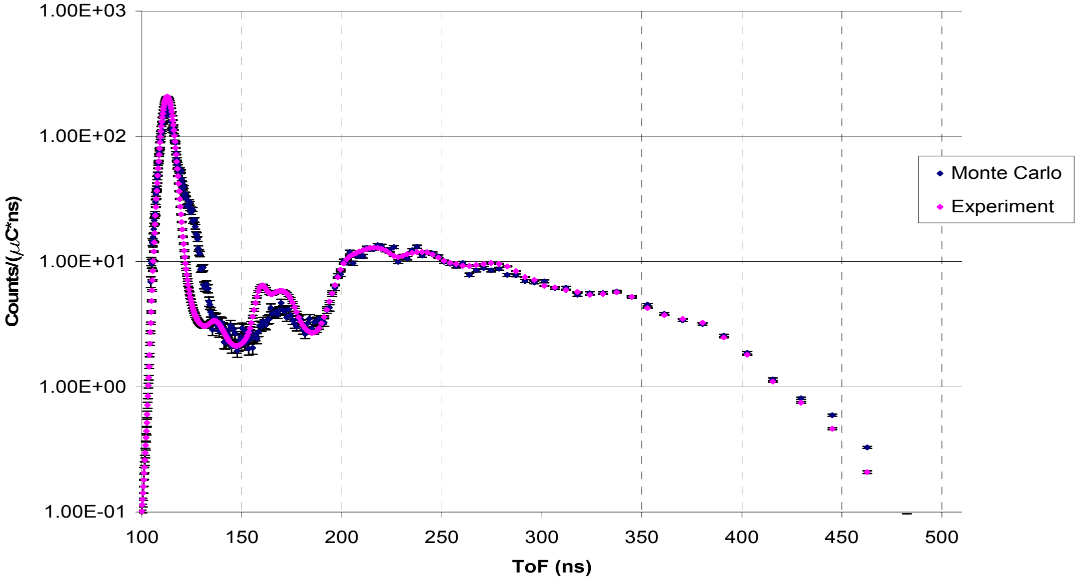

Figure III.37 Comparison of the 7MeV D(d,n) Monte Carlo calculations and experimental data for the 0 degree angle. (Large Sphere On)

Table III.6 presents the statistical error associated with the Monte Carlo results shown in above figures.

Table III.6 One Sigma Statistical Error for zero-degree D(d,n) Large Sphere On Monte Carlo Simulation

Beam Energy	Max Stat. Error (%)	Min Stat Error (%)	Peak Stat Error (%)
3 MeV	11	1.5	1.6
5MeV	9.3	1.2	1.3
7 MeV	12	1.7	2.0

The differences between the experimental and calculation data at the peaks are ~8%, ~13%, ~18% for projectile energies of 3 MeV, 5 MeV, and 7 MeV, respectively. The maximum differences over the whole spectra of the three projectile energies are ~99%, 235%, and 495%, respectively. These results indicate that the differences of experimental and calculation predictions increase noticeably with the increasing projectile energies. Since the combined systematic experimental error (~5%) and statistical error associated with calculations (Table III.6) is significantly less than the observed differences between the calculation and experimental data, we believe that the remaining difference may be attributed to the inaccuracy in the inelastic scattering cross sections.

III.4.3 Cross Section Evaluation and Adjustment Methodology

This section discusses the methodology used to adjust inelastic cross sections. Since the error in the experimental data are not equal throughout the ToF spectrum, and these errors have the lowest values at the peak of the spectrum, therefore, we have decided to use only the peak values for the purpose of cross section adjustment.

Before discussing the methodology for extraction and adjustment of inelastic cross sections, it is beneficial to evaluate the total cross sections at the peak location and compare them to the existing ENDF/B-VI data[21]. To estimate the total cross section, we utilize the following formulation

$$uc = c_0 e^{-\Sigma_t t} \tag{III.2}$$

where *uc* is the count for uncollided neutrons and c_0 is the count for source particles within the energy bin and angular bin of interest. The uncollided particle count is determined by removing the elastically scattered particles from the total count at the detector. Using the new tally option (Section III.2.1.1), we have estimated the fraction of neutrons that are elastically scattered and reduced the counts by that fraction. Table III.7 compares the ENDF/B-VI library's total cross sections to those obtained using Eq. III.2 based on the D(d,n) interaction with projectile energies of 3 MeV and 5 MeV.

Table III.7Comparison of estimated and ENDF/B-VI total cross sections using the D(d,n) experiments*

Interaction	**Energy Bin (MeV)**	**Counts (arbitrary units)**		**Σ_t (cm^{-1}, ENDF/B-VI)**	**Σ_t** (cm^{-1}, Estimated)**	**Relative Differences (%) of total Cross Section*** **
		c_o**	**uc** (fraction of uncollided neutrons)**			
3 MeV D(d,n) (Large Sphere)	6.1534 to 6.2035	549.88	49.07 (.754)	0.3033	0.3023	-0.3 %
5 MeV D(d,n) (Large Sphere)	8.1550 to 8.2050	444.15	46.44 (.689)	0.2839	0.2825	-0.5 %

*Experiment error <1.0%

** See Equation III.2

*** $\left(\frac{\sigma(estimated)_{nonelastic} - \sigma(ENDF/B-VI)_{nonelastic}}{\sigma(ENDF/B-VI)_{nonelastic}} \right)$

It is important to note that the values of the estimated and ENDF/B-VI total cross sections agree within 1%, which somewhat verifies the experimental data and the analytical technique being used.

To achieve a closer agreement between the calculation and experimental data for the sphere on cases, we have adjusted the inelastic cross sections at a few energy bins corresponding to the peak of the spectra of D(d,n) measurements. The peak energy bins were considered because there is more confidence in both experiment and calculation at these energy bins.

Table III.8 lists the energy bin widths along with changes made to the cross sections for the three D(d,n) measurements at zero-degree angle.

Table III.8 Cross Section adjustments and their associated energy bin

Interaction	**Energy Bin (MeV)**	**(%) change in inelastic Cross Section**
3 MeV D(d,n)	6.1534 - 6.2035	-21
5 MeV D(d,n)	8.1550 - 8.2050	-29
7 MeV D(d,n)	10.7561 - 10.8061	-35

Note that we have considered a larger percent change for the increasing projectile energies, because of the observed increasing differences between the calculation and experiment in the peak regions.

To change the inelastic cross sections in the ENDF/B-VI library, we developed an algorithm called XSMOD in F90. XSMOD is a menu driven software, and is capable of modifying cross sections for any interaction type (MT number) given in ENDF/B-VI.

III.4.4 Generation of the adjusted cross sections

The inelastic and elastic cross sections were modified such that the total cross sections remain constant. For this testing, we have changed the inelastic cross sections by relative differences obtained for the D(d,n) reaction at 3 MeV, 5 MeV, and 7 MeV with the large sphere as given in Table III.8. Figure III.38 shows nonelastic, inelastic, elastic, and total cross sections before and after adjustment

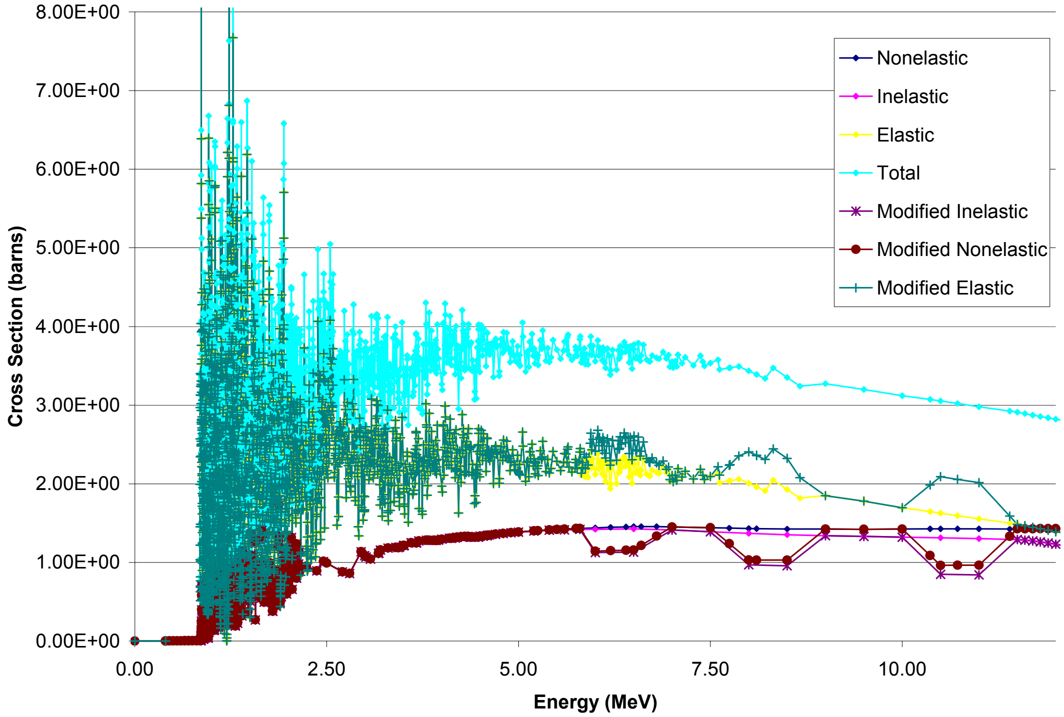

Figure III.38 Fe-56 ENDF/B-VI and adjusted nonelastic, inelastic, elastic, and total cross section.

Since there are no data points in the region of change in the ENDF library, XSMOD modifies the nearest points above and below of the energy bin of interest, and a new cross-section distribution is obtained via a linear interpolation. This procedure, however, broadens the affected region of cross section distribution as seen in Figure III.38.

III.4.5 The effect of modified cross sections

To examine the effect of the new adjusted cross sections, we have generated both continuous energy and multigroup cross sections.

III.4.5.1 Continuous energy Monte Carlo simulation

The adjusted Fe-56 cross sections are processed through the NJOY code[22] using the ACER module to generate continuous energy cross sections for the MCNP code. New MCNP calculations are performed for the D(d,n) interaction for the zero-degree angle using the adjusted cross sections.

Figs. III.39- III.41 compare the spectrum obtained from Monte Carlo calculation with the adjusted cross sections to those obtained from experiment and Monte Carlo calculation with ENDF/B-VI cross sections for peak regions. Note that all the results correspond to the D(d,n) source with zero-degree angle at different projectile energies of 3 MeV, 5 MeV and 7 MeV.

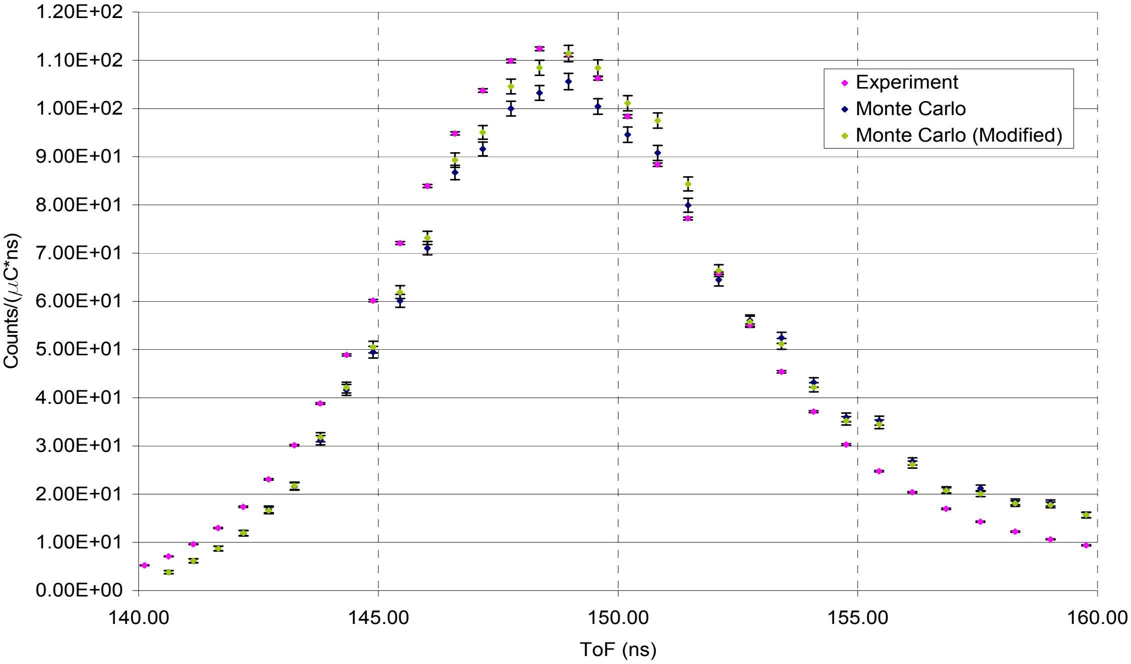

Figure III.39 Comparison of modified 3 MeV D(d,n) Monte Carlo calculations and experimental data for 0 degree angle. (Peak Region)

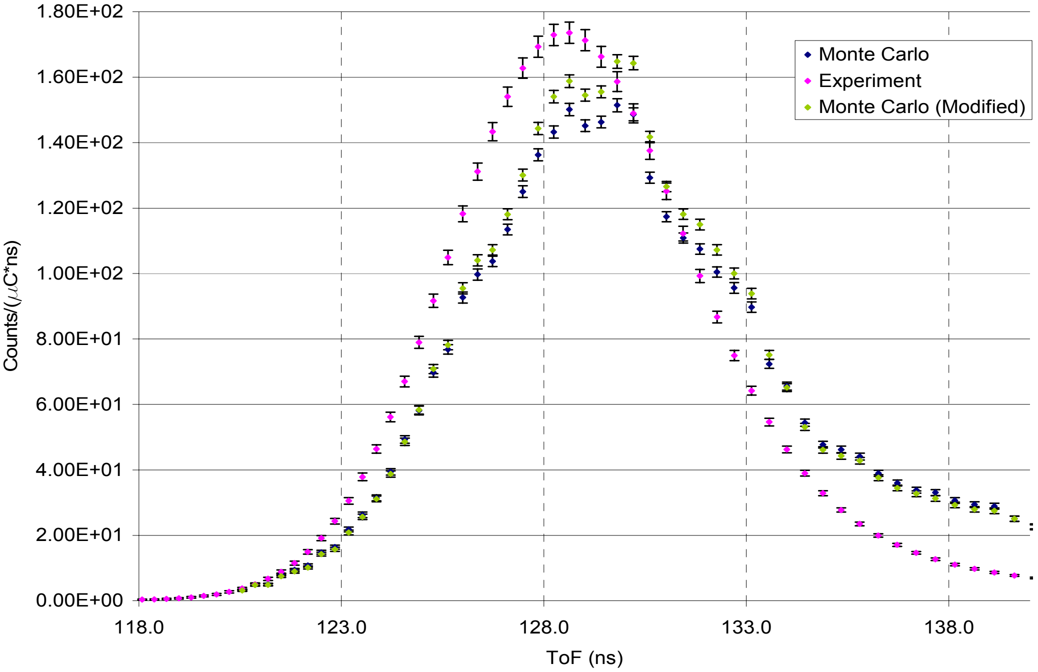

Figure III.40 Comparison of modified 5 MeV D(d,n) Monte Carlo calculations and experimental data for the 0 Degree angle. (Peak Region)

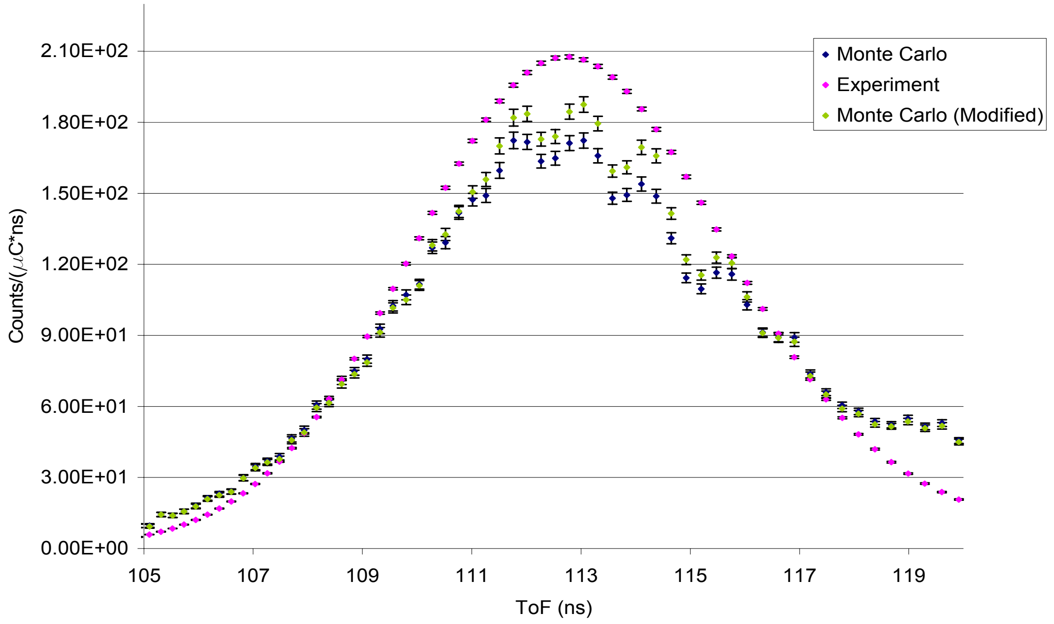

Figure III.41 Comparison of Modified 7 MeV D(d,n) Monte Carlo calculations and experimental data for the 0 degree angle. (Peak Region**)**

It is apparent that at the peak region, the calculated spectra based on the adjusted cross sections are closer to the experimental predictions. The relative differences between the experimental and new calculation data are ~3.5%, ~8% and ~11%, for 3MeV, 5MeV and 7MeV respectively, while the differences for the ENDF/B-VI based calculations results are ~8%, ~13%, ~18% for projectile energies of 3 MeV, 5 MeV, and 7 MeV, respectively. Note that the statistical errors of the new Monte Carlo calculations are similar to the previous ones (see Table III.6).

III.4.5.2 Multigroup Sn deterministic calculation for a PV problem

A multigroup cross-section library was generated based on the adjusted cross sections using the procedure described in Ref. 23. To test the multigroup cross sections, we simulate a 1-D reactor pressure vessel (PV) problem shown in Figure III.42.

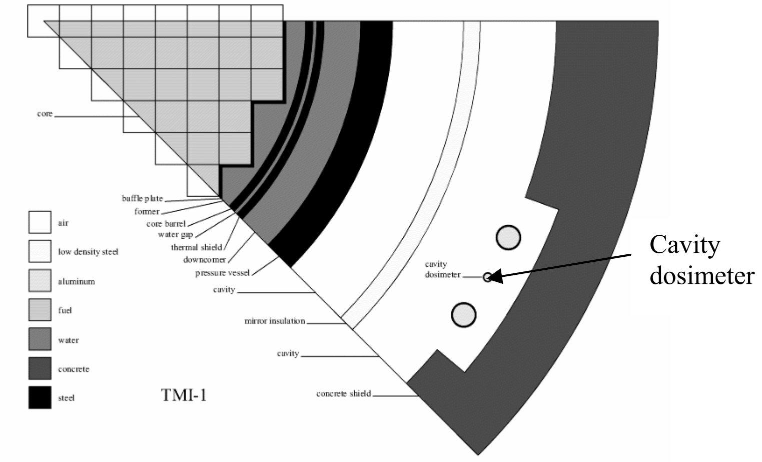

Figure III.42 Reactor pressure vessel model**.**

The reaction rates for ^{63}Cu(n,α), ^{54}Fe(n,p), ^{58}Ni(n,p), ^{46}Ti(n,p), ^{237}Np(n,f), and ^{238}U(n,f) interactions are determined at the cavity dosimeter and compared to the results obtained for a similar library derived from ENDF/B-VI. Table III.9 gives the reaction rate ratios (ENDF/B-VI/adjusted cross-section) for the six interactions.

Table III.9 Reaction Rate Ratios (ENDF/B-VI/adjusted cross-section) at the Cavity Dosimeter

Interaction	Threshold Energy (MeV)	$\frac{ENDF / B-VI}{Adjusted}$
^{63}Cu(n,α)	3.7	.9410
^{54}Fe(n,p)	1.0	.9862
^{58}Ni(n,p)	0.5	.9877
^{46}Ti(n,p)	2.97	.9627
^{237}Np(n,f)	0.1	.9986
^{238}U(n,f)	0.5	.9958

This is an important finding, because it indicates that the PV fluence might have been underestimated based on the currently available libraries. This can be a very important issue for the reactor material integrity and lifetime. Hence, future studies are needed.

IV. Summary, Conclusions, and Future Work

We have carried out a multifaceted research project to improve our knowledge of the iron cross section which should have a significant impact on future nuclear energy programs.

For this project a special Time-of-Flight (ToF) experiment was designed to examine the inelastic scattering cross sections of iron. To optimize the experiment and evaluate the cross sections, we have investigated different computational approaches and developed efficient models and a new tallying option for the MCNP Monte Carlo calculations. The new tallying option provides detailed information on neutrons that have gone through scattering interactions in the iron shell and subsequently arrived at the detector site.

To optimize the experiment, we used the new tallying option to determine the number of neutrons that have gone through inelastic scattering within the iron shell and subsequently were detected. By performing a series of simulations for different combinations of neutron energies and shell thicknesses, we concluded that for the energy range of interest (>1 MeV), a thickness of ~3-10 cm yields the maximum number of detected inelastically scattered neutrons.

Based on the aforementioned studies, we fabricated two iron shells with thicknesses of ~3 cm and 8 cm. To be able to examine the energy range of interest, we considered two source reactions, ^{15}N(p,n) and D(d,n). Further, to obtain detailed source distribution information, angular distribution measurements were made at a number of charged-particle energies.

Using a bi-linear interpolation approach, we developed detailed source distributions using the ‘sphere off’ measurements for the 0, 15, 45, 60, 90, 100, 120 and 135 degree angles for 5.1 MeV protons with the ^{15}N(p,n) reaction, and 3 MeV, 5 MeV and 7 MeV deuterons with the D(d,n) reaction. To examine the validity of these distributions, we performed Monte Carlo calculations, and determined the ToF spectra. Comparisons with the experimental data indicated that our bi-linear approach was effective for the zero angle for the D(d,n) and ^{15}N(p,n) experiments. However, for angles larger than 0 degrees, because of the complex angular behavior of the source, the bi-linear interpolation is not adequate, given the limited number of angles that had been measured in the angular distribution.

Using the inferred spatial and angular dependent source distribution, we performed a series of ‘sphere on’ simulations for the ^{15}N(p,n) reaction using 5.1 MeV protons with small and large spherical shell thicknesses at the 0, 45, and 90 degree angles. Simulations were also done for the large sphere using the D(d,n) reaction for deuteron energies of 3, 5, and 7 MeV, at angles of 0, 45 and 90 degrees. Comparisons of the Monte Carlo predicted ToF spectra with measured data for different source reactions, charged-particle energies, iron shell thicknesses, and beam angles, have demonstrated that the zero degree-angle cases are significantly more accurate than other angles. Further, increasing the energy of the charged-particle resulted in the reduction of the accuracy of the Monte Carlo predictions, because of the increased inaccuracy in the interpolated source distribution. After accounting for the effect of the experimental error and Monte Carlo statistical error, we concluded that there are differences which could be attributed to the inaccuracy of the inelastic cross sections in the ENDF/B-VI library.

To support this hypothesis, and verify the accuracy of our measurements and analytical methodologies, we estimated the total cross section of iron by comparing the ‘sphere on’ and ‘sphere off’ experimental data. Since the total cross section can be easily estimated from the ratio of uncollided to source neutrons, we used the new tallying option to estimate the fraction of uncollided neutrons, and corrected the measured neutron count that included both uncollided and scattered neutrons. To be able to estimate the cross section accurately, we considered only the peak energy bin at which both experimental and calculation predictions have the lowest errors. The estimated total iron cross sections at the peak energy bins were in excellent agreement (within 1%) with the available data in the ENDF/B-VI library. This result provided further confidence in our experimental and analytical methodologies.

In order to examine the impact of inelastic scattering on the differences observed between the Monte Carlo and experimental results, we considered changing the inelastic and elastic cross sections while keeping the total cross section constant. Considering only the peak energy bins for the D(d,n) reaction at the zero-degree-angle for different projectile energies of 3, 5, and 7 MeV, we decreased the inelastic cross sections in energy ranges of 6.1534 MeV to 6.2035 MeV, 8.1550 MeV to 8.2050 MeV and 10.7561MeV to 10.8061 MeV by -21%, -29%, and -35%, respectively. For this purpose, we developed a menu driven algorithm which easily modifies any cross section type in the ENDF/B-VI library. Using the modified point-wise cross sections in NJOY, we prepared a new continuous (point-wise) energy cross section file, and performed Monte Carlo calculations to determine the ToF spectra. Comparison of the new Monte Carlo spectra with the experimental data demonstrated that the modified cross sections have reduced the differences by ~40% in the peak regions where the changes were made. Further, in order to examine the effect of the new cross sections on pressure vessel cavity dosimetry, we prepared a 47-group multigroup cross section library, and performed a 1-D discrete ordinates calculation to estimate the reaction rate for six standard dosimeters, and observed that the modified cross sections resulted in higher reaction rates at the cavity dosimeter. This is an important finding, because it demonstrates that the currently available cross section libraries may lead to underestimation of the neutron fluence, and therefore the material damage.

We believe that this project has resulted in the development of experimental techniques and computational methodologies for optimization and analysis of the ToF experiments. Our studies have demonstrated that future studies should consider more detailed measurements for development of source distributions for the Monte Carlo modeling. Also, it is highly beneficial and important to develop numerical methodologies for charged-particle and neutron transport, which consequently results in detailed source distributions. Determining accurate source distributions will allow improved reliability of experiments at angles other than zero degrees, and therefore the possibility of performing more detailed analyses. These analyses are essential for improving our confidence in the adjusted cross sections and for expanding the adjustment to the whole cross section. Finally, to be able to estimate the amount of adjustment throughout the whole spectrum, it is necessary to develop new methodologies based on Monte Carlo and deterministic transport approaches.

References

1)U.S. Nuclear Regulatory Commission Regulatory Guide 1.190, "Calculational and dosimetry methods for determining pressure vessel neutron fluence," U.S. Nuclear Regulatory Commission (2001).

2)C.Y. Fu in "ENDF-201, ENDF/B Summary Documentation," ed. P.F. Rose, Brookhaven National Laboratory Report BNL-NCS-17541 (1991).

3)M. Holman and A. Konecná, "Neutron transmission through iron (sic) sphere, comparison of measured and calculated leakage spectra," ŠKODA Nuclear Machinery Company, Plzen, Czech Republic (1995).

4)E. Sajo, M.L. Williams, and M. Asgari, "Comparison of measured and calculated neutron transmission through steel for a ^{252}Cf source," *Ann. Nucl. Energy*, 20(9) 585 (1993).

5)M.B. Stanka, J.M. Adams, C.M. Eisenhauer, "Proton recoil measurements of the ^{252}Cf fission neutron leakage spectrum from an iron sphere," *Nucl. Sci. & Eng*., 143, 68 (2000).

6)R.W. Finlay, C.E. Brient, D.E. Carter, et al., "The Ohio University beam swinger facility," *Nucl. Inst & Meth*., 198, 197 (1982).

7)T. N. Massey, et al., "A measurement of the ^{27}Al(d,n) spectrum for use in neutron detector calibration". *Nucl. Sci. and Eng.*, 129, 175 (1998).

8)W. B. Howard, S.M. Grimes, T.N. Massey, S.I. Al-Quraishi, D.K. Jacobs, and C.E. Brient and J.C. Yanch, *"*Measurement of the Thick Target ^{9}Be(p,n) Neutron Energy Spectrum*", Nucl. Sci. and Eng.*, 138, 145 (2001).

9) S. Gardner, A. Haghighat and A. Patchimpattapong, “Monte Carlo Analysis of Spherical Shell Transmission Experiment with New Tallying Methodology, presented at M&C 2001 – ANS Topical Meeting, Salt Lake City, Utah (2001).

10)J. F. Briesmeister, “MCNP- A General Monte Carlo N-Particle Transport Code, Version 4C”, LA 13709-M, Los Alamos National Laboratory, (2000).

11)M. Drosg, DROSG-2000, PC database for 56 neutron source reactions, documented in the IAEA report IAEA-NDS-87 Rev. 5 (January 2000). PC diskettes received /downloaded from the IAEA Nuclear Data Section.

12)J. C. Wagner and A. Haghighat, “A^{3}MCNP: Automatic Adjoint Accelerated MCNP User’s Manual,” Users Manual, The University of Florida Transport Theory Group, May (2000).

13)DOORS3.2, "RSICC Computer Code Collection, DOORS3.2, One, Two- and Three Dimension Discrete Ordinates Neutron/Photon Transport Code System," Oak Ridge National Laboratory, Oak Ridge Tennessee, July (1998).

14)G. Sjoden, "PENTRAN: A Parallel 3D S_N Transport Code with Complete Phase Space Decomposition, Adaptive Differencing, and Iterative Solution Methods," Ph.D. Thesis in Nuclear Engineering, The Pennsylvania State University, May (1997).

15)A. Geist, A. Beguelin, J. Dongarra, W. Jiang, R. Manchek, and V. Sunderam, *PVM: Parallel Virtual Machine. A User's Guide and Tutorial for Networked Parallel Computing*. The MIT Press, Cambridge, Massachusetts and London, England, (1994).

16)B. Carlson, "Solution of the Transport Equation by S_N Method" *LA-1891* Los Alamos Scientific Laboratory, (1955).

17)V. Kucukboyaci and A. Haghighat, "Analysis of PENTRAN Features/ Formulation for BWR Core Shroud Problem," Proceedings of 1998 Radiation Protection and Shielding Conference, Nashville, TN (1998).

18)K. D. Lathrop, and B. G. Carlson, "Discrete Ordinates Angular Quadrature of the Neutron Transport Equation," LA-3186, Los Alamos Scientific Laboratory (1965).

19)G. Longoni, and A. Haghighat, "Development of New Quadrature Sets With the 'Ordinate Splitting Technique'," presented at M&C 2001 – ANS Topical Meeting, Salt Lake City, Utah (2001).

20)G. Longoni, and A. Haghighat, "Development of the Regional Angular Refinement and its Application to the CT-Scan Device," ANS Topical Meeting, Hollywood, Florida (2002)

21)ENDF "Evaluated Nuclear Data Files," T-2 Nuclear Information Service, Los Alamos Scientific Laboratory, Brookhaven National Nuclear Data Center, Upton, NY, (2002).

22)R. E. MacFarlane and R. M. Boicourt, "NJOY: A Neutron and Photon Processing System," *Trans. Am. Nucl. Soc.* 22, 720 (1975).

23)A. F. Alpan, "Advanced Methodology For Generating Multigroup Cross Sections For Shielding Calculations, "Ph.D. Thesis, Nuclear Engineering, The Pennsylvania State University, (2003).